Shining a Light into the Dark: Cosmic Voids as Cosmological Probes of Evolving and Interacting Dark Sector Physics

Eromanga Adermann

A thesis submitted in fulfilment of the requirements
for the degree of Doctor of Philosophy

School of Physics, Science Faculty
The University of Sydney

February 2019

Abstract

The dark sector of the Universe presents one of the greatest unanswered questions in all of physics. Although it has been nearly two decades since the surprising discovery of dark energy, and many decades since the discovery of dark matter, the quest to understand them both have not yet yielded many significant breakthroughs. The problem of understanding the dark sector, which dominates the current mass-energy content of our Universe, is as daunting as ever, and without a solid theoretical framework for it, we are limited in our understanding of the history, evolution and eventual fate of the cosmos.

Our best characterisation of the dark sector can be found within the Standard Model of Cosmology: Λ Cold Dark Matter (ΛCDM). Within the model, dark matter is non-relativistic, non-baryonic, and does not interact via the electromagnetic force. Dark energy is mathematically described by a positive cosmological constant in the field equations of General Relativity, and interpreted as a form of energy that produces a negative pressure on the fabric of the cosmos, driving it to accelerate in its expansion. The success of the ΛCDM model in predicting various features observed in the large-scale structure has led to its establishment as the Standard Model of Cosmology. However, despite its success, ΛCDM still provides a somewhat simple characterisation of the dark sector, which reflects our lack of insight into its nature. It may be a successful model, but it is by no means a complete one.

In this thesis, I aim to address this theoretical problem by finding the unique signatures of two non-standard, alternative cosmological models, in order to provide a means of observationally probing the dark sector and distinguishing between the different models of dark energy.

The alternative models of interest in this work are an uncoupled quintessence model (ϕCDM) and a coupled dark energy model (CDE). Both these models characterise dark energy as a dynamic, evolving scalar field, ϕ, rather than as a cosmological constant. The CDE model additionally allows interaction between the scalar field and the dark matter field, resulting in the decay of the scalar field into dark matter. These extensions to the dark sector alter the expansion history as well as the matter power spectra of the universe, and thus they might be expected to also affect observable properties of the cosmic web. Indeed, previous studies have demonstrated that the cosmic web is not just influenced by gravitational interactions, but also by the properties of the dark sector in these models (for

example, Carlesi et al., 2014a,b; Elahi et al., 2015).

In this work, I focus on identifying the signatures of the scalar field and dark sector coupling in the properties and evolution of cosmic voids within the large-scale structure. Specifically, I compare the voids within the uncoupled quintessence and coupled dark energy model to those within a ΛCDM universe. To do this, I use N-body adiabatic hydrodynamical simulations to model the large-scale structure of universes governed by each of the three cosmologies, and I develop a density-based void-finding method to identify the voids within these simulations. I then investigate the population size, volume, ellipticity, prolateness and average density of voids that form in the dark matter distribution of each of the three models in the redshift range $z = 12-0$, and compare them to determine how the underlying cosmology influences void evolution and to identify unique signatures for use as observational probes of cosmology.

Across this redshift range, I find that the volumes and shapes (defined by ellipticity and prolateness) mostly do not vary across cosmology to a statistically significant extent, suggesting that both these characteristics of voids are largely insensitive to the differences between a scalar field and a cosmological constant, and dark sector interactions. However, I find that the average densities of voids are systematically lower in the alternative models than in the standard model, indicating that the scalar field causes voids to form with less material within them than in the standard model. I propose that the effect of the scalar field manifests itself in the form of an enhanced void evacuation rate, which also produces greater void merger rates. I also find that the uncoupled quintessence model produces emptier voids than the coupled model, demonstrating that the coupling between dark matter and dark energy tends to reduce the emptying effect of the scalar field, likely due to the altered effective gravitational force acting on dark matter particles that arises directly from coupling. These results reveal that void densities are highly sensitive to the presence of a scalar field and to some extent dark sector coupling, and consequently could form the basis of observational probes of cosmology in the Universe.

Ultimately, I demonstrate the promising potential of void densities as a powerful probe of dark sector physics in our Universe, particularly of the scalar field. Thus, I conclude by proposing a number of methods to observationally tease out the signature, so that in the near future we may successfully utilise it to determine the nature of dark energy.

Acknowledgements

The completion of my PhD thesis marks the end my eight and a half years at university! And what an extraordinary journey it has been! There have been many various challenges along the way, both technical and emotional, but there have also been an incredible amount of wonderful, inspiring and satisfying moments too. I have learned and developed so much, and feel extremely happy that my efforts have culminated in something tangible. I may now call myself 'Doctor', and reasonably request that others do so too. More importantly, I have succeeded in achieving the goal I set for myself at the beginning of my PhD: to add something significant to humanity's body of knowledge.

As with many significant achievements, the hard work was not completed by just one person. I am extremely grateful to the following people for their guidance and support during my studies.

First, I would like to express my immense gratitude to my supervisor and mentor, Dr. Pascal Elahi, who from the very start has been there to solve all the technical (and sometimes emotional) problems that my work presented. Thank you Pascal for answering my very many questions, debugging my code, discussing ideas, editing my papers and thesis, and helping me become an independent researcher. The time and energy you invested in developing my skills and knowledge have not been wasted.

Second, I am especially grateful to my supervisor Prof. Geraint Lewis, for agreeing to take me on as a PhD student at short notice and being willing to accommodate my desire to study dark energy. Thank you Geraint for continuing to accommodate my interests throughout the course of my PhD, and for giving me the freedom to explore other areas unrelated to my project, while also keeping me on track to complete my degree. Without your input, I might still be conducting research and trying to add more to my thesis.

I have been very fortunate to be looked after by numerous academics besides my supervisors during my studies. In particular, I am extremely appreciative of the mentoring and counselling that Prof. Anne Green, my former Honours supervisor, has provided me. Thank you Anne for your sound, practical advice, which has always set me on the right path, your understanding and empathy, which have helped me overcome various hurdles, and your belief in me, which has helped me find confidence in myself and inspired me to

reach for the stars. I must also thank A/Prof. Tara Murphy, my former supervisor during my days in the Talented Student Program, for providing me with advice and guidance during my PhD whenever I asked for it, and for believing in me when I had little belief in myself, thus providing the motivation for me to follow my dreams and study physics at the highest level possible.

I have also been lucky to be surrounded by great scientists at SIfA who have inspired new ideas and helped me gain greater insight into my work. In particular, I am grateful to Dr. Krzysztof Bolejko for our very informative discussions about the observational use of voids.

It might have been possible for me to complete my PhD without any friends, but I sure am thankful I didn't have to! I have really enjoyed and appreciated the camaraderie shared by myself and my fellow PhD students, both past and present. Thank you to my office mates, colleagues and friends, in particular Marcin Glowacki, Chris Herron, Nik Iwanus, Asger Gronnow, Nuwanthika Fernando and Becky Brown, for brightening my days with your friendship and company, during the good and the bad times, and for all the assistance with various technical problems that you have provided me these past few years. I am very grateful for the support, laughter and close relationships we have shared. I extend my gratitude to my close friends outside of SIfA: Jarrah Sastrawan, Claudia Yan, Pauline Wong and Jack Freestone, whose friendship and support have made the journey much more pleasant for me, and who provided me with refreshing breaks from working on code or writing a paper, whether it be in the form of a catch-up over lunch or snorkelling in the Great Barrier Reef. I would also like to acknowledge my dear friend Diego Funai, whose friendship and support I will always be grateful for. I wish I could have celebrated this achievement with you.

Finally and most importantly, I offer my deepest and most heartfelt thanks to my parents, May and Rudiger, and my brothers, Falko and Felix, for providing me with all the love, care and encouragement I needed to be where I am now, and for always believing in me no matter what. I would not be completing my PhD were it not for you. I hope you know how much you have done for me, and how much it means to me.

“It is far better to grasp the Universe as it really is than to persist in delusion, however satisfying and reassuring.” - *Carl Sagan*

Declaration

I, Eromanga Adermann, hereby declare that all work presented in this thesis is based on research conducted by me, other than that declared below, during my PhD candidature at The University of Sydney, from March 2014 to August 2018. This work has not been presented for a degree at this or any other university, and is, to the best of my knowledge, original except where duly acknowledged in the text.

Chapters 4 and 5 are reproduced from papers published in refereed journals in collaboration with other authors. These papers were fully written by myself, apart from the exceptions noted below, and I was primarily responsible for the work presented.

Significant contributions made by other people are as follows:

- The simulations used in Chapter 4 and Chapter 5 were produced by Dr. Pascal Elahi and Prof. Chris Power.
- The fitting code I wrote to find the best fit parameters for the volume and density distributions was based on code originally written by Dr. Joseph Callingham.
- Section 4.3 was primarily written by Dr. Pascal Elahi and edited by me.
- The text in this thesis was edited and checked by Dr. Pascal Elahi and Prof. Geraint Lewis.

Eromanga Adermann
1st February 2019

Publications

The following chapters have been reproduced from papers that have been published in refereed journals:

- Chapter 4: **Eromanga Adermann**, Pascal J. Elahi, Geraint F. Lewis, Chris Power "Cosmic Voids in Evolving Dark Sector Cosmologies: the Low Redshift Universe" *Monthly Notices of the Royal Astronomical Society*, 2017, 468, 3381–3394.
- Chapter 5: **Eromanga Adermann**, Pascal J. Elahi, Geraint F. Lewis, Chris Power "Cosmic Voids in Evolving Dark Sector Cosmologies: the High Redshift Universe" *Monthly Notices of the Royal Astronomical Society*, 2018, 479, 4861–4877.

Contents

List of Figures

List of Tables

CHAPTER 1

Introduction: Understanding the Large-Scale Universe

1.1 Cosmology

Cosmology is the study of the origin, nature, evolution and fate of the Universe we live in. It is as old as humanity itself, emerging when primitive societies attempted to explain the world around them. The advent of scientific cosmology can be traced back to the early Greeks, who were the first to construct a cosmological model to explain and predict the motions of the heavenly bodies without relying on myth. As technology advanced and new ideas emerged, the early cosmological model underwent various revolutionary changes, finally arriving at a heliocentric model of the Solar System featuring elliptical orbits that could be explained by Newtonian mechanics, existing within a sea of stars.

A second set of revolutions to our understanding of the Universe occurred in the 20^{th} century, driven by the advent of new ideas of gravity and advancements in telescope technology once again. The discovery that the cosmos contains many more galaxies than our own, many of which are moving away from us, led to the conclusion that the Universe began its life in an initial burst and had been expanding ever since. The observation of the microwave afterglow from the initial burst confirmed that the cosmos had indeed begun its life in a 'Big Bang', and was not eternal and unchanging. Finally, the discoveries of dark matter, and the acceleration of the expansion of the Universe, mere decades ago have revealed just how much of the cosmos we are yet to elucidate.

Today, cosmology focuses on the large-scale properties of the Universe as a whole, including its dynamics and evolution, in order to answer the big questions about how and why the cosmos is the way it is, and to determine how these properties are influenced by the fundamental physics of the Universe. Modern cosmology progresses in much the same way as it did thousands of years ago; through the combination of new ideas and models and advancements in observational technology. It integrates both the theoretical and observational aspects of astronomy and particle physics to understand the nature and

evolution of the Universe. Observational astronomy and experimental particle physics provide us with insight into what the Universe is, while the mathematical frameworks of theoretical cosmology provide us with the how and why.

Cosmology has so far revealed that the Universe is spatially flat, isotropic and homogeneous on large scales. It began its life as a very hot and dense place, evolving into its present state through a long process of expansion (including a period of very rapid expansion) and cooling, and is currently expanding at an ever-increasing rate. There is strong evidence for an invisible dark sector dominating its total mass-energy content, but little is understood about its nature. As such, one of the primary goals of cosmology today is to unravel the mystery surrounding the dark sector, and to determine how and whether it fits into the current standard parameterisation of the Big Bang model: **The Standard Model of Cosmology**.

1.2 The Standard Model of Cosmology

One of the greatest achievements of modern cosmology is the establishment of the Standard Model of Cosmology: Λ Cold Dark Matter (ΛCDM). The model offers a simple and very successful explanation for the evolution of the Universe and its large-scale characteristics. Within the model, universal expansion and large-scale gravitational interactions are fully governed by Einstein's field equations. The Universe is also spatially flat (it has no spatial curvature on very large scales, so that Euclidean geometry applies on these scales), and dominated by an invisible dark sector comprised of dark matter and dark energy, which together make up approximately 95% of its current mass-energy content. In this section, we will explain the foundations and key components of the standard model, and outline its development.

1.2.1 The Cosmological Model

The establishment of ΛCDM began with the **the cosmological model**, which offers a more general mathematical description of the Universe. It rests on two fundamental assumptions: the cosmological principle and the universality of the laws of physics. The cosmological principle states that our place in the Universe is no more or less special than any other place in the Universe (Milne, 1933). This implies that the Universe on a large enough scale is both homogeneous and isotropic – it looks the same from every location (homogeneity) and in all directions (isotropy). The principle derives from the Copernican Principle – we are not privileged observers – and has been verified by large galaxy redshift surveys (for example Ntelis et al., 2017), with homogeneity occurring on scales of greater than 300 Megaparsecs (Mpc; 1 Mpc is equivalent to 3.086×10^{22} m). This homogeneity and isotropy of the luminous matter distribution in the Universe is visible in the data from the Third Sloan Digital Sky Survey (SDSS-III; Eisenstein et al., 2011), shown in Figure 1.1.

The cosmological model assumes that gravity obeys the theory of General Relativity (GR; Einstein, 1916a), which more accurately predicts the perihelion precession of various

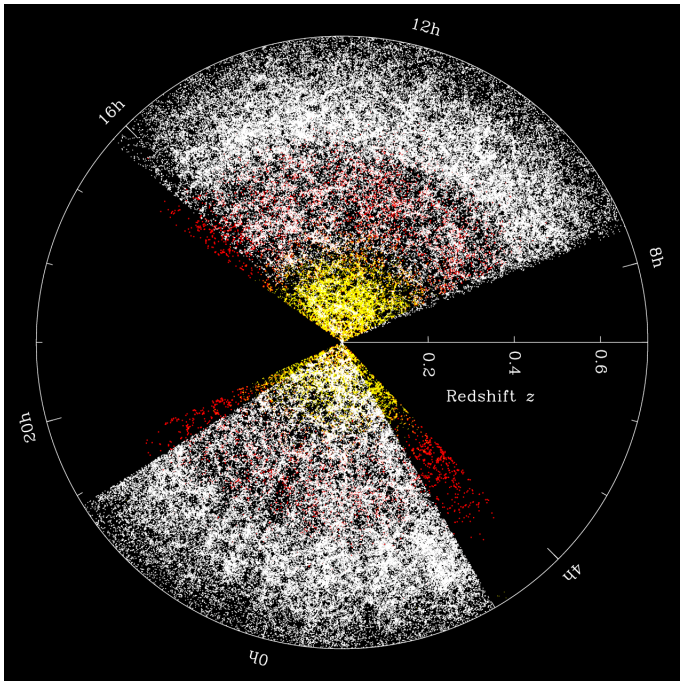

Figure 1.1: A projected slice of the galaxies detected by the Third Sloan Digital Sky Survey (SDSS-III), illustrating the large-scale homogeneity and isotropy in the statistical distribution of galaxies. The white points are galaxies from the BOSS CMASS sample (Baryon Oscillation Spectroscopic Survey 'Constant Mass' sample; Dawson et al., 2013), the red points are the red luminous galaxies, and the yellow points are from the main galaxy sample. Credit: Michael Blanton and the SDSS collaboration.

Solar System planets (Le Verrier, 1859; Biswas & Mani, 2008), the bending of light around the Sun (Dyson, Eddington & Davidson, 1920), gravitational redshift (Greenstein, Oke & Shipman, 1971) and gravitational waves (Einstein, 1916b, 1918; Abbott et al., 2016, 2017b), than other models of gravity, including Newtonian gravity. In GR, the gravitational field is the result of curvature in four dimensional spacetime, induced by the presence of energy and mass. This is fully described by Einstein's field equations:

$$R_{\mu\nu} - (\frac{1}{2}R - \Lambda)g_{\mu\nu} = \frac{8\pi G}{c^4}T_{\mu\nu}, \tag{1.1}$$

where $R_{\mu\nu}$ is the Ricci curvature tensor, R is the Ricci scalar, $g_{\mu\nu}$ is the metric tensor, G is the gravitational constant and c is the speed of light in a vacuum. The Ricci scalar/tensor and the metric tensor describe the curvature of spacetime in response to energy sources. The stress-energy tensor, $T_{\mu\nu}$, encapsulates the density of energy and momentum flux that give rise to spacetime curvature, or equivalently, the gravitational field. The diagonal components of the stress-energy tensor represent the energy density (in the 00-component) and the normal stress (called pressure when isotropic) exerted by sources in three orthogonal directions (11-, 22- and 33-components). The off-diagonal elements of the stress-energy

tensor represent shear stress (the component of stress that is parallel to a surface), while the 0^{th} components of the off-diagonal elements can also be interpreted as the components of the linear momentum density crossing a surface. Radiation produces anisotropic stress, and hence it will result in non-zero shear stress, while collisionless dust (which can be used to model dark matter) will produce only isotropic stresses, and contribute only to the diagonal elements. Λ is the cosmological constant, a geometric quantity which naturally arises out of the action that produces the above equation. It was part of the original equations written down by Einstein (Einstein, 1917), and was required to ensure a static universe. It was then subsequently removed to allow for an expanding universe, and was only recently re-added as a constant of positive value to account for the acceleration in the expansion of the Universe. Although Λ is usually written on the left-hand side of Equation 1.1, where it may be interpreted as a description for the behaviour of space-time to accelerate in its expansion even in the absence of the usual sources of energy (namely, matter and radiation), it can also be written on the right-hand side so that it is incorporated as part of the sources in the stress-energy tensor. It would then represent a fluid with constant energy density and constant, isotropic negative pressure, altering the diagonal elements of the tensor.

One exact solution of Einstein's field questions that describes a homogeneous, isotropic spacetime geometry is the Friedmann-Lemaître-Robertson-Walker (FLRW) metric:

$$ds^2 = -c^2dt^2 + a^2(t)\left[\frac{dr^2}{1-kr^2} + r^2(d\theta^2 + \sin^2\theta d\phi^2)\right], \tag{1.2}$$

where ds is the fundamental line element, $a(t)$ is the scale factor at time t after the birth of the Universe (defined so that its value today is equal to 1), θ and ϕ are the comoving polar and azimuthal coordinates, respectively, and r is a geometry-dependent function of the comoving radial coordinate, χ. The FLRW metric describes three possible homogeneous and isotropic geometries – closed (positive curvature), flat (no curvature) and open (negative curvature) – encoded in the value of k:

$$k = \begin{cases} 1, & \text{if closed} \\ 0, & \text{if flat} \\ -1, & \text{if open.} \end{cases} \tag{1.3}$$

In each of these geometries, r takes on the following expressions:

$$r = \begin{cases} \sin\chi, & \text{if closed} \\ \chi, & \text{if flat} \\ \sinh\chi, & \text{if open.} \end{cases} \tag{1.4}$$

Observations favour a flat universe (de Bernardis et al., 2000; Bennett et al., 2013).

The scale factor $a(t)$ in the FLRW metric is a dimensionless quantity that relates the proper distance between two observers at a given time to their comoving distance, thus parameterising the expansion or contraction of spacetime. As such, it quantifies the

expansion of the Universe. Its evolution is dependent on the matter density, radiation density and dark energy density.

The time evolution of $a(t)$ can be found by solving the Friedmann equations, which are derived from the Einstein field equations for the FLRW metric:

$$\left(\frac{\dot{a}}{a}\right)^2 = \frac{8\pi G\rho}{3} - \frac{kc^2}{a^2} + \frac{\Lambda c^2}{3}; \tag{1.5}$$

$$\frac{\ddot{a}}{a} = \frac{4\pi G}{3}\left(\rho + \frac{3p}{c^2}\right) + \frac{\Lambda c^2}{3}; \tag{1.6}$$

$$\dot{\rho} = -\frac{3\dot{a}}{a}\left(\rho + \frac{p}{c^2}\right). \tag{1.7}$$

The quantities ρ and p respectively denote the density of and pressure exerted by cosmological fluids (e.g. matter, radiation or dark energy) on spacetime, while $\dot{a}$ and $\dot{\rho}$ represent the first derivative of the scale factor and density with respect to time, and $\ddot{a}$ represents the second derivative of the scale factor with respect to time. The above equations can be solved exactly by assuming that the cosmological fluids in question are perfect fluids (i.e. they can be completely characterised by the mass density in their rest frame and their isotropic pressure). However, since the equations contain three unknowns and only two of the equations are independent, we require a third equation to solve them. This is the relation between the density and pressure, known as the equation of state:

$$w = \frac{p}{\rho c^2}, \tag{1.8}$$

where w is a constant. The equation of state governs how the pressure exerted by the fluid changes with energy density. For example, for $w < 0$, an increase in the density of the source fluid results in greater negative pressure exerted by the fluid, expanding or stretching it. The equation of state determines the specific dependence of the cosmological fluid on the scale factor, as well as the time-dependence of the scale factor. For example, for a flat and matter-dominated universe (where $w \approx 0$), the Friedmann equations dictate that $\rho \propto a^3$ and $a \propto t^{2/3}$.

For a given expansion rate, there exists a critical density, ρ_c, that will asymptotically slow the expansion to a halt:

$$\rho_c(t) = \frac{3H^2(t)}{8\pi G}, \tag{1.9}$$

where $H(t) \equiv \dot{a}(t)/a(t)$ is the Hubble constant at time t. If we rewrite Equation 1.5 in terms of $H(t)$, then it is clear that when the total density in the Universe exceeds the critical density, then $k > 0$, and the Universe will eventually stop expanding and collapse. Conversely, if the total density is smaller than the critical density, then $k < 0$, and the Universe will expand forever. Finally, if the total density is equal to the critical density, then $k = 0$, and expansion will continue indefinitely but at an ever decreasing rate. In this way, the Friedmann equations show that the total density of all energy sources in the Universe affects the curvature of space and its expansion trajectory.

1.2.2 The ΛCDM Model

From theoretical considerations, we arrived at a general cosmological model for our homogeneous and isotropic Universe, consisting of equations governing its evolution. However, to fully describe our Universe, we require values for Λ, ρ, p, w, k and H_0 (the Hubble constant today). These values were provided by observations made throughout the 20^{th} century, allowing cosmologists to refine the general cosmological model into a specific model, ΛCDM, now established as the Standard Model of Cosmology.

The first cosmological model in modern times was courtesy of Einstein, who was the first to introduce the cosmological constant into his field equations (Einstein, 1917), with the purpose of producing a static universe. The cosmological constant would provide the repulsive force to counteract the attractive gravitational force in a matter-dominated universe. However, when Hubble discovered that the Universe was expanding (Hubble, 1929), Einstein and de Sitter put forth a model where both the spatial curvature and the cosmological constant were zero (Einstein & de Sitter, 1932). An important feature of this model is that the matter density was equal to the critical density of the universe, meaning that there would neither be ever-increasing expansion nor contraction. The Einstein-de Sitter model became the standard model for the Universe initially, especially in light of the development of cosmic inflation (see Guth, 1981; Linde, 1984; Steinhardt & Turner, 1984), which predicted a very low spatial curvature, and the lack of evidence for a cosmological constant.

As it was the only known form of matter in the Universe, the cosmological model initially only included ordinary baryonic matter. However, we now understand that the Universe also contains a large amount of invisible, non-baryonic matter, referred to as dark matter. This understanding came after multiple measurements of galaxy and cluster motions and measurements of the cosmic microwave background radiation (CMB), which suggest that dark matter occurs everywhere in the Universe, in approximately five times the amount of baryonic matter (Fabian et al., 1986; Fabbiano, 1993; Hinshaw et al., 2009; Bennett et al., 2013; Planck Collaboration et al., 2014a). Furthermore, the cosmic baryon to photon ratio as measured from primordial elemental abundances (Dar, 1995), and measurements of the amount of baryons in various locations including stars, galaxies, galaxy clusters, galaxy groups, and the interstellar, intergalactic and intracluster medium (Fukugita, Hogan & Peebles, 1998), provide convincing evidence that most of the matter density in the Universe is not baryonic. Dark matter is now characterised by ΛCDM as an invisible, non-relativistic (cold), and non-baryonic form of matter that comprises 27% of the total present-day mass-energy content, and understood to be a key driver of structure formation.

The addition of dark matter to the cosmological model was a significant alteration, but it was by no means the last. By the mid-1990s, there were hints for a non-zero Λ again, in the discrepancies between the ages of globular clusters and the Universe (e.g. Bolte & Hogan, 1995; Chaboyer et al., 1996), and in the large-scale galaxy clustering (Efstathiou, Sutherland & Maddox, 1990). Then in the late 1990s, two independent supernova surveys provided evidence for an accelerating universal expansion (Riess et al., 1998; Perlmutter et al., 1999). The simplest explanation for these results was a non-zero cosmological

constant, with the total matter density, $\Omega_{\rm m}$, being approximately equal to 0.3, and the cosmological constant (dark energy) density, Ω_Λ, being approximately equal to 0.7. This was the first significant evidence in favour of a ΛCDM Universe. CMB measurements shortly afterwards indicated that the Universe was indeed spatially flat (de Bernardis et al., 2000; Hanany et al., 2000), requiring that the total mass-energy density be equal to one, and providing yet another line of evidence for a non-zero Λ. Although the nature of Λ is not understood, within ΛCDM it represents and characterises dark energy, a repulsive form of vacuum energy that drives accelerated expansion, and which also comprises 69% of the current mass-energy content.

Since the establishment of the dark sector within the ΛCDM model, there has been a great effort to refine it further by measuring the parameters of the standard model with increasing precision. There are six free parameters that define the standard model, and constraining their values requires a combination of different and complementary observations to provide consistency checks, remove parameter degeneracies and improve precision. For example, constraining w, $\Omega_{\rm m}$ and Ω_Λ requires not just the CMB matter power spectrum (which offers the most powerful set of constraints), but also other data sets such as baryonic acoustic oscillations (BAO) and supernovae luminosity-distance measurements. The joint constraints for these parameters are presented in Figure 1.2. The combined results of elemental abundances and Big Bang Nucleosynthesis predictions, measurements of the CMB matter power spectrum, galaxy cluster measurements, BAO and gravitational lensing have also constrained the baryon fraction, dark matter fraction and dark energy fraction to within 1% uncertainty.

Multiple lines of evidence, which will be outlined in later sections, have since provided further support for the ΛCDM model, firmly establishing it as the Standard Model of Cosmology.

1.3 The Dark Sector

Despite its dominance of the total matter-energy content in our Universe today (contributing approximately 95% to the total), the dark sector remains a poorly-characterised component of the standard model. In this section, we will motivate the establishment of dark matter and dark energy as components of the standard model, and outline the status of recent inquiries into their nature.

1.3.1 Dark Matter

Dark matter was first proposed in 1937 by Fritz Zwicky. He compared the luminous/visible masses (derived from total light output) of Coma cluster galaxies to their virial masses (derived from their velocities through the cluster), and unexpectedly found that their virial masses were much larger than their luminous masses. The result implied a significant amount of non-luminous mass within the cluster (Zwicky, 1937), which Zwicky dubbed ‘dark matter’.

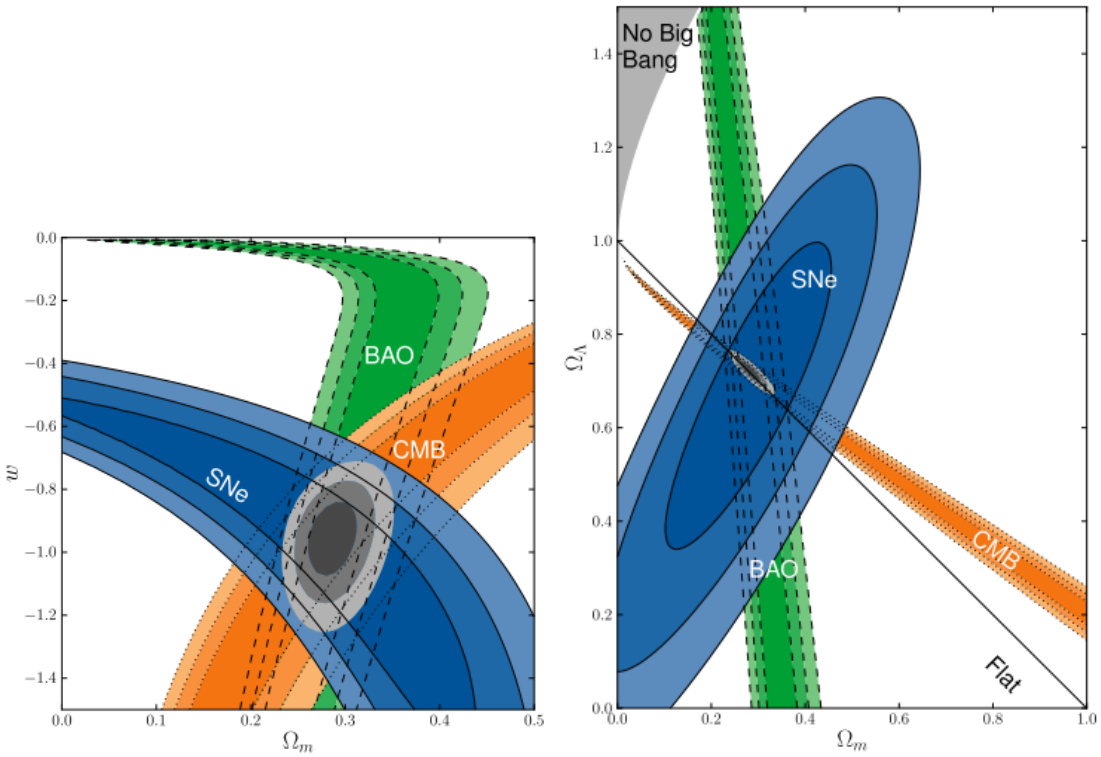

(a) $w - \Omega_m$ (b) $\Omega_\Lambda - \Omega_m$

Figure 1.2: The combined constraints for w, Ω_Λ, and Ω_m, illustrating the use of multiple sets of complementary probes to improve the precision of parameter estimation. These constraints are derived from Union2.1 supernovae Type Ia (SNe Ia) data combined with BAO and CMB data sets and observations. The contours represent the 68.3%, 95.4% and 99.7% confidence regions, which include systematic and statistical uncertainties. Adapted from Suzuki et al. (2012).

However, the notion of dark matter did not take off until the 1970s, when Vera Rubin and Ken Ford published their findings on the rotation curve of the Andromeda galaxy, M31. They found that the rotational velocity did not decrease with radius as expected from Kepler's second law and the amount of visible matter in the galaxy (Rubin & Ford, 1970), which implied the presence of invisible mass in its outskirts. This result was subsequently found in many more spiral galaxies, with the rotation curves remaining flat to large radii even in 21 cm radio observations (Freeman, 1970; Rogstad & Shostak, 1972). The overwhelming conclusion was that spiral galaxies must contain much more mass located in their outer parts than was visible.

Since then, a vast array of observational evidence has appeared, pointing to the presence of copious amounts of invisible mass in the Universe. For example, velocity dispersion estimates for elliptical galaxies differ from the expected values based on the amount of

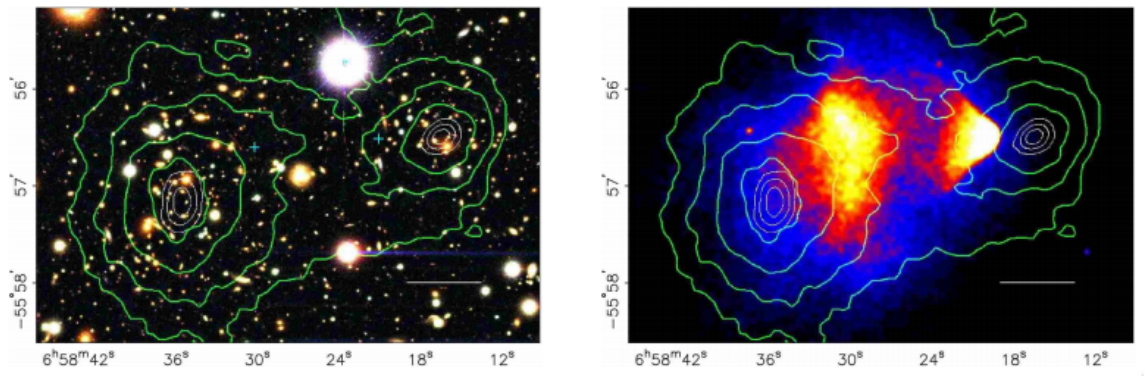

Figure 1.3: Optical and X-ray images of the dynamics of the Bullet Cluster, illustrating the inconsistency between the position of the hot, baryonic gas and the bulk of the matter. Left: Optical image of the Bullet Cluster from the Magellan Telescope, overlayed with a contour plot showing the distribution of mass derived from gravitational lensing measurements. Right: X-ray image from the Chandra X-ray Observatory, overlayed with the same contour plot, showing the spatial distribution of the hot gas during the merger. Credit: Clowe et al. (2006).

visible matter in them (Faber & Jackson, 1976), X-ray studies of hot gas in giant elliptical galaxies show that the amount of matter required to gravitationally bind the hot gas is $5 - 6$ times greater than the visible mass (Fabricant, Lecar & Gorenstein, 1980; Fabricant & Gorenstein, 1983; Fabian et al., 1986; Fabbiano, 1993), and gravitational lensing around clusters reveal masses several times greater than their luminous masses (Limousin et al., 2007; Hoekstra, 2007).

One of the more well-known pieces of evidence for dark matter comes from the study of the Bullet Cluster, which is a system composed of two merging galaxy clusters (Clowe et al., 2006). Most of the luminous matter in this ensemble of galaxies is in the hot X-ray emitting gas. However, by using the cluster as a gravitational lens, Clowe et al. (2006) found that the location of most of the cluster's mass was not within the hot, luminous gas (see Figure 1.3). This result suggests that there are substantial quantities of non-luminous mass within the cluster – in other words, dark matter. The offset between the dark matter distribution and the hot gas also shows that dark matter is not slowed down by ram pressure the way the hot plasma is during the merger, demonstrating its almost collisionless nature, and its lack of coupling to the electromagnetic force.

Dark matter is not completely collisionless, though over large scales and at early times it behaves as a collisionless dust. As such, it may be characterised by its temperature, or equivalently its average velocity and mass, which has significant consequences for structure formation in the Universe. If dark matter travels at relativistic speeds and has a large free-streaming length (so called 'hot' dark matter), then it would dampen the formation of small-scale structures, preventing the bottom-up structure formation favoured by observations (Davis et al., 1985). Furthermore, simulations have revealed that the

large-scale structure in a hot dark matter paradigm is inconsistent with Lyman-α forest observations (White, Frenk & Davis, 1983) and the observed galaxy distribution (Hut & White, 1984). With cosmological data also severely constraining its abundance in the Universe (e.g. Smoot et al., 1992), hot dark matter has been ruled out for the bulk of dark matter in the Universe.

On the other hand, cold dark matter driven structure formation is well-supported by observations (e.g. Ostriker & Peebles, 1973; Ostriker, Peebles & Yahil, 1974; White & Rees, 1978; Davis et al., 1985; White et al., 1987; Coc et al., 2004; Libeskind et al., 2013a). It is slow moving and heavy, with a small free-streaming length, allowing small structures to form and grow into large ones. The CMB temperature map shows that in the very early Universe, both the dark matter and baryonic matter distributions were approximately smooth and homogeneous, each containing only minor density perturbations. The density perturbations within baryonic matter could not grow because of constant interactions with photons. However, the lack of interaction between photons and dark matter allowed the small-scale collapse of density perturbations within dark matter. These small structures eventually grew and merged into ever-larger structures in bottom-up fashion. The gravitational potential of these dark matter overdensities caused the coagulation of baryonic matter, which in turn allowed galaxies, clusters and large-scale structures to form in the Universe.

There exists another type of dark matter with a free-streaming length between that of cold and hot dark matter, known as warm dark matter, which is an alternative to the cold dark matter paradigm. Warm dark matter could alleviate some of the small-scale inconsistencies between cold dark matter predictions and observations (e.g. de Blok, 2010; Lovell et al., 2014). It is unclear how much, if any, of the dark matter bulk consists of warm dark matter. Pinpointing the temperatures and mass of dark matter is still an ongoing task.

The particle identity(-ies) of dark matter remain(s) an area of active research in both cosmology and particle physics. We know that in addition to being either cold or warm, dark matter must also be stable, interact through the gravitational force (i.e. have mass), and must not interact via the electromagnetic force or interact with standard model particles through the strong force. Although standard model neutrinos meet these criteria and make up a small portion of dark matter, they qualify as hot dark matter particles due to their small masses and large free-streaming lengths, and thus cannot make up the bulk of dark matter. Thus, all standard baryonic particles are ruled out as dark matter candidates. Unfortunately for the dark matter search, what lies beyond the standard model of particle physics is largely unchartered and/or unverified territory, although proposals for extensions to the standard model do exist. In fact, many of the proposed candidates for dark matter naturally spring from these models.

One of the earliest candidates considered for dark matter were Massive Compact Halo Objects (MACHOs). These objects consist of completely baryonic massive objects, such as planets, brown dwarfs, neutron stars and black holes, which are too faint to contribute much to the visible mass of galaxies and clusters. MACHOs have been ruled out as dark

matter candidates, due to a lack of detection of microlensing effects they should have on extragalactic sources (Graff & Freese, 1996; Alcock et al., 2000; Tisserand et al., 2007). In addition, independent measurements comparing Big Bang Nucleosynthesis predictions of elemental abundances to measured primordial abundances show that most of the baryons in the Universe are visible and not dark, implying that most of the missing matter cannot be baryonic (Copi, Schramm & Turner, 1995; Dar, 1995). The baryon density derived from these measurements has been further confirmed by CMB measurements (Hinshaw et al., 2013; Planck Collaboration et al., 2014a).

A favourite set of dark matter candidates among theorists are the Weakly Interacting Massive Particles (WIMPs), which arise naturally from supersymmetry, a well-established but unconfirmed extension to the standard model of particle physics which offers a solution to the electroweak hierarchy problem. WIMPs interact with themselves (can self-annihilate) and baryonic matter through the weak force. They are expected to make up about five times more mass than ordinary matter today, which matches up nicely with dark matter density measurements (known as the 'WIMP miracle'). However, despite the excellent motivation for WIMP dark matter and the relic density coincidence, there has not yet been any experimental evidence for either their existence or the validity of supersymmetry. Recent studies into gamma ray emission at the centre of our Galaxy show an excess that could be an indirect signal of certain WIMP candidates, through the particle-antiparticle annihilation of their decay products (see for example, Ackermann et al., 2015; Daylan et al., 2016; Winter et al., 2016), however the gamma ray excess could also be explained by a population of unresolved millisecond pulsars (Lee et al., 2016; Bartels, Krishnamurthy & Weniger, 2016) or by the stellar population in the Galactic bulge and nuclear stellar bulge (Macias et al., 2016).

Another popular candidate is the Lightest Supersymmetric Particle (LSP), the least massive particle in supersymmetry models and also a specific type of WIMP. A highly favoured LSP/WIMP candidate for dark matter is the neutralino, which has not been ruled out by cosmological constraints, as other LSPs have. Other candidates include hidden dark matter, which has no standard model gauge interactions making some forms of it difficult to detect; sterile neutrinos, which are hypothetical and more massive right-handed versions of standard model neutrinos that only interact via the gravitational force with standard model particles, and whose decays ought to produce observable X-rays; and axions, particles which arise from a promising solution to the strong-CP problem of Quantum Chromodynamics (the problem of why Charge + Parity symmetry is not violated in strong interactions; Peccei & Quinn, 1977a,b; Wilczek, 1978; Weinberg, 1978).

Recently, the Strongly Interacting Massive Particles (SIMPs) have emerged as a possible new paradigm for dark matter. SIMPs interact with themselves via the strong force, and with ordinary matter via the weak force. The signatures of these interactions are expected to show up in future collider experiments, electron ionisation signals and gamma ray flux measurements, and may even address other astrophysical problems including the inconsistency between simulated and observed small-scale structure (Hochberg et al., 2014; Tulin & Yu, 2018).

Almost all of these candidates qualify as cold dark matter, with only sterile neutrinos and axions also capable of acting as warm dark matter. Almost all of these candidates are yet to have their existence confirmed, let alone their status as constituents of dark matter. Neutrinos are the only candidate known to exist.

Although not as prominent in the scientific community, there are models that attribute the mass inconsistencies found in galaxy and cluster dynamics to an incomplete understanding of gravity rather than the existence of an invisible form of matter, for example Modified Newtonian Dynamics (MOND; Milgrom, 1983, which is a heavily disfavoured and incomplete model) and Tensor-Vector-Scalar theory (TeVeS; Bekenstein, 2004). The key modification in MOND is in Newton's Second Law, while TeVeS is a relativistic generalisation of MOND. These models and other variations of MOND have not been able to explain key observations such as the Bullet Cluster observations as successfully and simply as ΛCDM, though they have not yet been entirely ruled out as alternatives to the dark matter paradigm.

1.3.2 Dark Energy

Dark energy is a hypothesised form of vacuum energy that permeates through all of spacetime, driving the late-time acceleration of the expansion of the Universe. Under the ΛCDM model, dark energy is characterised by the cosmological constant, Λ, which appears in Einstein's field equations of General Relativity (Equation 1.1). If we assume that Λ is a measure of the intrinsic energy density of the vacuum, then we can write $\Lambda = 8\pi G\rho_{\text{vac}}/c^2$, where ρ_{vac} is the energy density of the vacuum, and move it to the right hand side of Equation 1.1. Thus it can be treated as a source term, representing the mass or energy density of empty space.

The current best estimate for the value of the cosmological constant is $\Lambda = 1.11 \times 10^{-52}$ m^{-2} or 4.33×10^{-66} eV^2 in natural units (derived from Planck Collaboration et al. 2014a parameter values). It has an equation of state given by $w = p/\rho = -1$, meaning that it produces a negative, repulsive pressure on the fabric of spacetime. As Λ is a constant, the dark energy density is uniform across all spacetime and at all times (unlike all other fluids which dilute as the Universe expands), enabling it to dominate the mass-energy content of the Universe at late times despite having a very small mass density. Additionally, this would mean that the dark energy content would continue to increase with time due to the creation of new spacetime, and the Universe will expand in an accelerated manner indefinitely.

Evidence for dark energy was first discovered in the late 1990s by two independent teams of astronomers working on supernova surveys. Specifically, each team was measuring the redshift of supernovae and their apparent magnitudes at further distances than ever before, taking advantage of the discovery that supernovae Type Ia could be used as standardisable candles (Phillips, 1993). Both teams found that the apparent magnitudes of the distant supernovae were approximately 0.25 magnitudes dimmer than expected in a Universe undergoing decelerating expansion (i.e. the Einstein-de Sitter model), which

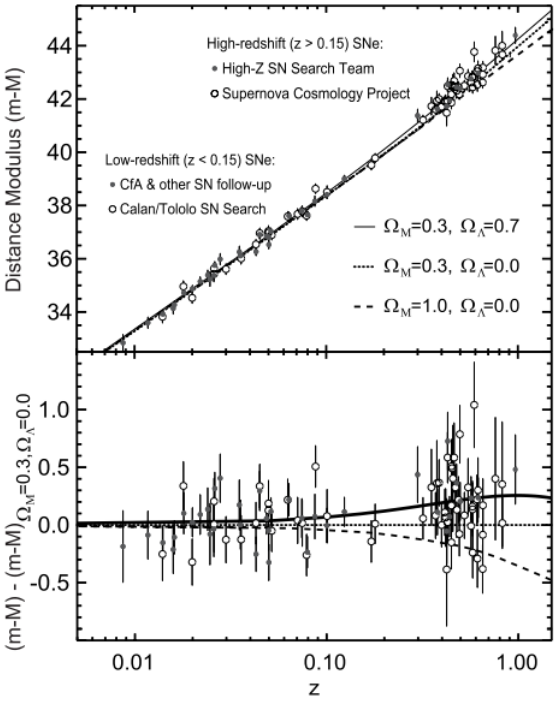

Figure 1.4: Distance modulus versus redshift data from the SNe Ia measurements by the two independent supernova survey teams (The Supernova Cosmology Project and The High-z Supernova Team), showing that a universe dominated by the cosmological constant provides the best fit to the data. Top: The fits to the data, for three different models. Bottom: The distance modulus residuals relative to an open universe with $\Omega_{\rm m} = 0.3$ and $\Omega_\Lambda = 0$. The plots are adapted from Perlmutter & Schmidt (2003) and Riess (2000). Credit: Frieman, Turner & Huterer (2008).

provided direct evidence that the Universe accelerated in its expansion in the last 5 Gyr. These results were best fit by a flat universe with $\Lambda > 0$ and $\Omega_\Lambda > 0$ (Figure 1.4).

Other lines of independent evidence have since provided further support for cosmic acceleration, apart from the CMB measurements which suggest a non-zero cosmological constant (de Bernardis et al., 2000; Hanany et al., 2000). For example, measurements of the geometric BAO distance ratios within the WiggleZ Dark Energy Survey data require an accelerating expansion with $w < -1/3$ (Blake et al., 2011), the power spectra derived from the 2dF Galaxy Redshift Survey and CMB anisotropies indicate that a significant fraction of dark energy is required for a flat Universe, constraining Ω_Λ to between 0.65 and 0.85 within the 2σ range (Efstathiou et al., 2002; Percival et al., 2002), and the detection of the late integrated Sachs-Wolfe (ISW) effect that is expected as a result of accelerated cosmic expansion (Scranton et al., 2003; Giannantonio et al., 2006).

The nature of dark energy is less understood and explored than that of dark matter. While it is often assumed to be zero-point radiation energy of empty space, which naturally

arises out of quantum field theory, the prediction for the value of ΛCDM under this assumption is approximately 30 orders of magnitude larger (although some sources claim a discrepancy of 120 orders depending on the choice of mass scale when expressing the energy density of Λ) than the value derived from observations (Carroll, 2001). Although there are ways around this discrepancy, for example by invoking an almost equally large cancelling term (which requires its own explanation, as it has no theoretical motivation), the mismatch between theory and observations reveals a fundamental ignorance of the nature of dark energy.

This has motivated a number of alternative characterisations of dark energy. Popular alternatives to the ΛCDM model of dark energy are those featuring dynamical dark energy, in which the density of dark energy changes with time, and modified gravity models, which involve altering the field equations rather than invoking a mysterious form of vacuum energy.

1.4 The Success of ΛCDM

Since the establishment of the ΛCDM model, multiple lines of evidence have emerged in support of it, firmly entrenching it as the Standard Model of Cosmology.

Some of the most significant pieces of evidence in support of the ΛCDM model come from measurements of the CMB, which is the residual radiation left over after matter and photons decoupled during the recombination era of the Universe (when nuclei and electrons combined to form neutral atoms). The detailed features, especially in the temperature fluctuations, contain information on the distribution, and other characteristics, of matter at the time of decoupling. The temperature anisotropies can be decomposed into an angular power spectrum, which show acoustic peaks at approximately equal angular spacing. The height of the third peak is dependent on the dark matter density in the Universe (Ω_{dm}), and the results from the Planck Collaboration confirm the prediction for these peaks by ΛCDM. Specifically, $\Omega_{\mathrm{dm}} \approx 25\%$, providing convincing evidence for the existence of dark matter independently of observations of galaxy or cluster dynamics. Furthermore, Lyman-α forest observations also constrain cosmological parameters (including w, Ω_{m}, the inflationary spectral index and the Hubble parameter, h) (Phillips et al., 2001; Seljak, Slosar & McDonald, 2006).

Another convincing piece of evidence comes from measurements of BAOs, which are regular, periodic fluctuations in the density of baryonic matter across the Universe. They are expected to arise because of the acoustic oscillations in the baryon-photon fluid in the early Universe before recombination, and to contain information about the average matter density and the Hubble constant in the Universe. Evidence for these oscillations were found in the angular power spectrum, and the average matter density derived from them confirm the existence of dark matter in the quantities expected. BAOs are also weakly seen in the large-scale structure, and these measurements add another line of evidence to the dark matter paradigm of ΛCDM.

In addition to providing evidence for accelerated cosmic expansion, the Type Ia supernovae measurements also provide an estimate of the total dark matter density, if we assume that the cosmological constant explanation for accelerated expansion, and the dark energy density derived from this assumption, is correct. These estimates are consistent with estimates derived from the CMB.

However, it is important to note that the interpretation of the CMB power spectrum and the Type Ia supernovae measurements, and hence the derivation of the dark matter and matter densities, are dependent on the cosmological model assumed. What these results show is that the ΛCDM cosmological model is consistent with these observations, rather than that ΛCDM is the correct underlying cosmology of our Universe.

1.5 Beyond the Standard Model

Despite the great success of ΛCDM in accurately predicting large-scale features of the Universe, the standard model nevertheless contains a number of problems in need of satisfactory explanation. The existence of these problems have led to the development of extensions to the model, and entirely alternative models. Here we review some of the issues within the standard model, followed by alternative cosmological models developed to address these issues.

One of the concerns over ΛCDM are the discrepancies that exist between its predictions (from simulations) and observations on galactic scales. For example, ΛCDM does not naturally predict the planar distribution of the satellite galaxies observed in the Local Group, for example the Vast Polar Structure (Pawlowski, Pflamm-Altenburg & Kroupa, 2012; Pawlowski, 2018) and the Great Plane of Andromeda (Ibata et al., 2013; Conn et al., 2013; Ibata et al., 2014a; Pawlowski & Kroupa, 2014), and these distributions cannot be explained by accounting for baryonic physics (Ahmed, Brooks & Christensen, 2017). Intriguingly, most of the satellite galaxies around Andromeda also appear to be co-rotating, and their angular momenta are approximately perpendicular to the position vector from the Milky Way to Andromeda (Ibata et al., 2013). Strong alignments are also seen non-locally, within galaxy survey data (Yang et al., 2006; Li et al., 2013; Ibata et al., 2014a), but are only expected to appear at a very low rate in ΛCDM simulations (see Pawlowski et al., 2014; Ibata et al., 2014b), suggesting that modifications must be made to galaxy formation theories, ΛCDM, or both.

Simulations of ΛCDM also predict too many dark matter subhaloes in large galaxies such as the Milky Way, compared to the number of satellite galaxies observed. Many of these subhaloes have predicted densities that exceed the estimated densities of the satellite galaxy haloes. This is the so-called ‘too big to fail problem’, because if the cold dark matter predictions are correct, then these large subhaloes would be too massive to not host a stellar population (Boylan-Kolchin, Bullock & Kaplinghat, 2011, 2012). If they exist, they should be observable. Although properly accounting for baryonic physics improves the agreement between the cold dark matter prediction and observations (Sawala et al., 2016), alternatives to the cold dark matter paradigm, such as warm dark matter in the

form of sterile neutrinos, are capable of even better agreement with observations (Lovell et al., 2017). Self-interacting dark matter models and mixed dark matter models may also adequately resolve this problem (Vogelsberger, Zavala & Loeb, 2012; Marsh & Silk, 2014).

A related issue with the standard model is that it overestimates the number of satellite dwarf galaxies around galaxies the size of the Milky Way (e.g. Klypin et al., 1999; Moore et al., 1999; Springel et al., 2008). ΛCDM simulations are unable to reproduce observed numbers, leading to what is known as 'the missing satellite' problem. This problem may partially be due to the difficulty in detecting very faint objects like dwarf galaxies, and can naturally be eliminated by properly modelling feedback processes and their effects (i.e. removal of gas from feedback processes in the host galaxy may reduce the number of visible satellites that can form; see Bullock, Kravtsov & Weinberg, 2000; Benson et al., 2002; Nickerson et al., 2011, 2012; Brooks et al., 2013; Sawala et al., 2016). However, the discrepancy could also be addressed by modifications to the standard model's characterisation of dark matter and/or gravity. Warm dark matter models may offer a solution to the missing satellite problem by increasing the free-streaming length of dark matter particles, which dampens structure formation on small scales, thus reducing the number of dwarf satellite galaxies (Lovell et al., 2012; Schneider et al., 2012; Power, 2013; Lovell et al., 2014; Elahi et al., 2014). However, it is worth noting that certain studies also suggest that warm dark matter is not enough to resolve all inconsistencies on the small scale (Schneider et al., 2014), though these tensions may be addressed by a mixture of cold and warm dark matter (e.g. Anderhalden et al., 2013).

ΛCDM N-body simulations containing collisionless dark matter are also unable to accurately reproduce the dark matter density profiles deduced from observations of low-mass galaxies (for details, see de Blok, 2010). This is known as the core-cusp problem, because simulations predict the density of dark matter haloes to rise quickly at small radii into a cusp-like shape, while rotation curve measurements suggest the haloes flatten out around the centre (Dubinski & Carlberg, 1991; Navarro, Frenk & White, 1996, 1997). As with the 'missing satellites' problem, multiple solutions have been proposed to solve the core-cusp problem. Some studies show that including more detailed baryonic feedback processes, such as Active Galactic Nuclei and supernovae feedback, has the effect of flattening out the cusp shape, as a result of energy transfers between the gas and the dark matter particles, pushing them into more energetic orbits further from the centre (Navarro, Frenk & White, 1996; Pontzen & Governato, 2012; Brooks & Zolotov, 2014; Brooks et al., 2017). Other studies however, show that changing the nature of dark matter can also solve this problem. Specifically, warm dark matter models, mixed dark matter models and self-interacting dark matter models also produce dark matter cores consistent with observations (Lovell et al., 2012; Anderhalden et al., 2013; Elbert et al., 2015).

A different issue of ΛCDM is the unexplained discrepancy between the values of H_0 measured from the CMB spectrum (Planck Collaboration et al., 2016a), and from local measurements, such as Cepheid data (Riess et al., 2016). Additionally, since σ_8 (the value of the matter fluctuation amplitude on the $8\ h^{-1}$ Mpc scale) is correlated with H_0,

there is also a discrepancy between the measured values of σ_8 at high and low redshifts. Specifically, the constraints provided for the $\Omega_{\rm m}$-σ_8 plane provided by Planck data are different from the constraints from the thermal Sunyaev-Zel'dovich cluster counts (Planck Collaboration et al., 2014b, 2016b,d) and weak lensing of galaxies (Heymans et al., 2012), which are complementary probes of the cosmic matter density. Recent work has shown that these tensions can be reduced with dark matter-neutrino interactions (e.g. Di Valentino et al., 2018) and coupled dark energy models featuring the decay of dark energy into dark matter can resolve the tension entirely (e.g. Murgia, Gariazzo & Fornengo, 2016).

The ΛCDM model is also afflicted by the theoretical problems associated with its characterisation of dark energy. Although the cosmological constant, representing vacuum energy, is the mathematically simplest way of explaining the accelerated expansion of the Universe, dark energy could fundamentally be more complex than this. Indeed, the simple assumption has led to what is known as 'the worst theoretical prediction' in the history of physics!

Quantum field theories predict very large values for the cosmological constant corresponding to the quantum vacuum, with $\Lambda \sim 6 \times 10^{54}$ eV^2 for a Universe described by an effective local quantum field theory down to the Planck scale. This prediction is between $\sim 10^{30}$ times and $\sim 10^{120}$ times larger than the observationally derived value of Λ (depending on choice of mass scale). Although supersymmetry (if valid) could reduce this discrepancy, it still leaves a significant mismatch. The question that arises from the cosmological constant problem is whether there is another unknown form of energy that almost exactly cancels out the contributions predicted for the quantum vacuum, resulting in the very small observed value of Λ. This leads to a fine-tuning problem: if there are multiple contributions to the effective cosmological constant (e.g. vacuum energy, zero-point energies of existing fields), then why do they so nearly cancel each other out? Furthermore, there is no known way to derive this small value for Λ from theory. The standard characterisation of dark energy is clearly incomplete. ΛCDM is simply the best characterisation we have.

The cosmological constant characterisation also leads to the cosmic coincidence problem, which arises because the density of matter in the Universe today is of the same order of magnitude as the density of dark energy. According to the ΛCDM model, the matter and dark energy densities evolve quite differently and independently, with Ω_Λ staying constant while $\Omega_{\rm m}$ declines with time. Hence, there should only be a small window of opportunity for the two densities to have similar values, as displayed in Figure 1.5, and yet coincidentally this is exactly what we observe today. For this intersection of densities to occur at $z \approx 0.39$ is extremely important for the evolution of the Universe. If dark energy had begun to dominate even slightly earlier, then structure formation could not have continued and life would never have appeared. On the other hand, if dark energy had begun at a slightly later epoch, then the Universe would not be expanding at an accelerated rate today, and we never would have discovered it. For humanity to exist and discover the accelerating cosmic expansion, the dark energy domination can only have begun at approximately the current epoch.

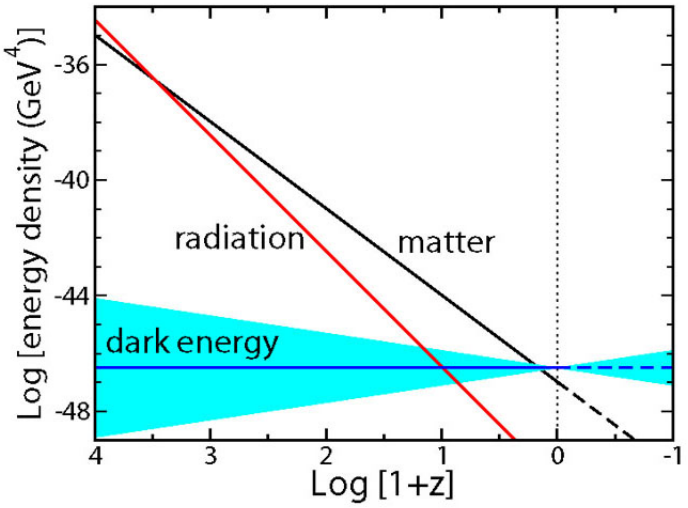

Figure 1.5: A plot showing the evolution of the matter, dark energy and radiation densities with redshift in the ΛCDM cosmology. The matter and dark energy densities follow different trajectories through time, and have similar values only at the current epoch. The teal band represents the dark energy densities corresponding to $w = -1 \pm 0.2$. Credit: Frieman, Turner & Huterer (2008).

Attempts to explain this cosmic coincidence have invoked the Anthropic Principle and the existence of a multiverse. However, the Anthropic Principle does not fully explain the comparability between the dark energy and matter densities, because the conditions required for observers such as ourselves to arise is not extremely dependent on the specific value of Λ in our Universe. Star formation rates and structure formation as observed in our Universe can theoretically be produced by a wide range of values for Λ, meaning that the specific value of Ω_Λ is not particularly special (Salcido et al., 2018; Barnes et al., 2018). Fortunately, there is an alternative explanation: that the ΛCDM model assumptions are wrong, and the evolution of the matter and dark energy densities are in fact closely linked. This idea has led to the development of alternative models, or extensions to ΛCDM, which will be discussed in the next chapter.

Finally, although ΛCDM has been an extremely successful framework for explaining the large-scale features of the Universe and their evolution, it is an incomplete model that fails to provide a deeper understanding of the nature and source of either dark matter or dark energy. For this reason, interest in cosmological models with alternative dark sector physics, so-called 'beyond-ΛCDM models', has increased in recent times. The current hope is that these models leave unique and observable imprints, so that we can observationally distinguish between competing models, and hone in on the properties of dark matter and dark energy.

1.6 The Aims and Scope of this Thesis

Currently, the standard model for cosmology does not provide a theoretical understanding of either dark matter or dark energy. Although there are alternative models that could offer further insight into their physical nature, the landscape of cosmological models is vast and varied. The best way to constrain the possibilities for our Universe, and probe the nature of the dark sector, is to compare the predictions made by these models to the observed features in the Universe. The aim of this work was to find unique signatures of alternative cosmological models from cosmological simulations of these models, so that in the near future, observations made by large-scale surveys can be used to constrain or rule out various models of dark sector physics.

In this work, I focused on finding the observational signatures of two alternative cosmological models: an uncoupled or pure quintessence model and a coupled dark energy model, two relatively simple extensions of ΛCDM that resolve some major issues with the standard model. To derive these signatures, I made use of hydrodynamical N-body simulations of universes governed by these two models, as well as a reference simulation of the ΛCDM model, to identify unique imprints of alternative dark sector physics. I focused my search for cosmological signatures on the features of the large-scale structure, specifically the properties of cosmic voids, which are large underdense regions in the Universe.

This thesis is structured as follows. In Chapter 2, I lay down the landscape for alternative cosmological models, and explain the specific alternative models we investigated, as well as the simulations developed to bring them to life. In Chapter 3, I motivate the use of voids as observational probes of cosmology, and introduce the Hessian-based void finder that I developed to identify voids in the simulations. In Chapters 4 and 5, I present the results of my search for signatures of alternative cosmological models at low and high redshifts, within the properties of cosmic voids. These results are presented in the form of two published papers in peer-reviewed journals, followed by extended discussion on the implications of my results in constraining other cosmological models beyond the ones studied in this work. I also propose a number of methods to take advantage of imprints of cosmology in upcoming large-scale surveys. In Chapter 6, I will summarise and conclude this thesis, and discuss possible avenues for further research arising from the results of my work.

CHAPTER 2

Beyond ΛCDM: Evolving and Interacting Dark Sector Universes

2.1 Alternative Cosmological Models

The shortcomings of the ΛCDM model have motivated the development of a multitude of alternative cosmological models. In this section, we discuss a few of these models, specifically models with a dynamical dark energy component, modified gravity models, and models featuring alternatives to cold dark matter.

2.1.1 Dynamical Dark Energy

In place of the cosmological constant, dynamical dark energy models allow the dark energy field to vary with time. A well-known class of dynamical dark energy models are the quintessence models. Quintessence models assume the presence of a time-dependent and spatially homogeneous scalar field, ϕ, with a potential $V(\phi)$, which drives the accelerated cosmic expansion, akin to the proposed inflationary scalar fields (Ratra & Peebles, 1988). The equation of state for the scalar field is given by $w = p_\phi/\rho_\phi$, where p_ϕ and ρ_ϕ denote the pressure associated with the scalar field and the density of the scalar field, respectively. For most quintessence models, the equation of state satisfies the condition $-1 < w \leq 0$, and varies with time. The history (and future) of the Universe under a quintessence cosmology is therefore substantially different from the history (and future) predicted by ΛCDM, where $w = -1$ at all times.

Quintessence models are also subject to the fine-tuning problem, as the energy density of the scalar field must still be equal to the dark energy density today, and this normally requires both $V(\phi)$ and the initial value of ϕ and its time derivatives to be quite specific, or in other words, fine-tuned. Fortunately, there exists a class of quintessence models called 'tracker' models (Zlatev, Wang & Steinhardt, 1999; Steinhardt, Wang & Zlatev, 1999), which are completely insensitive to the initial value of the field and its time derivatives,

thereby addressing the fine-tuning problem. Furthermore, these models enable the scalar field energy density to track the matter density so that they naturally have similar values today, thereby addressing the cosmic coincidence problem (for further explanation of how this works, see Steinhardt, 2003).

Quintessence models can be extended to include non-gravitational interactions between the scalar field and the matter field. These models are called Coupled Dark Energy models (e.g. Amendola, 2000). In these models, energy and momentum are transferred between dark energy and the matter field. Couplings usually exist between the scalar field and the dark matter field, but can also occur between the scalar field and the overall matter field (including baryons), or the scalar field and the neutrino field (e.g. Takahashi & Tanimoto, 2006; Mota et al., 2008; Amendola, Baldi & Wetterich, 2008), where the neutrino mass is ϕ-dependent. These couplings can take various forms. For example, dark matter may decay into the scalar field and thus increase the dark energy density, or the scalar field can decay into dark matter and increase the overall matter density.

The coupling between dark sector components alters the expansion history of the Universe and the growth of perturbations in the density field compared to ΛCDM. However, CMB observations, BAO measurements, Type Ia supernovae data, Hubble parameter measurements and other considerations can still be consistent with these models as long as their model parameters are appropriately constrained (see Pettorino, 2013; Xia, 2013; Planck Collaboration et al., 2016c; van de Bruck, Mifsud & Morrice, 2017). With coupling between dark energy and dark matter, coupled models are also able to resolve the coincidence problem by including a mechanism by which the dark energy density is dependent on the total matter density. Recent studies have also indicated certain observational data favour coupled models over either ΛCDM or pure, uncoupled quintessence (e.g. Pourtsidou, Skordis & Copeland, 2013).

2.1.2 Modified Gravity

Another way to produce accelerated cosmic expansion is to modify the equations describing gravity themselves (for a review, see Jain & Khoury, 2010). One possible method of achieving this is to modify the Ricci scalar, R, in the action giving rise to Einstein's field equations (Einstein-Hilbert action), to $f(R)$, a function of the Ricci scalar R. This formalism is referred to as $f(R)$ gravity, and incorporates a family of models each defined by the specific form of $f(R)$. These models were first introduced by Buchdahl (Buchdahl, 1970), as a generalisation of the Einstein-Hilbert action, and later gained traction after they were used in the context of inflationary cosmology as a possible driver of inflationary expansion (Starobinsky, 1980). As it turns out, quantum corrections to GR naturally produce $f(R)$ models (e.g. Birrell & Davies, 1984; Buchbinder, Odintsov & Shapiro, 1992; Vilkovisky, 1992), whose solution when curvatures are large involves an effective cosmological constant that drives inflation.

The generalisation to $f(R)$ introduces additional degrees of freedom that also produce an effective cosmological constant, giving rise to accelerated expansion at late times with-

out invoking a form of dark energy. Some $f(R)$ models also modify the Poisson equation, thus altering the relation between the energy density and the associated gravitational potential to include some dependence on local curvature and offering an alternative explanation for structure formation without the need for some form of dark matter. However, not all models are viable cosmological models for our Universe, either because they do not match observations or they produce theoretical problems. For example, the very first $f(R)$ model proposed to explain late-time cosmic acceleration (of the form $f(R) = R - \mu^4/R$, where $\mu \sim 10^{-33}$ eV) was ruled out because it violates tests of GR (Chiba, 2003) and contains catastrophic instabilities (Dolgov & Kawasaki, 2003). Furthermore, some $f(R)$ models exhibit curvature singularities (Frolov, 2008), while others offer no physical solutions for the field equations beyond the special case of GR (Barausse, Sotiriou & Miller, 2008). Constraining viable models can be difficult due to the large number of possible forms of $f(R)$, the complexity of finding solutions to the modified field equations, and because deviations from GR can be made arbitrarily small for some models in order to match observations.

Other modified gravity theories include Galileons, massive gravity theories and scalar-tensor theories. Galileons are a class of modified gravity theories that contain a self-interacting scalar field and whose Lagrangian is invariant under Galileon symmetry, which removes instability and other problems that plague other modified gravities (Nicolis, Rattazzi & Trincherini, 2009). Massive gravity and its extensions modify GR at large scales, by introducing a non-zero mass to the graviton, in order to produce accelerated cosmic expansion without introducing dark energy (see de Rham, Gabadadze & Tolley, 2011). This also forces gravitational waves to travel at less than the speed of light. Scalar-tensor theories offer a natural framework in which a massless scalar field is linked to the gravitational field, while also preserving the coupling of matter and gravity present in GR (e.g. Brans-Dicke theory; Brans & Dicke, 1961). These models are referred to as scalar-tensor, because GR is a tensor theory (the metric is a spin-2 tensor), while the addition of a linked scalar field provides the scalar component. They are of particular interest because they also arise naturally out of unification theories that include gravity (e.g. Jordan's Projective Relativity theory; Jordan, 1955, and string theory; Damour & Vilenkin, 1996). Many of these models also tend to approach GR at the current time, making them consistent with observations that support it, while some also offer an alternative to dark matter, instead explaining cluster and rotation dynamics through modified gravitational interactions.

The additional scalar degrees of freedom introduced as part of these modifications are expected to couple to matter and thereby produce an observable fifth force. Such a force has never been observed in local tests of gravity (e.g. tests of the Strong Equivalence Principle within the Solar System; Williams, Turyshev & Boggs, 2009, 2012), so many modified gravity theories require a 'screening mechanism' in their formalism to achieve consistency with local observations (for example, the Vainshtein mechanism, which includes non-linear derivative self-interactions to suppress the fifth force; Vainshtein, 1972, and the chameleon mechanism, which increases the mass of the scalar field in regions of high density; Khoury

& Weltman, 2004). The screening allows the fifth force introduced by additional degrees of freedom (e.g. scalar fields coupling to matter with gravitational strength) to produce accelerated cosmic expansion on cosmological scales, while suppressing its effects on small scales. These mechanisms apply to $f(R)$ gravity, Galileons, massive gravity theories, scalar-tensor theories, and other modified gravity theories.

It is worth noting that the interpretation of the scalar fields in modified gravity theories is not the same as the interpretation of the scalar field in quintessence models. In quintessence, the scalar field appears as a source of energy in the stress-energy tensor, rather than as an alteration to the behaviour of the gravitational force in modified gravity. However, the distinction can be considered inconsequential, as will be discussed in greater detail in Chapter 5. It is also worth highlighting that some $f(R)$ models behave like quintessence models, where the particular alteration to the Einstein-Hilbert action produces an expansion history and a modified Poisson equation that mimics the effect of a quintessence scalar field. This similarity in behaviour will also be further explored in Chapter 5.

2.1.3 Dark Matter Models

Apart from modifications to gravity or alternative formulations of dark energy, other popular beyond-ΛCDM models exist to address different shortcomings of the standard model or provide tests of dark matter candidates. These include warm dark matter models, mixed dark matter models, self-interacting dark matter models, and models that modify gravity without invoking a new form of matter.

Despite the evidence in favour of the cold dark matter paradigm, a number of discrepancies between its predictions and observations have led to interest in warm dark matter models, which encompass dark matter candidates such as sterile neutrinos and axions. It has been suggested that warm dark matter, with a free-streaming length between cold and hot dark matter, could alleviate some of these tensions, for example the excess of dark matter velocity dispersion in the inner parts of Milky Way satellites (the 'too big to fail' problem Boylan-Kolchin, Bullock & Kaplinghat, 2012), and the cuspiness of galactic cores (de Blok, 2010). These tensions occur on the small scale, which warm dark matter may be able to address through its larger average velocity and hence greater free-streaming length, which would act to suppress structure on Mpc scales and below (e.g. de Vega, Salucci & Sanchez, 2012; Lovell et al., 2012, 2014). However, constraints from the Lyman-α flux power spectrum require warm dark matter to be almost indistinguishable from cold dark matter on the relevant scales, and hence warm dark matter models cannot resolve the small-scale problems of the cold dark matter paradigm without some modifications, such as including both cold and warm dark matter components (mixed dark matter models) or by altering the warm dark matter power spectrum so that it gradually decreases on the small scale (Viel et al., 2013; Schneider et al., 2014). Mixed dark matter models have enjoyed some support as an alternative to cold dark matter because they can also solve key small-scale structure problems, including the problem of cuspiness in galactic cores and the 'too big to fail' problem, while remaining consistent with the Lyman-α constraints (e.g.

Anderhalden et al., 2012, 2013; Marsh & Silk, 2014; Kamada, Inoue & Takahashi, 2016).

Self-interacting dark matter was originally introduced to address the core-cusp problem and the 'missing satellites' problem (Spergel & Steinhardt, 2000). In this paradigm, cold dark matter is no longer collisionless. Instead, it has weak interactions with baryons and strong interactions with itself. Dark matter particles self-interact by scattering elastically off each other through $2 \rightarrow 2$ interactions, with a small velocity-dependent cross-section constrained by observations such as those within the Bullet Cluster (Randall et al., 2008). This addition to the cold dark matter model results in differences in the inner structure of haloes compared to cold dark matter, while retaining the successes of cold dark matter on large scales. For example, the presence of collisions between dark matter particles causes the central density within haloes to flatten out as a result of the redistribution of energy and angular momentum, which addresses the core-cusp problem (Rocha et al., 2013; Peter et al., 2013). Self-interacting dark matter models also offer solutions to the 'too big to fail' problem (Vogelsberger, Zavala & Loeb, 2012) and the problem of dark matter deficits across a range of scales (Kaplinghat, Tulin & Yu, 2016), as well as an explanation for the diversity of galactic rotation curves (Kamada et al., 2017). One example of self-interacting dark matter is the Strongly Interacting Massive Particle, though other possibilities include particles interacting through a Yukawa potential (Loeb & Weiner, 2011).

Although attention is focused mostly on finding dark matter particle candidates, it has also been proposed that dark matter does not exist at all, and the mass inconsistencies observed in galaxy and cluster dynamics could instead be due to an incomplete understanding of gravity. These models include MOND (Modified Newtonian Dynamics; Milgrom, 1983), TeVeS (Tensor-Vector-Scalar theory, a relativistic generalisation of MOND; Bekenstein, 2004) and other generalisations of MOND. Although MOND was originally successful in explaining galaxy dynamics, explaining dynamics on the scale of clusters was more difficult (e.g. Bullet Cluster observations), and explaining the peaks in the CMB angular power spectrum proved to be even more challenging. The model is both incomplete and ineffective, and as a result is heavily disfavoured as an alternative to dark matter. TeVeS is able to explain cluster-scale dynamics by invoking other sources of gravitational potential besides dark matter, and explain the CMB power spectrum peaks through tweaking additional degrees of freedom. However, both of these explanations are more complicated than dark matter explanations. TeVeS is also tightly constrained by the recent gravitational wave results from GW170817 (Boran et al., 2018) as well as large-scale structure measurements (e.g. Reyes et al., 2010), as are other generalisations of MOND (such as Generalized Einstein-Aether Theory and bimetric MOND), by gravitational wave results from GW150914 (Chesler & Loeb, 2017). Despite this, interest in variations of MOND has not completely subsided, and it remains a possibility that some version of MOND/TeVeS could convincingly explain these observations without invoking a new form of matter.

It is worth noting that the very recent gravitational wave observations from GW170817 (Abbott et al., 2017b) have shown that gravitational waves travel at light speed (Abbott et al., 2017a), which provides a strong constraint on the number of alternative models that could describe our Universe. Specifically, quartic and quintic Galileons, generalised

scalar-tensor theories, and quartic and quintic Horndeski theories, are among the models predicting non-light speed gravitational waves, and have consequently been ruled out (see Creminelli & Vernizzi, 2017; Ezquiaga & Zumalacárregui, 2017; Baker et al., 2017). Aside from TeVes and MOND-like theories, many modified gravity theories which do not include dark matter are also severely constrained by these results (e.g. Boran et al., 2018). Quintessence and coupled dark energy models have not been ruled out, and in this thesis, we will present methods of constraining some of these models through observations.

2.2 Quintessence Models

We investigated two non-standard cosmological models featuring dynamical dark sectors: an ***uncoupled quintessence model (ϕCDM)*** and a ***coupled dark energy model (CDE)***.

These models differ from ΛCDM in their characterisation of dark energy. In both models, accelerated cosmic expansion is the result of an evolving scalar field, ϕ, instead of a cosmological constant in Einstein's field equations, Λ. The coupled dark energy model contains an additional differentiating feature, which is that dark matter particles can decay into the scalar field.

The general Lagrangian for these quintessence models is given by

$$L = \int \sqrt{-g} \left(-\frac{1}{2}\partial_\mu \partial^\mu \phi + V(\phi) + m(\phi)\psi_m \bar{\psi}_m \right) d^4x, \tag{2.1}$$

consisting of a kinetic term, $-\frac{1}{2}\partial_\mu\partial^\mu\phi$, a potential term to describe the scalar field's self-interactions, $V(\phi)$, and a coupling term that describes the interaction between the scalar field and the matter field, $m(\phi)\psi_m\bar{\psi}_m$. The term $\psi_{\rm m}$ represents the total matter field, which includes the dark matter field, the baryonic matter field and the neutrino field. Since dark matter, baryons and neutrinos can each couple to the scalar field in a CDE model, the full expression for the interaction term, $m(\phi)$, includes expressions for the individual interactions between the scalar field and dark matter, baryons and neutrinos. For our CDE model, only the coupling between dark matter and the scalar field is non-zero. For the uncoupled quintessence model, $m(\phi) = 0$.

There are a large number of different definitions available for $V(\phi)$ that result in different expansion histories for the universe. For this work, we use a simple inverse power of the scalar field, known as the Ratra–Peebles potential:

$$V(\phi) = V_0 \phi^{-\alpha}, \tag{2.2}$$

for our alternative cosmological models, where V_0 and α are constants (with $\alpha > 0$) that are determined by fits to observational data.

The Ratra–Peebles potential was originally introduced to describe a near-homogeneous real scalar field (which also gave rise to inflation at early times) with an energy density that declines to zero over time, in order to explain why the observed energy density associated with the cosmological constant is so small at the current epoch (Ratra & Peebles, 1988). If

$\alpha = 0$ in Equation 2.2, the scalar field reduces to a cosmological constant. If $\alpha > 0$, the inverse power-law potential produces a tracker solution for ϕ, which allows a large range of initial scalar field energy densities to arrive at the observed small density today, and for some solutions also enables the scalar field density to stay close to the background energy density during the radiation- and matter-dominated epochs (Steinhardt & Caldwell, 1998; Steinhardt, Wang & Zlatev, 1999), addressing both the quintessence fine-tuning problem and the cosmic coincidence problem.

As the scalar field is time-dependent, the equation of state and the energy density are also time-dependent. The density, ρ_ϕ, and the pressure, p_ϕ, of the scalar field are given by

$$\rho_\phi = \frac{1}{2}\dot{\phi}^2 + V(\phi) \quad \text{and} \quad p_\phi = \frac{1}{2}\dot{\phi}^2 - V(\phi), \tag{2.3}$$

respectively, where $\dot{\phi}$ is the first derivative of ϕ with respect to time. These expressions correspond to the diagonal elements of the stress-energy tensor associated with the scalar field, for an observer who sees the universe as isotropic, and are true for a scalar field that has no spatial variation and no anisotropic stress. The equation of state is then given by

$$w_\phi = \frac{p_\phi}{\rho_\phi} = \frac{\frac{1}{2}\dot{\phi}^2 - V(\phi)}{\frac{1}{2}\dot{\phi}^2 + V(\phi)}. \tag{2.4}$$

Assuming a spatially isotropic, homogeneous universe and minimal coupling, the scalar field satisfies the following continuity equation:

$$\dot{\rho_\phi} + 3H(\rho_\phi + p_\phi) = 0, \tag{2.5}$$

where H is the Hubble constant and $\dot{\rho_\phi}$ is the time derivative of the scalar field density.

Substituting the definitions for ρ_ϕ and p_ϕ from Equation 2.3 into Equation 2.5, we obtain the equation of motion for the scalar field ϕ:

$$\ddot{\phi} + 3H\dot{\phi} + \frac{dV(\phi)}{d\phi} = 0, \tag{2.6}$$

where $\ddot{\phi}$ is the second derivative of ϕ with respect to time.

In order to produce accelerated cosmic expansion, the pressure produced by the scalar field evolution must be negative, which requires that the kinetic energy term in Equation 2.3, $\frac{1}{2}\dot{\phi}^2$, be less than the potential energy term, $V(\phi)$. In other words, the field rolls slowly down the potential. This requirement is indeed satisfied by the Ratra–Peebles potential. We can choose appropriate values of V_0 so that the equation of state satisfies $w < -1/3$, which can be seen by substituting Equation 2.2 into Equation 2.4 and rearranging to give the requirement that $V_0 > \dot{\phi}^2/\phi^{-\alpha}$. The Ratra–Peebles potential also causes the energy density of the scalar field to decrease more slowly with time than the matter and radiation densities, so that the scalar field can dominate at late times (Peebles & Ratra, 2003).

2.2.1 Uncoupled Quintessence

The Lagrangian for the uncoupled or pure quintessence model contains no coupling term, with $m(\phi) = 0$. There is no direct non-gravitational interaction between the scalar field and the matter field. The difference between the standard model and the uncoupled quintessence model is in the time-dependence of ϕ, which not only provides an alternate way of causing accelerated late-time expansion, but also alters the total energy content of the universe, and hence its expansion history compared to the standard model.

2.2.2 Coupled Dark Energy

The coupled dark energy model is an extension of the pure quintessence model. In addition to the changes in expansion history and equation of state associated with introducing the scalar field governed by the Ratra–Peebles potential, the CDE model also features an interaction between the scalar field and the matter field, which results in an altered expansion history compared to uncoupled quintessence, and an altered density perturbation evolution compared to ΛCDM. For our CDE model, we chose the interaction term to be between the scalar field and dark matter only, and given by

$$m(\phi) = m_0 \exp[\beta(\phi)\phi], \tag{2.7}$$

where m_0 is a constant determined by fitting to observational data, and $\beta(\phi)$ is the coupling term that describes the degree of coupling between the scalar field and matter field. We chose $\beta(\phi) = \beta_0 = 0.05$, which is a simple coupling that represents the greatest degree of coupling allowed by observational constraints (see Pettorino et al., 2012; Xia, 2013). This form of coupling allows the dark matter field to decay into the scalar field, while also preserving the tracker feature present in the uncoupled model.

Another important consequence of this interaction term is that dark matter particles behave differently from normal baryonic particles, due to the momentum exchange between dark energy and dark matter. While baryons still obey approximately Newtonian dynamics, dark matter particles are subject to an additional 'drag' force that exists only within dark matter-dark matter interactions. This can be viewed as an altered gravitational interaction, with an altered gravitational constant:

$$G_{\text{eff}} = G(1 + \beta_0^2). \tag{2.8}$$

This corresponds to a fifth force, or a modification to gravity for only dark matter interactions. The interactions between dark matter and baryons remain the same for our choice of interaction term. This results in an offset between the dark matter and baryonic particles in the amplitude of their density perturbations, which alters the evolution of the initial density perturbations, reduces the fraction of baryons in haloes and alters their density profiles compared to ΛCDM (Baldi et al., 2010). The differences in the non-linear power spectrum (and the growth factor evolution and expansion history) between the CDE and ΛCDM models can be seen in Figure 2.1, which also shows the differences between the ϕCDM and ΛCDM models.

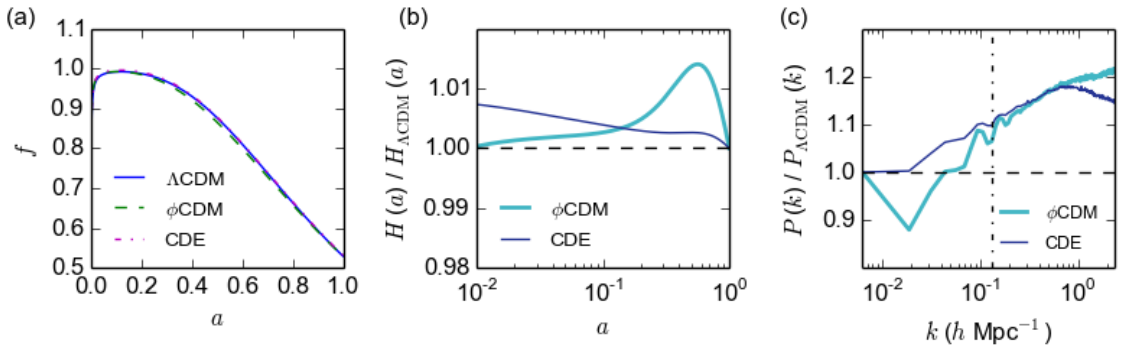

Figure 2.1: Plots showing the differences between the models we simulated: (a) the evolution of the growth factor, f, as a function of scale factor, a (b) the evolution of the Hubble constant relative to the ΛCDM simulation, $H(a)/H_{\Lambda\mathrm{CDM}}(a)$, as a function of a (c) the non-linear power spectrum relative to the ΛCDM simulation, $P(k)/P_{\Lambda\mathrm{CDM}}(k)$, as a function of the wavenumber, k. To the left of the vertical line is the region where the ratios have an error of less than 1%. Both the alternative models exhibit an increased expansion rate relative to ΛCDM except at $a = 1$, with the expansion rate being the greatest for pure quintessence at late times, and for the coupled model at early times. The differences in the non-linear power spectrum reflect the differences in how the initial density perturbations evolve with time in the alternative models, showing that the pure quintessence model has less large-scale power than the other two models, and that ΛCDM has less small-scale power than the alternative models.

The expansion history is also altered as a result of an additional phase in the history of the universe where the ratio between the dark energy density and the dark matter density remains constant (Amendola, 2000). This leads to a greater early dark energy component present during structure formation than in the uncoupled case (Doran, Schwindt & Wetterich, 2001; Doran & Robbers, 2006), altering the expansion history of the universe at early times compared to the uncoupled quintessence model. Furthermore, increasing the degree of coupling tends to increase the value of the Hubble parameter compared to ΛCDM at high redshifts (Baldi et al., 2010).

As the cold dark matter density evolution is different, the interaction between the dark sectors affects the scale factor at which matter-radiation equality occurs, and thus affects the locations and amplitudes of acoustic peaks of the CMB temperature anisotropies, as well as the turnover scales of the large-scale structure matter power spectrum (Lee, Liu & Ng, 2006). The late ISW effect will also be affected, because the gravitational potential wells that the photons from the CMB traverse have a different time evolution as a result of the altered cold dark matter density evolution, and the specific alteration to the effect depends on the coupling and the direction of energy flow between the sectors (He, Wang & Zhang, 2009; Xia, 2009).

Table 2.1: Parameter values for the Ratra–Peebles potential and coupling in the alternative cosmological models (Carlesi et al., 2014a). The values of V_0 and α are fixed by fitting the models to observational data.

Model	V_0	α	β_0
ϕCDM	10^{-7}	0.143	0
CDE	10^{-7}	0.143	0.05

2.3 Adiabatic Hydrodynamical Cosmological Simulations

The purpose of developing these models is to understand the nature of the dark sector, as well as its effect on the evolution of our Universe. To determine whether any of these models could explain the large-scale features of the Universe as well as, or better than, ΛCDM does, we must derive observational tests for these models. One way of doing this is to run simulations of a universe's evolution under different models of interest, and compare the imprints left by these models on the various features of the universe. Any unique signature of a particular cosmological model that differentiates it from ΛCDM could serve as the basis of observational tests for the model.

Simulations solve the non-linear equations governing the evolution of particles, which are extremely difficult or impossible to solve analytically. They produce a 'mini-universe' that matches a particular set of cosmological equations for us to explore, measure and probe. With simulations, we can provide a means of identifying unique features that exist within a universe governed by the models of interest.

The simulations used in this work are adiabatic hydrodynamical cosmological simulations. Each simulation consists of a three-dimensional box, and contains a number of dark matter particles and baryonic (gas) particles to represent the types of matter in our own Universe. The particles each start at specific locations, and their trajectories are calculated by integrating equations of motion that are determined by Newtonian gravity (with the appropriate gravitational constants for dark matter and baryons in the CDE model), simple gas thermodynamics and the cosmology of the model. Heat exchange and magnetic effects are not included in these simulations, and we neglect star formation, black holes and feedback physics.

The simulations were run in boxes of length 500 h^{-1} Mpc from $z = 100$ to $z = 0$, using a modified version of the P-GADGET-2 N-body code called DARK-GADGET. Each simulation consisted of 2×512^3 dark matter and baryonic particles with masses of 6.9×10^{10} $h^{-1}M_\odot$ and 1.3×10^{10} $h^{-1}M_\odot$ respectively. For CDE, the overall dark matter mass evolves with redshift due to dark matter decay into the scalar field, so this mass resolution applies only at $z = 0$ where we set Ω_m. The defining parameters used for each simulation are summarised in Tables 2.1 and 2.2, while in Figure 2.2, we show the smoothed dark matter density field within a 1 h^{-1} Mpc slice of the ΛCDM simulation, at $z = 0$.

We used a linear Boltzmann integrator called CMBEASY (Doran, 2005) to determine the

Table 2.2: The cosmological parameters used in all three simulations, and the simulation details. $\Omega_{\rm b}$ is the total baryon density, $m_{\rm DM}$ and $m_{\rm gas}$ represent the mass resolutions of dark matter and gas, respectively, and $N_{\rm DM}$ and $N_{\rm gas}$ represent the number of dark matter and gas particles in the simulations, respectively.

Parameter	Value	Parameter	Value
h	0.67	Box Length	$500\ h^{-1}$ Mpc
$\Omega_{\rm m}$	0.3175	$N_{\rm DM}$ & $N_{\rm gas}$	512^3
$\Omega_{\rm b}$	0.049	$m_{\rm DM}$	$6.9 \times 10^{10}\ h^{-1}\ {\rm M}_\odot$
σ_8	0.83	$m_{\rm gas}$	$1.3 \times 10^{10}\ h^{-1}\ {\rm M}_\odot$

initial density perturbations, evolution of cosmological parameters, matter power spectra, growth factors and expansion history for each of the non-standard models, which are all affected by the scalar field and the coupling. The integrator calculates the rate of growth of the initial density perturbations based on cosmological parameters and underlying cosmology, which can then be used to extrapolate the current power spectrum back in time, in order to describe the statistical properties of the initial density field. The initial particle locations are then generated within this density field by perturbing particles placed on a Cartesian grid, with the first-order Zel'dovich approximation, using a modified version of the N-GENIC code (Elahi et al., 2015). For the standard cosmology, the growth factor is computed during the simulation runs.

At each time step, we calculated the gravitational force experienced by the baryons and dark matter particles due to all other matter. For the CDE model, we evolved the dark matter particle mass with time to model the decay of dark matter into the scalar field. Additionally, we accounted for the extra 'drag' force acting on dark matter particles due to other dark matter particles, by including in the force calculations a separate gravity tree containing this additional force.

We ensured that each simulation was initialised with the same phases in their density perturbations, so that all underdensities and overdensities initially occurred in approximately the same locations. This was to reduce differences between the large-scale structures of each simulation arising as a result of cosmic variance. Our simulations also included a gravitational softening parameter of 1/33 of the interparticle spacing, to avoid numerical divergences when particles are very close to each other.

We chose to use $z = 0$ as our normalisation point, so that σ_8, $\Omega_{\rm m}$, $\Omega_{\rm b}$ (the baryon density) and h for the two alternative models matches the values derived for ΛCDM at $z = 0$ by Planck Collaboration et al. (2014a), from CMB observations. This causes the amplitudes of the density perturbations to differ at $z_{\rm CMB}$ (redshift corresponding to the CMB), and the expansion rates in the past to differ between the non-standard models and ΛCDM, so that $z_{\rm CMB}$ is also different between the models.

We note that there is some freedom in defining the values of cosmological parameters such as σ_8 and $\Omega_{\rm m}$ in the alternative models. Alternative models will have their own set of parameters, some of which may be shared by ΛCDM. The shared parameters depend

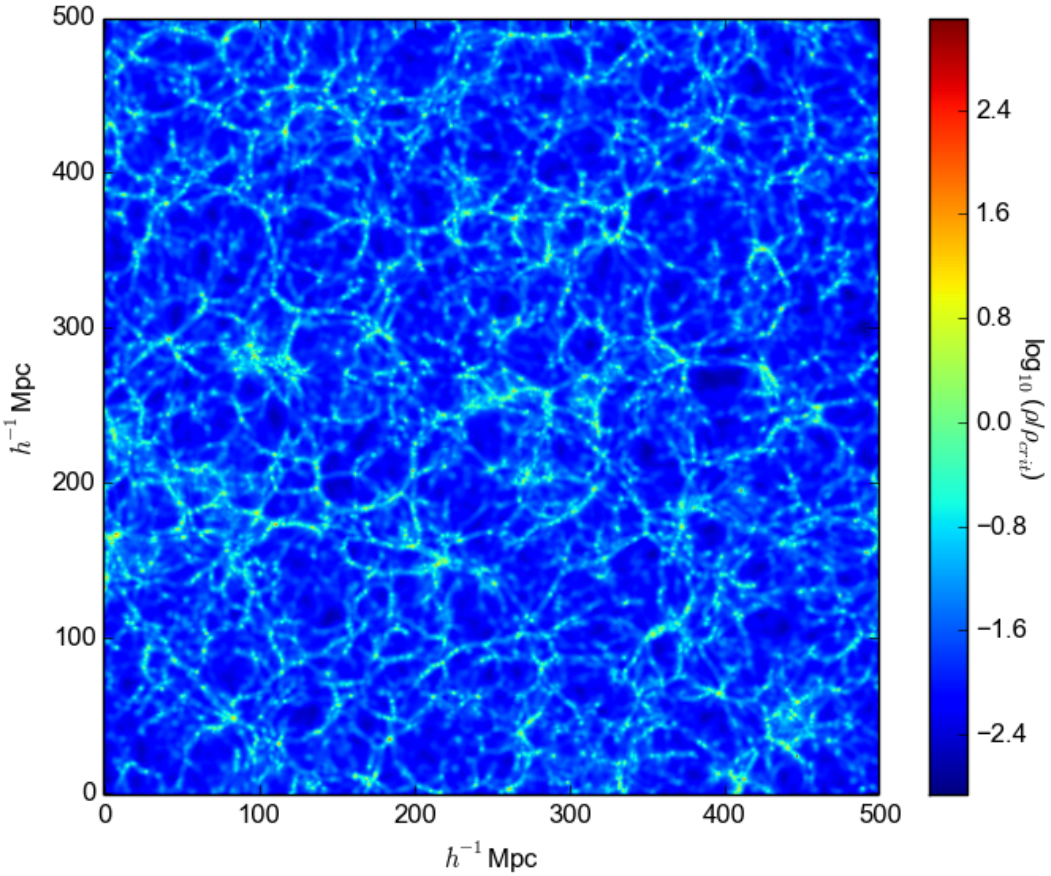

Figure 2.2: The density field of the smoothed dark matter distribution within a 1 h^{-1} Mpc slice of the ΛCDM simulation at $z = 0$, showing the large-scale structure produced by the simulation. The densities, ρ, are given in the form of $\log_{10}(\rho/\rho_{crit})$, where ρ_{crit} is the critical density.

on both the alternative model and on the observational data used to constrain the non-standard parameters. This is because each set of observational data can only constrain certain parameters, while keeping other parameters fixed (and matched to ΛCDM values). Moreover, fitting parameters to observational data can result in values that do not agree with standard model constraints, because the fitting process may involve cosmology-dependent assumptions that differ from those used to derive the ΛCDM parameter values. Thus, there is some freedom in choosing which parameters to constrain by observations (and which parameters to be shared with ΛCDM fits to data). For example, Baldi (2012) chose the parameters of their coupled dark energy models so that the amplitudes of the density perturbations were consistent with ΛCDM amplitudes at $z_{\rm CMB}$, while $\Omega_{\rm b}$ and $\Omega_{\rm m}$ matched ΛCDM values at $z = 0$, causing σ_8 to differ from ΛCDM at low redshift. This is different from our choice, but due to the flexibility in fixing non-standard parameters, neither of our approaches are more valid than the other.

CHAPTER 3

Much Ado About Nothing: Identifying Voids in the Cosmic Web

3.1 The Cosmic Web

The matter distribution in the Universe forms a hierarchical web-like structure on Mega-parsec scales, known as the cosmic web (see Figure 3.1). The cosmic web emerged as a natural consequence of anisotropic collapse over billions of years, which amplified the very small primordial density fluctuations of the initial Gaussian random field. This occurred because at very early times, the small density fluctuations produced imbalances in the gravitational force across the matter field, causing them to accumulate matter and grow over time. As these structures grew, they underwent mergers with each other under the influence of gravity to produce ever-larger structures.

The gravitational force experienced by particles is anisotropic. As densities increase and push the growth of structures into non-linear territory, complex patterns begin to emerge in the density field. The outcome of this is a web-like structure. Over time, the denser structures get smaller and denser, and the low density structures grow larger and emptier.

The cosmic web can naturally be divided into 4 types of structure: knots (or blobs), filaments, sheets and voids. Knots are the highest density regions, usually roughly spherical in shape due to collapsing in all directions, and contain the largest number of dark matter haloes, galaxies and gas; filaments are long dense structures that form links between knots, and are collapsed along two dimensions; sheets are homeomorphic to planar structures, collapsed along only one dimension, and tend to connect filaments and form void walls; and voids are very underdense regions containing little matter, which evacuates out of them in all directions. Under this classification scheme, every particle in the cosmic web may be grouped into one of these four categories of substructures.

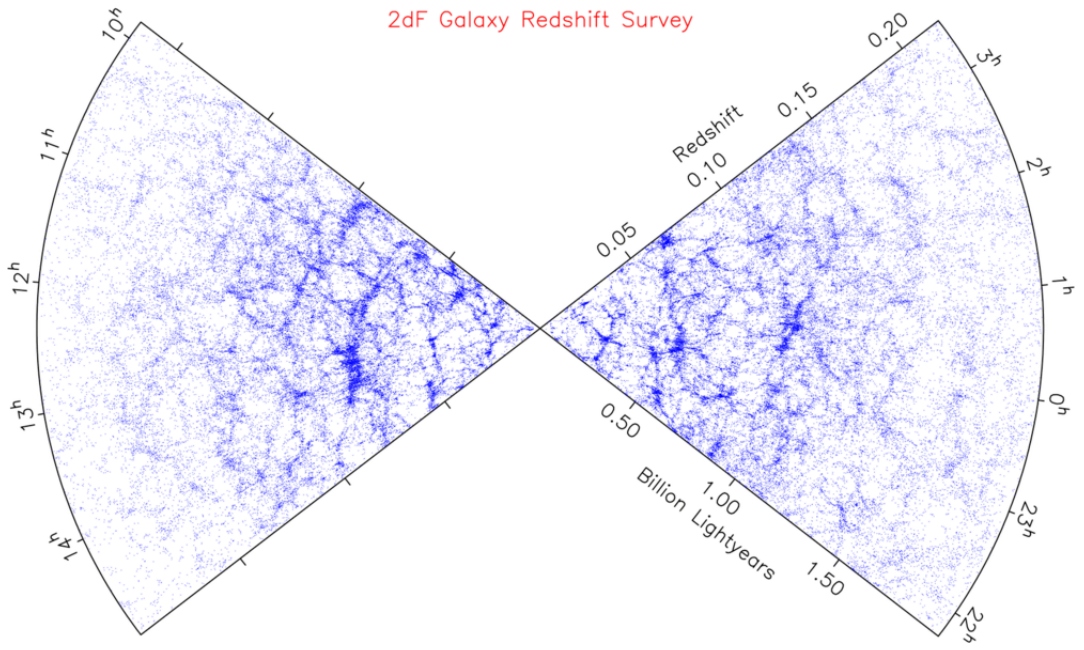

Figure 3.1: Galaxy distribution from the 2dF Galaxy Redshift Survey (Colless, 2004), showing the web-like structure that the galaxies form on Megaparsec scales. Image Credit: Matthew Colless, 2003.

3.1.1 Cosmic Voids as a Probe of Cosmology

Although gravity dominates the evolution of the original density perturbations and their subsequent motions, the growth of the cosmic web is also influenced by the specific cosmology of the Universe. For example, the fifth force that arises from certain cosmological models can affect the net gravitational attraction experienced by massive structures, and additional scalar fields will change the expansion history of the universe. The properties of haloes and filaments are also potentially affected by underlying cosmology, for example from an altered Poisson equation in modified gravity models or an altered initial power spectrum in coupled dark energy models. As such, many studies into the signatures of alternative cosmologies focus on using features of the cosmic web as probes, including halo mass functions (Sutter & Ricker, 2008), gas properties of galaxy clusters (Baldi et al., 2010; Carlesi et al., 2014b) and the topology (overall interconnectedness of underdense and overdense regions) of the large-scale structure (Watts et al., 2017).

Many of the earlier studies focused on the properties and statistics of overdensities in the cosmic web. However, in recent years cosmic voids have become a popular alternative probe of cosmology. Voids are considered ‘cleaner’ environments in which to search for cosmological signatures than denser structures, such as dark matter haloes. Their low densities make them relatively simple, mildly non-linear environments, which are less affected than denser structures by gravitational interactions, gas physics and complex feedback physics that could mask any effect that dark sector physics has on their growth

and their properties. In contrast, the evolution of overdense structures is heavily influenced by gravitational interactions and gas physics, making subtle imprints difficult to distinguish from non-cosmological effects. In theory, cosmological signatures within cosmic voids should be easier to identify than those within overdense structures, making them ideal cosmological probes. For this reason, the work in this thesis makes use of cosmic voids as probes of cosmology.

3.2 Structure-Finding Methods

Finding voids and other cosmic web substructures is not necessarily straightforward, because there is no precise definition for each of these substructures. For this reason, there exists a large range of different structure-finding methods that produce different results, depending on the specific definitions used (see The Aspen-Amsterdam void finder comparison project; Colberg et al., 2008, and Libeskind et al., 2018). In this section, we will outline a number of different structure-finding methods used to identify voids in simulations and observations.

Void-finding procedures can be roughly divided into the following broad categories: geometric/Hessian-based methods, topological methods and phase space methods.

Geometric/Hessian-based methods are defined as those that use changes in either the tidal, velocity or density field to identify substructures in the cosmic web. These changes are captured in a matrix or tensor involving the second derivative of the field in question (i.e. a Hessian matrix or tensor). The tidal force field quantifies the local gravitational potential in specific regions, and the eigenvalues of the associated Hessian reveal the expansion/contraction of material, thus providing a classification scheme for clusters, filaments, sheets and voids (see Hahn et al., 2007 and Forero-Romero et al., 2009 for more details). The velocity shear tensor encodes the velocity of particles moving within the cosmic web as it evolves under gravity (velocity shear field), relying on velocity to classify substructures (e.g. Hoffman et al., 2012; Libeskind et al., 2013b; Carlesi et al., 2016; Pahwa et al., 2016). The Hessian of the density field uses density gradients (specifically the concavity of the local density field) to identify and classify substructures (e.g. Aragón-Calvo et al., 2007; Bond, Strauss & Cen, 2010; Trowland, Lewis & Bland-Hawthorn, 2013; Cautun et al., 2014; Adermann et al., 2017, 2018).

Phase space methods rely on the fact that if the intrinsic velocity dispersion of particles in the primordial universe is small, then the evolving spatial mass distribution can be interpreted as a 3-dimensional sheet folding itself in a 6-dimensional phase space, known as a phase space sheet. This formalism can trace the streams of mass flow, and thus the emergence of non-linear structures as the cosmic web evolves, allowing a dynamical classification of the emerging structures. Examples of void-finding procedures that utilise phase space methods include the ORIGAMI formalism (Falck, Neyrinck & Szalay, 2012; Falck & Neyrinck, 2015) and the procedures used by Shandarin (2011) and Abel, Hahn & Kaehler (2012). In the case of ORIGAMI, no parameters (including smoothing parameters),

shape or density criteria are imposed on the identification of voids. Voids are simply regions where no phase-mixing has occurred.

Topological methods involve using the connectivity and topology of the density field to identify substructures. One popular void-finding procedure that falls in this category is the watershed transform, which is used in two popular void-finding algorithms: the Watershed Void Finder (Platen, van de Weygaert & Jones, 2007) and ZOBOV (ZOnes Bordering on Voidness; Neyrinck, 2008). The watershed transform is a technique normally used for segmenting images, but can also be used to segment the cosmic web into different morphological structures. The method works by first identifying local density minima in the density field (procedures for this vary), then filling up the basins in which those minima lie with water. When the water level reaches the edge of the basin, it erects a ridge onto the saddle points that define the edge. Those ridges then define the edges of the voids, and consist of filaments and sheets. The watershed transform allows the identification of voids with a minimal number of constraints, allowing it to preserve and trace the substructure of voids. It also naturally identifies void hierarchies (voids within voids). However, a density threshold is required to prevent segmentation boundaries with densities lower than a typical void from being defined as void walls. Although the Watershed Void Finder and ZOBOV do not impose shape criteria in defining voids, they do require the use of density criteria to avoid identifying a large number of spurious voids, where these thresholds are defined somewhat arbitrarily. Other void finders have somewhat more restrictive definitions of voids, such as defining them as spherical underdensities or as unions of specific shapes (e.g. Kauffmann & Melott, 1992; Müller et al., 2000; Hoyle & Vogeley, 2002; Colberg et al., 2005).

In the next sections, we describe the Hessian-based method we used to classify substructures in the cosmic web, using as few parameters as possible.

3.3 The Hessian Void Finder

To identify substructures in the cosmic web of our simulations, I developed a void-finding algorithm based on the Hessian of the density field. There are four types of substructures of interest: knots, filaments, sheets and voids.

The Hessian matrix can be used to identify these substructures based on the gradients in their density fields. The Hessian matrix, $H_{\alpha\beta}(\mathbf{x})$, at a point $\mathbf{x}$, consists of second order partial derivatives of the local density, $\rho(\mathbf{x})$, that encode these gradients in its eigenvalues and eigenvectors, and is given by

$$H_{\alpha\beta}(\mathbf{x}) = \frac{\partial^2 \rho(\mathbf{x})}{\partial x_\alpha \partial x_\beta}, \tag{3.1}$$

where α and β denote various combinations of the three axes x, y and z. As there are three axes, the Hessian is a three-dimensional matrix with three eigenvalues. The sign of each eigenvalue reveals the presence of either a local maximum or minimum in the density field, along the direction of the corresponding eigenvector. In this way, substructures

can be identified from the number of maxima they exhibit along orthogonal axes. For example, a knot would consist of density maxima along any three orthogonal directions, a filament would show density maxima along two (and usually a density minimum along one direction), a sheet would consist of a density maximum along one (and density minima long two directions), and a void would exhibit density minima along any three orthogonal axes. The classification scheme thus works as follows:

Knot/Cluster/Blob: $\lambda_i, \lambda_j, \lambda_k < 0$
Filament: $\lambda_i, \lambda_j < 0, \lambda_k > 0$
Sheet: $\lambda_i < 0, \lambda_j, \lambda_k > 0$
Void: $\lambda_i, \lambda_j, \lambda_k > 0$

The eigenvalues are sorted so that $\lambda_k > \lambda_j > \lambda_i$.

Our classification starts with calculating a smoothly-varying density field, $\rho(\mathbf{x})$, from the particle positions within the simulation. To do this, we first implement a kernel density estimator (from VELOCIraptor; Elahi, Thacker & Widrow, 2011; Elahi, 2013), which estimates the local density around each particle using the 64 nearest neighbour particles and a smoothing kernel. The simulation is divided into a regular grid with cell length $1\ h^{-1}$ Mpc, approximately equivalent to the interparticle spacing, and the local density for each particle is assigned to the nearest grid cell. If a grid cell has more than one particle assigned to it, then the densities are averaged. These gridded densities are then additionally smoothed with a Gaussian kernel of scale $3\ h^{-1}$ Mpc, equivalent to three grid cells in length, to identify smoothly-varying gradients at the appropriate scale for large-scale structure classification, and also to smooth out discontinuities in the gridded density field. A scale of $3\ h^{-1}$ Mpc was chosen so that the results of the classification procedure matched the results of a visual classification of substructures. The kernel density estimation is necessary to ensure that important local structures (such as void walls) are both smooth and well-defined before applying large-scale Gaussian smoothing, which does not sufficiently smooth the density field at the local level.

The Hessian matrix is calculated at the centre of all the grid cells, before being diagonalised to find its eigenvalues. Each grid cell is given a classification based on the sign of these eigenvalues, as illustrated in the classification scheme above. We chose to associate a zero gradient with lack of minima, to avoid identifying any completely flat region in the density field as a void, and hence all voids must have positive eigenvalues. The voids are identified by joining neighbouring cells (including edge and vertex neighbours) that have been classified as void-like, using a friends-of-friends algorithm. The void boundaries are identified as the set of sheet-like cells that neighbour at least one void-like cell. This scheme also allows single void-like cells within the grid to be identified as voids. However, these are ignored because they are too small to be properly resolved by our grid. Thus the smallest voids within our population are the ones consisting of two adjoining void-like cells, which are $2\ h^{-3}$ Mpc^3 in volume. A schematic of the density-based Hessian void-finding procedure is shown in Figure 3.2.

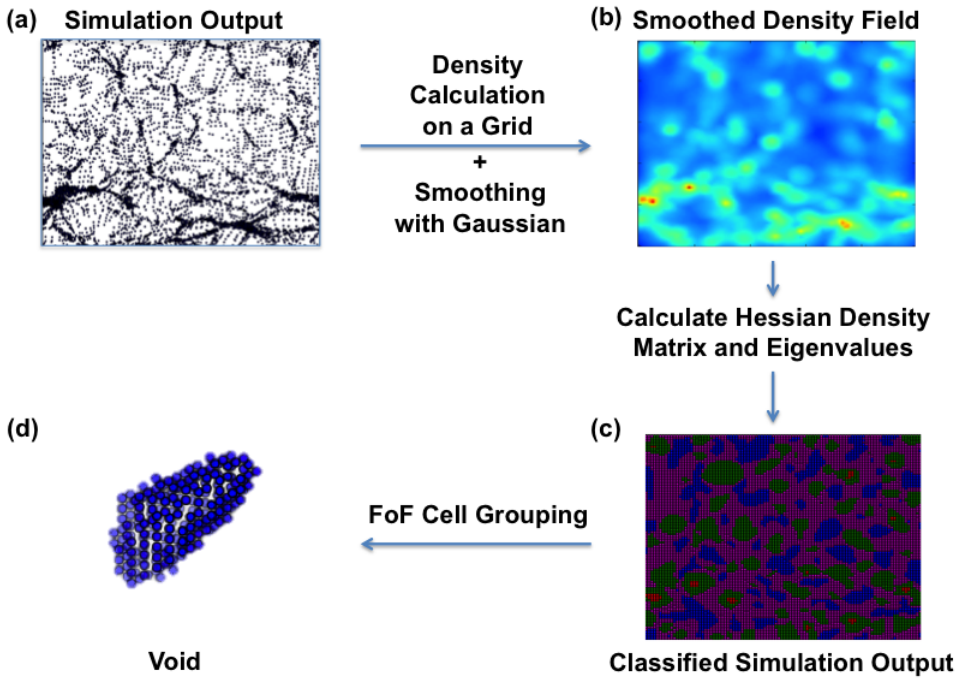

Figure 3.2: Schematic illustrating the void-finding process. (a) The raw simulation output showing the particle distribution in a $0.5\ h^{-1}$ Mpc slice of a $50\ h^{-1}$ Mpc simulation. (b) The density distribution after the kernel density estimation and Gaussian smoothing. (c) The classification given to each cell in the grid, where blue represents the void classification, purple represents the sheet classification, green represents the filament classification and red represents the knot classification. (d) An example of a void identified after linking together neighbouring void-like cells. For clarity, only the void boundary, defined by the nearest sheet cells, is shown.

Although we had the option of imposing an eigenvalue threshold (i.e. choose a non-zero threshold), we chose to use the natural definition of knots, filaments, sheets and voids as structures exhibiting density maxima or minima along different directions, which sets the threshold at zero. Our procedure also avoids imposing any shape on the voids. We instead define void boundaries where the density gradients no longer exhibit minima in all directions, thus allowing void shapes to be complex. We also do not impose a density criterion, instead generalising our definition of voids to minima in the density field, and allowing even shallow troughs to be identified as voids provided they are large enough. This is to make void-tracking through redshift easier, as voids begin their evolution as shallow troughs and only get deeper as the cosmic web evolves. Setting a density threshold could prevent these early voids from being identified.

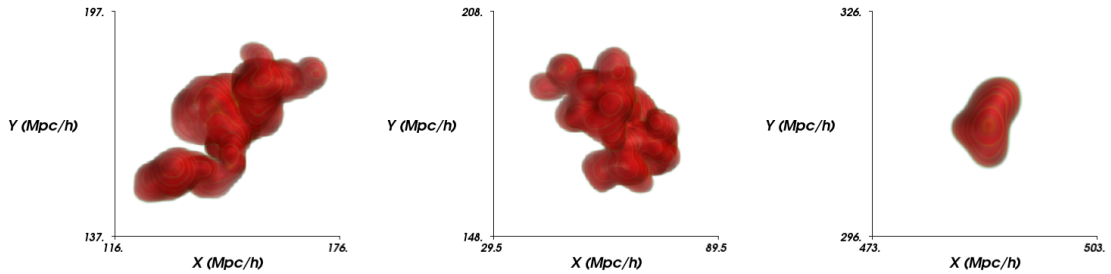

Figure 3.3: Examples of voids identified within the cosmic web of the ΛCDM simulation, at $z = 0$, revealing the highly irregular nature of many of the voids identified by our Hessian-based procedure, and the range of shapes they exhibit.

3.3.1 Results

In Figure 3.3, we show examples of voids of various sizes identified in the ΛCDM simulation at $z = 0$ by our void finder. Many of the voids we identify have complex shapes, and are far from spherical, as expected from anisotropic accumulation of material on to the cosmic web. We also find that the larger the voids, the more irregularity they can display, while smaller voids seem to exhibit far more regularity in their shapes. Although this difference could be explained by the resolution of our grid (since smaller voids are composed of fewer grid cells than larger voids, any irregularities in their shapes are not easily identified), it could also reflect the more complicated growth histories of larger voids (for example, involving void mergers).

One of the primary differences between our void populations and those identified from other methods is in the distribution of volumes. Our void population volumes range from 2 to $\sim 10,000\ h^{-3}$ Mpc^3, whereas the the voids found by VIDE, for example, in Sutter et al. (2015) and Pollina et al. (2016), cover volumes between roughly 500 and 3-4 $\times 10^5$ h^{-3} Mpc^3. The differences in maximum void size are due to differences in the way voids are identified between our method and VIDE. VIDE identifies hierarchies of voids that include smaller voids embedded within larger ones, where at least in Pollina et al. (2016), the smaller voids are cast out of the final sample. These larger voids at the top of the hierarchy are not identified as single voids by the Hessian matrix, because they contain local maxima. Instead, the smaller voids at the bottom of the void hierarchies with no local maxima are the only ones identified as voids, resulting in the discrepancy between the maximum void sizes in our void populations and those found using VIDE and other watershed transform methods. Although our method does not provide information on the hierarchies of voids and subvoids, it reliably keeps the void population clean of any local overdensities occurring within voids.

A related result is the fact that the total volume occupied by the voids in our population is approximately 11% of the total simulation volume, with 47% occupied by sheets, 38%

by filaments and 4% by knots. This is a smaller percentage than usually reported with other void finders. For example, Libeskind et al. (2018) reports that most void-finding methods find large void-filling fractions, coverin the approximate range of $40 - 70\%$, far greater than the fraction we obtain. The much greater void-filling fraction obtained by watershed transform methods might not be surprising, since they include in their void population the large voids at the top of the hierarchy. However, these large fractions are also obtained by the methods that most closely resemble our density gradient-based method, such as the tidal shear tensor method (Forero-Romero et al., 2009) and NEXUS+ (Cautun, van de Weygaert & Jones, 2013; Cautun et al., 2014). Another reason for the differences is that other void finders classify as voids what our void-finder classifies as sheets. This is because the eigenvalue thresholds are typically set to a small positive number (instead of 0) to match the visual impression of the cosmic web (e.g. Forero-Romero et al., 2009). It is worth noting that the fraction we find is very close to the fraction of 9.5% found by Trowland (2013) using the same void definition and method of identification, suggesting that the discrepancies in void-filling fraction are the result of differences in both void definition and void-finding method.

Despite the lack of density threshold in our void identification, we find that at $z = 0$, none of the voids in any of the simulations were denser than the average simulation density of $\log_{10}(\rho/\rho_{crit}) = -0.23$. Only 0.014% of voids in ΛCDM, 0.011% of voids in ϕCDM, and 0.012% of voids in CDE were denser than the commonly used threshold of 20% of the average simulation density. The density distribution (expressed as a probability density function) for ΛCDM at $z = 0$ is presented in Figure 3.4. The voids with higher average density than the simulation density could be depressions within high density regions, known as 'voids-in-clouds', which could constitute the initial stages of void formation. However, because of the low resolution in our simulation, the kernel density estimation (which uses nearest neighbours to calculate densities), and the large smoothing scale used, the depressions in the density field identified by our void-finder are very unlikely to reside within overdense regions. The voids denser than 20% of the average simulation density are likely to still be voids, that formed later in the simulation's evolution and are yet to reach these low densities. It is worth noting that the use of density thresholds in watershed transform-based methods such as VIDE are necessary to prevent large voids that contain significantly overdense subvoid walls from being classed as voids. Our method does not require such thresholds, as it is highly unlikely that it would class any object containing an overdensity as a void. Filamentary structures are unlikely to be thin enough (< 100 kpc wide) to be smoothed over by our Gaussian smoothing and classified as an underdensity, and knots are always connected to other structures through filaments.

Although there are differences between our void population and those produced by other void-finding methods, for our purposes we only require that the void-finding method be the same when analysing and comparing simulations and observational data.

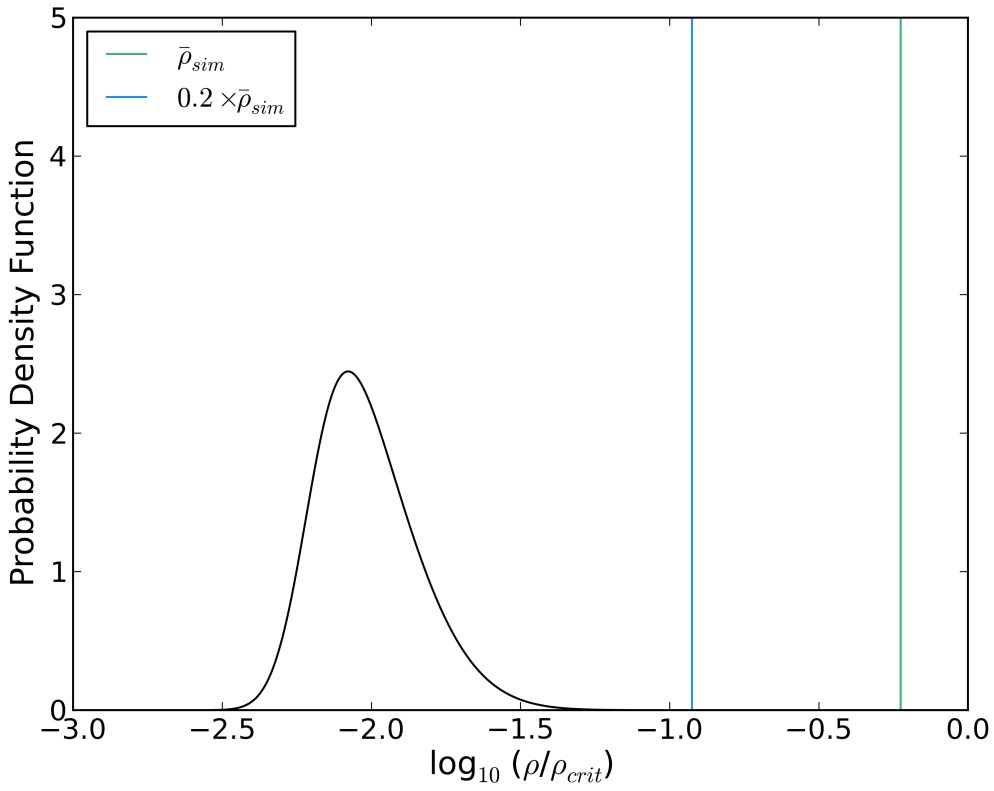

Figure 3.4: The probability density function representing the densities of the voids found in the ΛCDM simulation at $z = 0$, showing where the void population identified by our Hessian-based void-finder sits in relation to two different density thresholds. The vertical lines show the common density thresholds used in watershed transform void identification: green represents the average density of the simulation the voids were identified within, and blue represents 20% of this density. Almost the entire population of voids have densities below these thresholds.

CHAPTER 4

The Properties of Cosmic Voids in Evolving Dark Sector Cosmologies in the Low-Redshift Universe

This chapter presents the following published article:

Cosmic voids in evolving dark sector cosmologies: the low-redshift universe by **Adermann E.**, Elahi, P. J., Lewis G. F., Power, C., 2017, Monthly Notices of the Royal Astronomical Society, Volume 468, 3381–3394.

The paper details our study of the properties of cosmic voids in the dark matter distribution over the redshifts $z = 0 - 1$, in a pure quintessence model, a coupled dark energy model and the standard model. We chose to search for voids within dark matter because dark matter voids are more likely to preserve cosmological signatures than voids within baryonic matter. Unlike dark matter voids, these voids evolved under the influence of hydrodynamical forces, which could mask the imprints of cosmology in their properties. Additionally, since the total matter field is dominated by dark matter, the dark matter field offers a better insight than the baryonic matter field into the effect of cosmology on the total matter field.

Using N-body hydrodynamical simulations, we compared three primary void properties between the cosmological models: volume, shape and density. We found that the volume distribution at $z = 0$ in the coupled dark energy model contains a higher proportion of large voids than either the pure quintessence model or the standard model. Furthermore, we revealed that the average void density differs between the models. The pure quintessence model contains the emptiest voids and the standard model contains the densest, except at $z = 0$ when the average densities in the quintessence and the coupled model are extremely similar. These results suggest that the scalar field within the quintessence and coupled

models causes emptier voids to form, while the coupling causes voids to be denser. This is a significant result as it could form the basis for an observational probe of the cosmology governing our Universe.

The main figures demonstrating these results are Figures 4.5, 4.9 and 4.10. Figure 4.5 shows the distribution of ratios between the volume distributions predicted by each model, notably the statistically significant difference between the coupled model prediction and the standard model prediction at $z = 0$. Figure 4.9 shows the form of the average void density distribution in the three models and that the quintessence model contains the emptiest voids and the standard model the densest, and Figure 4.10 shows the distribution of ratios between the density distributions in each model, which demonstrate that the differences between the models are statistically significant.

Important Notes on the Published Paper:

In our density analysis, we reported the average density of voids instead of the more commonly used spherical density profiles, due to the high irregularity of many of our voids, and their elliptical nature. We also note that we measure the average void density distribution function in our study, and not the local density distribution function.

In Section 4.6.1, we followed Sutter et al. (2015) and suggested that the CDE model voids might have thinner (less dense) walls than the ΛCDM and ϕCDM voids, in order to explain the greater numbers of large voids at $z = 0$ in CDE than in the other two models. We suggested that the drag force present in CDE slows down the dark matter particles as they aggregate onto the higher density void walls, resulting in lower density walls. However, since our paper was published, we have revised our proposed explanation for this observation (although we acknowledge that detailed analysis of void walls in the simulations is necessary to confirm any proposed explanations). Our revised proposition is that the scalar field causes voids in the CDE and ϕCDM models to merge more quickly, producing greater numbers of large voids than in ΛCDM, and that the drag force in CDE slows down the merger rate. However, these effects are quite subtle, and most likely occur alongside other effects in the CDE model that show up at particular redshifts, as discussed in Chapter 5. To explain the greater numbers of large voids at $z = 0$ in the CDE model, we suggest that there is an additional contributing factor which increases the void evacuation rate and merger rate in CDE relative to ϕCDM (which may not involve the drag force at all), leading to the excess in large voids observed at $z = 0$ in this model. A more detailed explanation is provided in Chapter 5.

In our discussions about normalisation Sections 4.6.1 and 4.6.3, we focused primarily on the effect of choosing σ_8 at $z = 0$ to be the same in all cosmological models on our results. It is worth noting that we have also chosen other cosmological parameters to be the same at $z = 0$ (i.e. $\Omega_{\rm m}$, $\Omega_{\rm b}$ and h), and that varying this choice could also impact our results. The

effect of varying the redshift for the normalisation of all these cosmological parameters should also be investigated.

In Section 4.6.2, we stated that 'Our results also indicate that the common assumption of sphericity for voids is problematic.' To clarify, this statement refers to the common assumption of sphericity after stacking voids. We acknowledge that it is generally known that individual voids are not spherical, and that our results only suggest that the assumption of sphericity after stacking a large number of voids could present problems, due to their elliptical nature.

Contributions and Acknowledgements:

The analyses in this paper are all my own work, apart from the contributions detailed below:

The simulations were provided by Dr. Pascal Elahi and Prof. Chris Power.

The fitting code I wrote to find the best-fitting parameter values for the volume and density distributions was based on code originally written by Dr. Joseph Callingham.

The non-linear power spectra in Figure 4.1 was calculated using code written by Dr. Cullan Howlett and modified by Dr Pascal Elahi.

One of the codes used to produce Figure 4.2 was written by Prof. Geraint Lewis.

Section 4.3 was primarily written by Dr. Pascal Elahi and edited by me.

The text in this paper was checked and edited by Dr. Pascal Elahi and Prof. Geraint Lewis.

MNRAS **000**, 1–16 (2017) Preprint 20 August 2018 Compiled using MNRAS LATEX style file v3.0

Cosmic voids in evolving dark sector cosmologies: the low-redshift universe

Eromanga Adermann,[1]⋆ Pascal J. Elahi,[1,2] Geraint F. Lewis[1] and Chris Power[2]
[1]*Sydney Institute for Astronomy, School of Physics, A28, The University of Sydney, NSW, 2006, Australia*
[2]*International Centre for Radio Astronomy Research (ICRAR), The University of Western Australia, 35 Stirling Hwy, Crawley, Western Australia 6009, Australia*

Accepted 14 March 2017. Received 01 March 2017; in original form 22 November 2016

ABSTRACT
We present a comparison of void properties between the standard model of cosmology, Λ cold dark matter (ΛCDM) and two alternative cosmological models with evolving and interacting dark sectors: a quintessence model (ϕCDM) and a coupled dark matter–dark energy (CDE) model. Using N-body simulations of these models, we derive several measures of void statistics and properties, including distributions of void volume, ellipticity, prolateness and average density. We find that the volume distribution derived from the CDE simulation deviates from the volume distribution derived from the ΛCDM simulation in the present-day universe, suggesting that the presence of a coupled dark sector could be observable through this statistic. We also find that the distributions of void ellipticity and prolateness are practically indistinguishable among the three models over the redshift range $z = 0.0 - 1.0$, indicating that simple void shape statistics are insensitive to small changes in dark sector physics. Interestingly, we find that the distributions of average void density measured in each of the three simulations are distinct from each other. In particular, voids on average tend to be emptiest under a quintessence model, and densest under the ΛCDM model. Our results suggest that it is the scalar field present in both alternative models that causes emptier voids to form, while the coupling of the dark sector mitigates this effect by slowing down the evacuation of matter from voids.

Key words: dark energy – dark matter – cosmology: large-scale structure of the Universe

1 INTRODUCTION

Cosmic voids have recently gained popularity as cosmological probes (e.g. Sutter et al. 2014b; Cai et al. 2015; Pollina et al. 2016), primarily because these large, underdense regions of the universe are only mildly non-linear, experiencing little gravitational evolution compared to other, denser structures that make up the cosmic web. The statistics of these denser structures, namely sheets, filaments and knots (which house dark matter haloes), are frequently used as probes of cosmology, for example in the use of the halo mass function (Sutter & Ricker 2008) and the properties of galaxy cluster gas (Baldi et al. 2010; Carlesi et al. 2014b). The difficulty with this approach is that the properties and evolution of overdense regions are typically governed by more than just an underlying cosmology. Complex baryonic physics and coupling due to non-linear evolution also play a significant role in governing these structures, which at best complicates the process of distinguishing between baryonic physics and effects due to cosmology, and at worst may mask the cosmological signature we are searching for. In contrast, baryonic physics leaves a much smaller imprint on the growth of cosmic voids. For this reason, voids are seen as relatively pristine environments ideal for studying cosmology.

Voids have been used in a variety of cosmological studies, due to the low-density environment within them, which makes them particularly sensitive probes of cosmology. These include studies of the integrated Sachs–Wolfe effect (e.g. Granett et al. 2008; Cai et al. 2014; Granett et al. 2015) and weak gravitational lensing studies (e.g. Clampitt & Jain 2015). Voids have also been established as useful probes of dark energy (e.g. Bos et al. 2012; Pisani et al. 2015), modified gravity theories (e.g. Clampitt et al. 2013; Barreira et al. 2015; Cai et al. 2015; Lam et al. 2015; Zivick et al. 2015; Achitouv 2016) and alternative cosmological models (e.g. Massara et al. 2015; Sutter et al. 2015; Yang et al. 2015; Pollina et al. 2016), the last of which will be the focus of this paper.

⋆ E-mail: eromanga.adermann@sydney.edu.au (EA)

The Λ cold dark matter (ΛCDM) model of cosmology is the standard model for the universe. Within this cosmology, the universe is spatially flat, and dominated by an invisible dark sector composed of dark matter and dark energy. Dark matter plays a significant role in the clustering of baryonic matter and the formation of structure in the universe, while a cosmological constant Λ, or dark energy, drives the late-time accelerated expansion of the universe (Riess et al. 1998; Perlmutter et al. 1999).

The ΛCDM cosmology is well-supported by observational results. For example, the anisotropies in the cosmic microwave background (CMB; e.g. Bennett et al. 2013; Planck Collaboration et al. 2014b; Planck Collaboration et al. 2016b), features in the large-scale structure (e.g. Abazajian et al. 2009; Beutler et al. 2012), baryonic acoustic oscillations (Beutler et al. 2011; Blake et al. 2011; Anderson et al. 2014), weak lensing (e.g. Kilbinger et al. 2013; Heymans et al. 2013), cluster abundances (e.g.Vikhlinin et al. 2009; Rozo et al. 2010), galaxy clustering (e.g. Tegmark et al. 2004; Reid et al. 2010) and the luminosity–distance relation from Type Ia supernovae (e.g. Kowalski et al. 2008; Conley et al. 2011; Suzuki et al. 2012) are all consistent with ΛCDM.

Although ΛCDM offers a framework for dark matter and dark energy, it does very little to explain or predict their existence, properties and behaviour. Instead, we must rely heavily on observations to pinpoint the properties of the dark sector. Such observations have supported 'cold' dark matter (which has well-motivated candidates from theoretical particle physics; see Bertone et al. 2005; Petraki & Volkas 2013) over more energetic dark matter (such as hot dark matter that is relativistic at decoupling; e.g. Ma & Bertschinger 1994; Pogosyan & Starobinsky 1993). There is strong evidence for (a) non-baryonic elementary dark matter particle(s), though the exact properties of such (a) particle(s) are poorly constrained by observations. Dark energy appears to be well-characterised by a cosmological constant, Λ, driving the late time accelerated expansion and with a measured equation of state given by $w = \rho/p \approx -1$ (Suzuki et al. 2012; Chuang et al. 2016). However, its origin and nature are not well characterised. Without a more in-depth framework for the dark sector whose predictions match observations as well as the standard model, the nature of the dark sector remains an unsolved problem.

In spite of the excellent consistency between the predictions of ΛCDM and observations of the large-scale structure, the standard model does not appear to be in agreement with observations on galaxy scales. For example, ΛCDM predicts many more satellite galaxies than are observed for galaxies like the Milky Way (Klypin et al. 1999; Moore et al. 1999). While this may be the result of feedback processes removing gas from low-mass subhaloes and leaving almost completely dark subhaloes (e.g. Bullock et al. 2000; Benson et al. 2002; Nickerson et al. 2011, 2012; Hopkins et al. 2014; Sawala et al. 2016), the missing satellites may also indicate the need for more energetic dark matter candidates, or warm dark matter (e.g. Power 2013; Elahi et al. 2014). Another inconsistency is the unexplained alignment of satellite galaxies around the Milky Way (known as the vast polar structure; Pawlowski et al. 2012) and Andromeda (known as the Plane of Satellites; Ibata et al. 2013; Conn et al. 2013). Such alignments have also been seen beyond the Local Group (e.g. Yang et al. 2006; Li et al. 2013). Furthermore, the velocities of these satellite galaxies are significantly more correlated than ΛCDM predicts (e.g. Ibata et al. 2014; Gillet et al. 2015), though there is some evidence that these alignments are not too improbable in ΛCDM (Cautun et al. 2015; Sawala et al. 2016).

Within the ΛCDM framework, the densities of dark matter and dark energy evolve independently, as different functions of cosmic time. Dark matter dominated at early times, allowing structure to form, while dark energy dominates the current epoch, driving the accelerated expansion of the universe. However, in spite of their independence, the two densities coincidentally have similar values today. This is dubbed the coincidence problem, and its existence suggests that there may be some inter-dependence between dark matter and dark energy, which is currently absent from ΛCDM (e.g. Wetterich 1995; Amendola 2000). This has led to the proposal of alternative models, including models with modifications to general relativity (e.g. Hu & Sawicki 2007; Starobinsky 1980; see de Felice & Tsujikawa 2010 for a review), and models with dynamical scalar fields, or quintessence models (e.g. Ratra & Peebles 1988; Wetterich 1988; Armendariz-Picon et al. 2001; see Tsujikawa 2013 for a review).

In dynamical scalar field models, dark energy is assumed to couple to dark matter (regardless of whether the dark matter is cold or warm). Dark matter decaying into the scalar dark energy field results in the late-time accelerated expansion of the Universe. The coupled dark sector gives rise to dark matter particles that change with time, and the strength of gravitational interactions between dark matter particles differs from the corresponding strength of baryon-baryon and dark matter-baryon interactions. Former studies into structure formation in coupled versus uncoupled models have revealed significant differences in the growth functions, and thus the matter power spectrum, between the models (Li & Barrow 2011). Differences have also been found in the weak lensing signature of coupled models (Giocoli et al. 2015, Pace et al. 2015). Pollina et al. (2016) found that coupled dark energy models have a greater number of large voids in the CDM distribution than ΛCDM, which they suggest is the result of a higher normalisation of linear perturbations at low redshifts in the coupled models. Sutter et al. (2015) found similar differences in the number of very large voids between a strongly coupled model (ruled out by observations; Pettorino et al. 2012) and ΛCDM, and additionally found differences in the void density profiles between these cosmologies. However, Carlesi et al. (2014a,b) found no significant changes in the cosmic web and halo mass function in coupled models, although they did discover small differences in the concentration and spin parameter of small field haloes.

The goal of our study is to further probe the signatures of alternative cosmological models. We examine void properties in the low-redshift Universe, determine how they differ among cosmological models and propose explanations for the signatures found. Further investigations into void properties and their evolution in a high-redshift universe will be published in later papers. In Sections 2 and 3, we present the simulations of the standard and alternative cosmological models, as well as the methods we used to identify voids in the large-scale structure. Our main results are presented

in Section 4, followed by a discussion and explanation of the results in Section 5.

2 EVOLVING DARK SECTOR MODELS

We focus on two non-standard cosmological models, both of which feature dynamic dark sectors: an uncoupled quintessence model (ϕCDM) and a coupled dark energy-dark matter model, which will be referred to as Coupled Dark Energy (CDE) throughout this paper. Both these models differ from ΛCDM in that dark energy arises due to the evolution of a time-dependent scalar field, ϕ, rather than being characterised as a cosmological constant. Additionally, the scalar field may be coupled to dark matter, in general, evolving dark sector models. The general form of the Lagrangian for the scalar field of such models (including the two models of interest) is given by

$$L = \int \sqrt{-g}\left(-\frac{1}{2}\partial_\mu\partial^\mu\phi + V(\phi) + m(\phi)\psi_m\bar{\psi}_m\right)d^4x, \quad (1)$$

consisting of a kinetic term, a potential term $V(\phi)$, which, if chosen appropriately, gives rise to the late-time accelerated expansion, and a coupling term that describes the interaction between the scalar field and dark matter field (ψ_m). For our models, we choose a Ratra–Peebles potential (Ratra & Peebles 1988)

$$V(\phi) = V_0\phi^{-\alpha}, \quad (2)$$

where V_0 and α are constants, determined through fits to observational data, and ϕ is in Planck units.

2.1 Uncoupled Quintessence (ϕCDM)

The Lagrangian for the scalar field of the uncoupled quintessence model contains no coupling term ($m(\phi) = 0$), and hence there is no direct interaction between the scalar field ϕ and the dark matter field ψ_m. However, unlike ΛCDM, the dark energy density evolves with time as a result of the inclusion of the scalar field, which, in turn, alters the expansion history of the universe compared to ΛCDM.

2.2 Coupled Dark Energy (CDE)

The coupling mechanism between the scalar field and the dark matter field is enabled by choosing a non-zero form of $m(\phi)$, also known as the interaction term. For our CDE model, we choose

$$m(\phi) = m_0\exp[-\beta(\phi)\phi], \quad (3)$$

for the interaction term, a form that alleviates the coincidence problem. To simplify things, we choose a constant coupling term, $\beta(\phi) = \beta_0 = 0.05$. This coupling enables dark matter particles to decay into the scalar field. It also results in an additional frictional force experienced by dark matter particles (but not baryons), leading to a difference in the evolution of the amplitude of their density perturbations. This coupling has been found to significantly affect the fraction of baryons in cluster-sized haloes (Baldi et al. 2010). Our CDE model differs from ΛCDM in both the expansion history, due to the scalar field, and the evolution of the density perturbation amplitudes, due to the coupling.

3 SIMULATIONS

For our study, we produced simulations of the following three cosmologies: a reference ΛCDM, an uncoupled quintessence model and a coupled dark energy-dark matter model with a coupling parameter β_0. Following Elahi et al. (2015), we choose $(h, \Omega_m, \Omega_b, \sigma_8) = (0.67, 0.3175, 0.049, 0.83)$, ensuring all cosmologies have parameters consistent with $z = 0$ ΛCDM Planck data (Planck Collaboration et al. 2014a, 2016a). The coupling parameter, $\beta_0 = 0.05$, in our simulation is chosen to test the boundaries of allowed coupling (see Pettorino et al. 2012; Xia 2013) in order to maximise any observational differences that may exist between this cosmology and the standard ΛCDM model. The linear power spectrum and growth factor $f \equiv d\ln D(a)/d\ln a$ are calculated using first-order Newtonian perturbation equations and the publicly available Boltzmann code CMBEASY (Doran 2005). We note that although these simulations have neglected star formation and feedback physics, baryons do not appear to significantly change the void population. Large underdense regions remain underdense, regardless of whether the simulation includes dark matter only, or accounts for hydrodynamic or full baryonic physics (Paillas et al. 2017).

Initial conditions are generated by perturbing particles placed on a Cartesian grid with the first-order Zel'dovich approximation using a modified version of the publicly available N-GENIC code. The modified code uses the growth factors calculated by CMBEASY to correctly calculate the particle displacements in the non-standard cosmologies. All the simulations are started at $z = 100$ with the same phases in the density perturbations. Choosing the same initial phases results in underdense regions forming in the same locations in all simulations. Each underdense region in a given simulation has a corresponding underdense region in other simulations (perhaps with different properties such as density or size, depending on cosmology). This is the case despite potentially different exact profiles of density perturbations between cosmologies with different power spectra, such as ΛCDM and CDE.

We use DARK-GADGET, a modified version of the P-GADGET-2 N-body code (for more details, see Carlesi et al. 2014a). The key modifications are the inclusion of a separate gravity tree to account for the additional long-range forces arising from the scalar field, and an evolving dark matter N-body particle mass that models the decay of the dark matter density. The code requires the full evolution of the scalar field, ϕ, the mass of the dark matter N-body particle and the expansion history.

Our simulations are 500 h^{-1}Mpc boxes containing 2×512^3 particles (dark matter and gas) giving a mass resolution of $m_{\rm dm}(m_{\rm gas}) = 6.9(1.3) \times 10^{10}\ h^{-1}\mathrm{M}_\odot$[1]. Though the mass resolution is poor for identifying haloes, this resolution is more than enough to identify voids. All runs use a gravitational softening length of 1/33 of the interparticle spacing. The set of simulations run is summarised in Table 1. Fig. 1 shows the growth factor evolution, the evolution of the Hubble constant and the non-linear power spectrum in the three simulations.

[1] The exact masses in the coupled cosmology naturally depend on redshift, but this is the mass resolution at $z = 0$, as we fix Ω_m at this time.

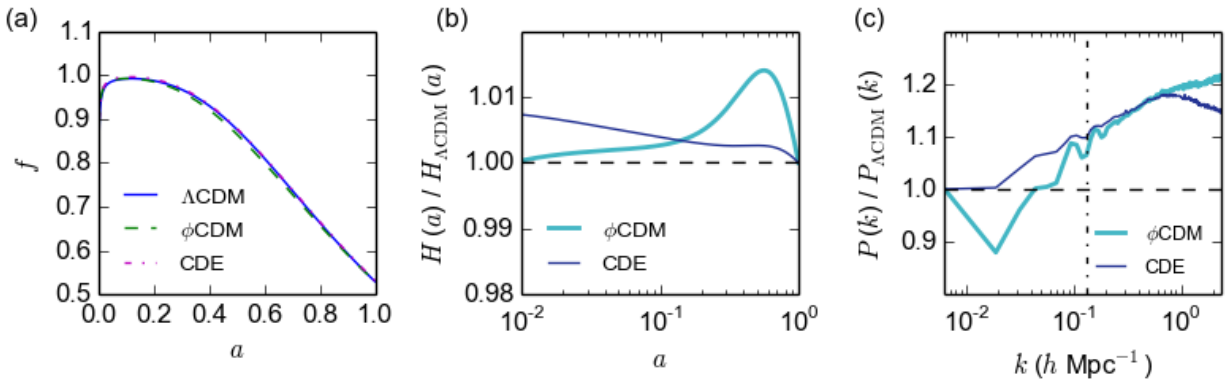

Figure 1. (a) The evolution of the growth factor, f, as a function of the scale factor, a, for the ΛCDM (solid blue), ϕCDM (dashed green) and CDE (dot–dashed magenta) simulations. (b) The ratio of the Hubble constant in the ϕCDM (thick teal) and CDE (thin blue) simulations, $H(a)$, to the Hubble constant in the ΛCDM simulation, $H_{\Lambda\mathrm{CDM}}(a)$, expressed as a function of the scale factor a. (c) The ratio of the non-linear power spectrum in the ϕCDM (thick teal) and CDE (thin blue) simulations, $P(k)$, to the power spectrum in the ΛCDM simulation, $P_{\Lambda\mathrm{CDM}}(k)$, expressed as a function of the wavenumber k. To the left-hand side of the vertical line is the region where the ratios have an error of less than 1 per cent.

Table 1. Simulations

Cosmology	Comments
ΛCDM	DM/gas run along with five pure DM runs ($m_{\mathrm{DM}} = 8.1 \times 10^{10}\ h^{-1}\mathrm{M}_{\odot}$), each with different random seeds to study cosmic variance.
ϕCDM	DM/gas run along with two pure DM runs, each with different random seeds to study cosmic variance.
CDE	DM/gas run only, with $\beta_0 = 0.05$.

4 VOID FINDING

Our study focuses on voids in the CDM particle distributions of our simulations. The method we used to define and identify these voids is based on the Hessian matrix of second derivatives at each point, a method that has also been used to identify other large-scale structures, such as sheets, filaments and knots (e.g. Aragón-Calvo et al. 2007; Hahn et al. 2007; Zhang et al. 2009; Trowland et al. 2013). The Hessian matrix is given by

$$H_{\alpha\beta}(\mathbf{x}) = \frac{\partial^2 \rho(\mathbf{x})}{\partial x_\alpha \partial x_\beta}, \tag{4}$$

which characterises the curvature of a density field, $\rho(\boldsymbol{x})$, as a function of position, $\boldsymbol{x}$. The eigenvalues of this matrix reveal whether the local density field around the point $\boldsymbol{x}$ is a local maximum or minimum, along three orthogonal directions (given by its eigenvectors). If all three eigenvalues are negative, the local density field is a local maximum, or is knot-like. If only two eigenvalues are negative, the density field has a local maximum along two orthogonal axes and a local minimum along the third axis, or is filament-like. If one eigenvalue is negative, then the density field has a local maximum along only one of its axes, or is sheet-like. Finally, if all three eigenvalues are positive, the density field exhibits a local minimum in all directions, or is void-like.

To find the void regions in the dark matter density field, we divided the simulation up into a regular grid of $500 \times 500 \times 500$ cells, so that each cell was 1 h^{-1} Mpc in length. The densities of particles were estimated using a smooth particle hydrodynamics kernel. These densities were then assigned to the nearest grid cell, so that an average density for each cell could be calculated. Finally, these density values were convolved with a Gaussian kernel, with a scale of 3 h^{-1} Mpc, to smooth out small-scale fluctuations. Both the cell length and smoothing scale were chosen to match the visual classification of structure based on particle positions only. We calculated the eigenvalues of the Hessian matrix for each cell, and gave each of them a classification using the scheme described above. We then utilised a friends-of-friends algorithm to group neighbouring void-like cells together, requiring that neighbouring cells be linked together only if both are void-like cells, or the second is a sheet-like cell. This results in a single layer of sheet-like cells surrounding and bounding each group of linked void-like cells, naturally defining a physical surface with a thickness of 1 h^{-1} Mpc for our voids. We also imposed the requirement that each void consists of at least two void-like cells linked together, with a corresponding volume of 2 h^{-3} Mpc^3. Smaller groups were excluded as voids, as they were not sufficiently resolved with our chosen cell size.

It is worth noting that our Hessian-based method of void finding is different from other void finding methods in that it does not assume any particular shape, nor apply any density criterion, when identifying voids. There have been numerous methods used to define and identify voids. Some are based on the velocity field (e.g. VWeb; Hoffman et al. 2012), but most methods use the density field. ZOnes Bordering On Voidness (ZOBOV, Neyrinck 2008) and The Void IDentification and Examination toolkit (VIDE, Sutter et al. 2014a) use a watershed algorithm to define voids and requires that voids satisfy a minimum density criterion. Other density-based algorithms demand that voids be spherical underdensities (e.g. Padilla et al. 2005). In contrast to these and several other commonly used methods, we do not enforce density thresholds when indentifying voids nor do we

require voids to have any particular shape. As we do not apply any density constraints, we can identify voids that would be ignored by ZOBOV/VIDE. More importantly, not constraining the shape of voids enables us to find voids that are irregular in shape. We show an example of such a void in Fig. 2, identified in the ΛCDM simulation at $z = 0.0$.

We find that the smallest voids (of a few h^{-3} Mpc^3 large) tend to be more regular (but not necessarily more spheroidal) in shape than larger voids. Since irregular shapes require more than a few cells to define, irregularity becomes more probable as voids get larger. The most likely explanation for this is void merging, with the largest voids forming as a result of the merger of multiple smaller and more regular voids. Fig. 2 shows an example of two voids found in the ΛCDM simulation using the method described above: one large, irregular void and one small, regular void.

5 RESULTS

The three cosmologies were found to contain a very similar number of voids at $z = 0.0$; a total of 35221 voids were found in the ΛCDM simulation, compared to 35701 voids in the ϕCDM simulation and 34646 voids in the CDE simulation. The similarity in numbers is not entirely surprising, since the initial conditions for each simulation contained the same initial density perturbation phases, and therefore the same initial underdensities. The differences in cosmology, which govern the initial amplitudes and the evolution of these underdensities, have resulted in a difference of only a few hundred voids.

In this section, we will discuss the differences in the volume distribution, shape distribution and average density distribution of voids occurring in the three simulations across the low redshift universe, spanning $z = 0.0$, 0.6 and 1.0. We will also discuss whether any of these differences could be used to observationally distinguish among the cosmologies, and hence differing dark sector physics.

5.1 Volume Distribution

A probability density function (PDF) to quantify the probability of finding a void of a specific volume was calculated for each simulation at multiple redshifts. We define the PDF so that the probability of finding a void of a given volume is the value of the PDF at that volume. We chose to use a PDF to quantify the void size distribution because it is independent of the total number of voids we found, and hence the size of the simulation box. The number of voids of a given volume within a region of space can be calculated by multiplying the PDF by the total number of voids we find (or expect to find) in that region of space, and reading off the value of the function at the given volume.

We defined the volume of a void to be the number of 1 h^{-3} Mpc^3 void-like cells that comprise it, excluding the sheet-like cells that make up the boundary layer. To find the appropriate PDF, we plotted the number of voids found at each integer volume. The shape of this distribution showed a power-law dependence on volume for small voids, before falling more drastically with volume for larger voids, indicating that the underlying PDF has the same dependence. We do not attempt to follow the full excursion set formalism (e.g. Sheth & van de Weygaert 2004), but instead appeal to it for the rough functional form of our PDF, given by

$$f(V) = \frac{1}{V_0\Gamma(1-\alpha)}(V/V_0)^{-\alpha}\exp(-V/V_0), \quad (5)$$

where V (h^{-3} Mpc^3) is the void volume, α is the power-law slope, V_0 is the characteristic volume that defines the position of the turnover and $\Gamma(1-\alpha)$ is simply the gamma function evaluated at $1-\alpha$:

$$\Gamma(1-\alpha) = \int_0^\infty x^{-\alpha}e^{-x}dx. \quad (6)$$

Using a Metropolis–Hastings based Markov chain Monte Carlo (MCMC) algorithm via the open source EMCEE package (Foreman-Mackey et al. 2013), we obtained the best-fitting values and their uncertainties for the parameters α and V_0. These values were obtained for the volume PDFs at $z = 0.0$, 0.6 and 1.0, for each of the three cosmological models, and are shown in Table 2. The corresponding distributions are shown in Fig. 4, while an example of a triangle plot obtained for the fit of the ΛCDM volume PDF at $z = 0.0$ is presented in Fig. 3.

In each of the redshift snapshots, the PDFs for the three cosmologies show remarkable similarity over the volume range. The 1σ uncertainties on their fit parameters reveal that the curves are consistent with each other over a large range of volumes. However, as Fig. 3 shows, these fits are partially correlated, meaning that the best-fitting values and uncertainties obtained may not reflect the true parameter distribution. To determine if the PDFs are truly indistinguishable from each other, we performed a bootstrapping analysis on the distribution of values that were sampled during the fitting process. This involved taking a subsample of parameter values from the values that were sampled during the fitting, determining the corresponding PDFs from these subsamples, then calculating the ratios between PDFs of different models, thus producing a distribution of PDF ratios for each pair of models. We used 5000 subsamples to produce the PDF ratio distributions for each pair of models, which our convergence analysis showed would sufficiently represent the full ratio distributions. These distributions are represented in Fig. 5, which shows both the medians and the ranges covered by the 16^{th}–84^{th} percentiles of the ratio distributions. The median ratios are shown by the solid lines, while the interquartile ranges are represented by the shaded regions. As the ratio distributions are not Gaussian, we avoid using the 1σ uncertainty, and instead use the 16^{th}–84^{th} percentile range (which covers the same percentile range as 1σ) to represent the uncertainty in the median ratios. The increase in the spread of this range that we see towards high volumes may be attributed to small number counts for large voids, which means the shape of the PDF in this region is less constrained.

The PDF ratios at $z = 0.6$ and 1.0 all tend to be consistent with a ratio of 1. The highest median ratio is ≈ 1.1 (between ϕCDM and ΛCDM), the lowest median ratio is ≈ 0.93 (between CDE and ϕCDM), and the corresponding interquartile ranges all safely overlap with a ratio of unity. The ratio distributions between the CDE and the ΛCDM PDFs are the most consistent with 1; hence, we would expect to see very little difference in void abundance across all volumes between these cosmological models. Though the

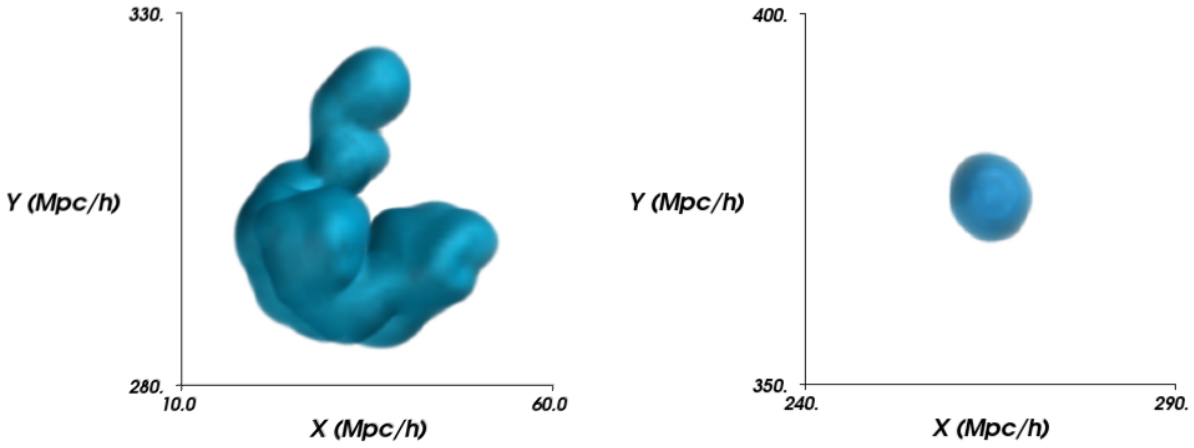

Figure 2. An example of a void of volume 1899 h^{-3} Mpc^3 (left-hand panel) and a void of volume 59 h^{-3} Mpc^3 (right-hand panel) found in the ΛCDM simulation at $z = 0.0$, using the Hessian-based method. Both voids are depicted using the 1 h^{-1} Mpc thick boundary sheet layer; hence, they appear slightly larger than their volumes (which are calculated using void-like cells only) suggest. For clarity, only the x- and y-axes are shown. The z-axis points out of the page.

medians do show a greater deviation from unity at higher volumes between ϕCDM and ΛCDM, suggesting that, on average, we should expect to see more voids with volumes of the order of $\sim 10^3$ h^{-3} Mpc^3 in a ϕCDM than in a ΛCDM cosmology at these redshifts; the differences are unlikely to be distinguishable, especially given the considerable overlap with a ratio of unity in these distributions. The void abundance PDFs at these redshifts are therefore unlikely to be useful as probes of cosmology.

However, there is a large range of volumes at $z = 0.0$ where the CDE PDF deviates from the other two PDFs. The deviation from ΛCDM and ϕCDM starts at $V \approx 700$ and ≈ 880 h^{-3} Mpc^3, respectively, and increases with volume. More than half of the ratios in the CDE:ΛCDM and the CDE:ϕCDM ratio distributions are greater than 1. At volumes greater than $V \approx 7 \times 10^3$ h^{-3} Mpc^3, more than half the ratios are greater than 1.1. Additionally, we can reasonably expect to see at least 10% more voids with volumes of $\approx 4 \times 10^3$ h^{-3} Mpc^3 in a CDE universe than a ΛCDM or a ϕCDM universe, and this excess increases with volume. On the other hand, the distribution of ratios between the ϕCDM and ΛCDM PDFs clearly shows that the void abundance in these cosmologies would be practically indistinguishable.

Finally, the PDFs all evolve slowly with redshift. We note that V_0 increases with redshift for all cosmologies (with a significance of many σ), corresponding to an increase in the volume at which the turnover occurs. This is not entirely surprising, as we expect smaller voids to expand or merge to form larger voids, which would push the turnover out to larger volumes. The power-law index, α, also slightly increases with redshift, which corresponds to a slight increase in the steepness of the power law. However, as both parameters are correlated (Fig. 3), the change we observe in α may simply reflect the change in V_0 from $z = 1.0$ to 0.0. The similarity in power-law slope across redshifts is consistent with excursion set-based void abundance predictions that do not show a large power-law dependence on redshift (Jennings et al. 2013).

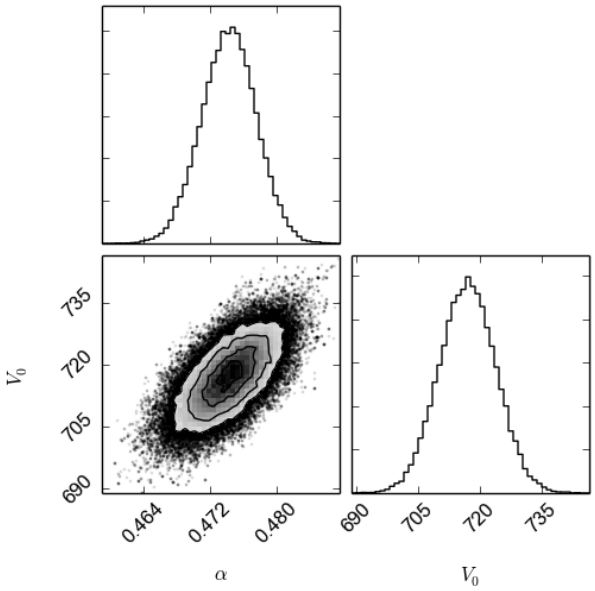

Figure 3. Triangle plot showing the sampled parameter distribution for the ΛCDM volume PDF at $z = 0.0$.

5.2 Shapes

Voids are often assumed to be roughly spherical, for example, during the void-finding process (as in Padilla et al. 2005), and in the construction of density profiles as a function of radius from the void centre (Hamaus et al. 2014). However, our simulations suggest that voids can be quite irregular in shape (see e.g. Fig. 2), and are better ap-

Table 2. The best-fitting values (including 1σ errors) for the volume PDF parameters, α and V_0. The values for three redshifts are shown for each cosmology.

Cosmology	Parameters	$z = 0.0$	$z = 0.6$	$z = 1.0$
ΛCDM	α	0.474 ± 0.003	0.442 ± 0.003	0.423 ± 0.003
	V_0	$717.1^{+6.8}_{-6.9}$	$598.3^{+5.4}_{-5.3}$	$540.0^{+4.7}_{-4.7}$
ϕCDM	α	0.476 ± 0.003	0.445 ± 0.003	0.427 ± 0.003
	V_0	$716.2^{+6.9}_{-6.9}$	$602.8^{+5.5}_{-5.4}$	$543.2^{+4.8}_{-4.7}$
CDE	α	0.477 ± 0.003	0.441 ± 0.003	0.424 ± 0.003
	V_0	$731.7^{+7.1}_{-7.1}$	$599.0^{+5.5}_{-5.3}$	$540.6^{+4.7}_{-4.6}$

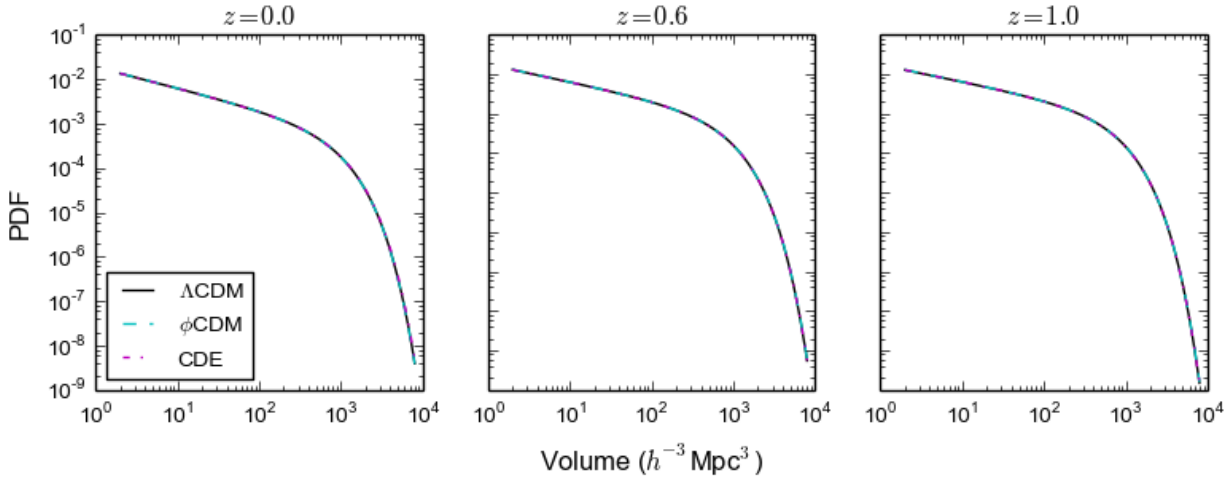

Figure 4. The void volume PDFs at multiple redshifts for the ΛCDM (black solid), the ϕCDM (cyan dashed) and the CDE (magenta dot–dashed) simulations.

proximated by ellipsoids than spheroids, especially for the smaller, unmerged voids. We define the ellipticity of a void (or deviation from a perfect sphere), e, to be

$$e = \frac{1}{4}\frac{c^2 - a^2}{a^2 + b^2 + c^2}, \tag{7}$$

where a, b and c are the three axes that define the ellipsoid, with c being the longest and a being the shortest. This definition is identical to the definition given by Nadathur (2016), except that we express e in terms of the three ellipsoid axes, rather than eigenvalues of the inertia tensor. With this definition, a perfect sphere has an ellipticity of zero. The greater the value of e, the greater the deviation from a perfect sphere.

Ellipsoids can be either prolate (more elongated along one axis) or oblate (more elongated along two axes). To quantify this variation in shape, we define the prolateness, p, to be

$$p = \frac{1}{4}\frac{(b^2 - a^2) + (b^2 - c^2)}{a^2 + b^2 + c^2}. \tag{8}$$

Again, this definition is identical to that given by Nadathur (2016). A negative value of p indicates elongation along one axis relative to the other two (prolate), whereas a positive value of p indicates relative elongation along two axes compared to the third axis (oblate). A prolateness of zero indicates that the ratio between the shortest axes and the longest axes is comparable, meaning that the shape is neither prolate nor oblate.

We calculated the ellipticities and prolateness of the voids in each of the three simulations, by calculating the eigenvalues of the moment tensor for each void, given by

$$M_{ab} = \sum_i (x_i^a - X^a)(x_i^b - X^b), \tag{9}$$

where i denotes the sheet-like cells that comprise the boundary layer of the void, x_i^a and x_i^b denote the a-coordinate and b-coordinate of the ith boundary layer cell, respectively, and X^a and X^b are the a-coordinate and b-coordinate of the barycentre of the void, respectively, with both a and b representing the x-, y- and z-axes. The eigenvalues of this tensor (e_1, e_2, e_3) correspond to a third of the square of the axes of the ellipsoid that best approximates the shape of the void:

$$e_1 = \frac{a^2}{3}, \quad e_2 = \frac{b^2}{3}, \quad e_3 = \frac{c^2}{3}. \tag{10}$$

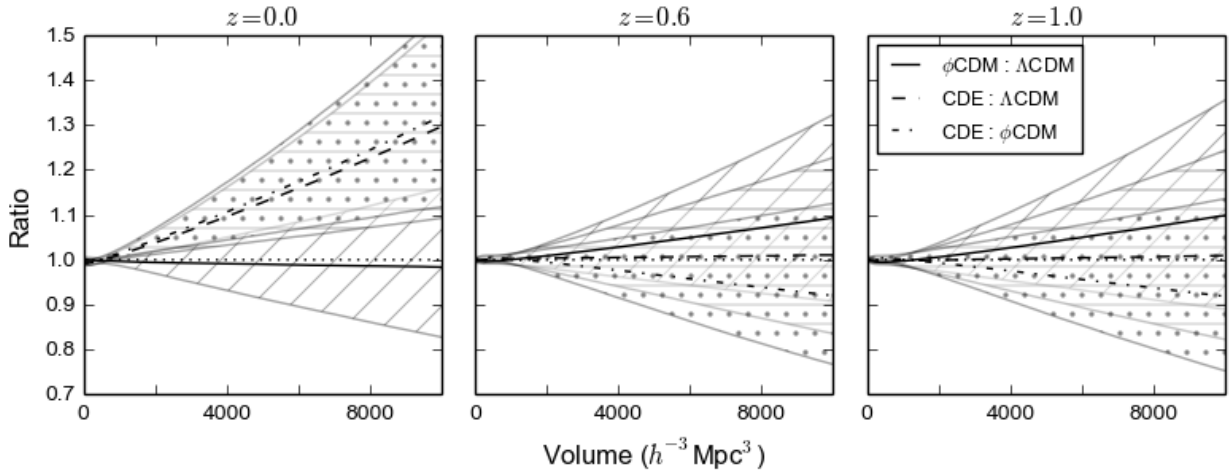

Figure 5. The median ratios of the volume PDFs: ϕCDM/ΛCDM (solid line), CDE/ΛCDM (dashed line) and CDE/ϕCDM (dot–dashed line). The shaded regions show the range covered by the 16^{th}–84^{th} percentiles of the ratio distributions, with the ϕCDM/ΛCDM region indicated by diagonal lines, the CDE/ΛCDM region indicated by horizontal lines and the CDE/ϕCDM region indicated by dots. The black dotted horizontal line indicates a ratio of 1.

From these eigenvalues, we calculated the length of the ellipsoid axes, and thus the ellipiticities and the prolateness of each void. We note that we included only voids of size greater than or equal to 10 cells (equivalent to 10 h^{-3} Mpc^3 in volume) in this analysis, since voids smaller than this do not have resolved shapes. Fig. 6 shows the resulting distributions of prolateness versus ellipticity, for the voids in ΛCDM, ϕCDM and CDE at z = 0.0, 0.6 and 1.0. The distributions are all peaked at (e, p) = (0.10, –0.05), with 25^{th} and 75^{th} percentiles occurring at (e, p) = (0.08, –0.09) and (e, p) = (0.13, –0.02), respectively, consistent with the results derived in Nadathur (2016) for voids in the SDSS-III BOSS Data Release 11 (Alam et al. 2015). There is no significant difference among the cosmologies in the distribution of ellipticities or prolateness, with the most common void shape across all three cosmologies being slightly prolate.

As mentioned in Section 4, the largest voids can be very irregular due to their formation through the merger of smaller voids. Interestingly, the irregularity of large voids does not automatically translate to a noticeable deviation from an approximate spheroid, which is clear from the distribution of void size versus ellipticity in Fig. 7. In fact, the smaller voids tend to exhibit a greater spread in ellipticity than the larger voids. This result is consistent with previous studies into the spherical evolution of voids, which found that the largest voids are better approximated by a spherical model than the smallest voids (e.g. Achitouv et al. 2015; Demchenko et al. 2016). A likely reason for this is that there are many more ways to merge smaller voids to form a lower ellipticity void than a high-ellipticity void, and hence a greater number of approximately spheroidal large voids form than approximately ellipsoidal large voids.

5.3 Densities

For each simulation and at multiple redshifts, we calculated a PDF to quantify the probability of finding a void of a specific average density. The average density for each void was calculated by taking the average of the smoothed densities of each cell in a void (excluding the boundary layer of sheet-like cells), which we calculated during the cell classification process. We found that the best fitting function for the underlying PDF governing the distribution of average void densities was a skewed Gaussian distribution, defined as a function of the base 10 logarithm of the void density, given by

$$p(t) = \frac{1}{\sqrt{2\pi}} e^{-t^2/2} \left[1 + \text{erf}\left(\frac{\alpha t}{\sqrt{2}}\right)\right], \tag{11}$$

where α is the skewness parameter and $t \equiv (x - \mu)/\sigma$, with μ and σ, respectively, denoting the mean and the standard deviation of the corresponding Gaussian. Again, we used a Metropolis–Hastings based MCMC-fitting algorithm to obtain the best-fitting values for these parameters, which are summarised in Table 3. The triangle plot obtained for the fit of the ΛCDM density PDF at z = 0.0 is presented in Fig. 8. Fig. 9 shows the shapes of the PDFs with these parameter values, highlighting the differences in the average void density distribution among the three cosmological simulations at z = 0.0, 0.6 and 1.0. The spherical threshold, which denotes the maximum density defined for voids predicted by excursion set theory, is given by $\Delta_v = -0.8$ for ΛCDM, or equivalently $\log_{10}(\rho/\rho_{\text{crit}}) = -1.27$ in the units chosen for Fig. 9. It is clear from the figures that the vast majority of our voids in all three simulations have average densities below this threshold.

To show the differences among the simulations more rigorously, we once again subsampled the parameter distributions from the fitting process, and used the subsamples to calculate corresponding distributions of PDF ratios. As before, our convergence analysis showed that 5000 subsamples sufficiently represent the full ratio distributions. Fig. 10 shows the median of these PDF ratios, along with the 16^{th} and 84^{th} percentiles, for z = 0.0, 0.6 and 1.0.

It is clear from Figs 9 and 10 that the PDFs are almost

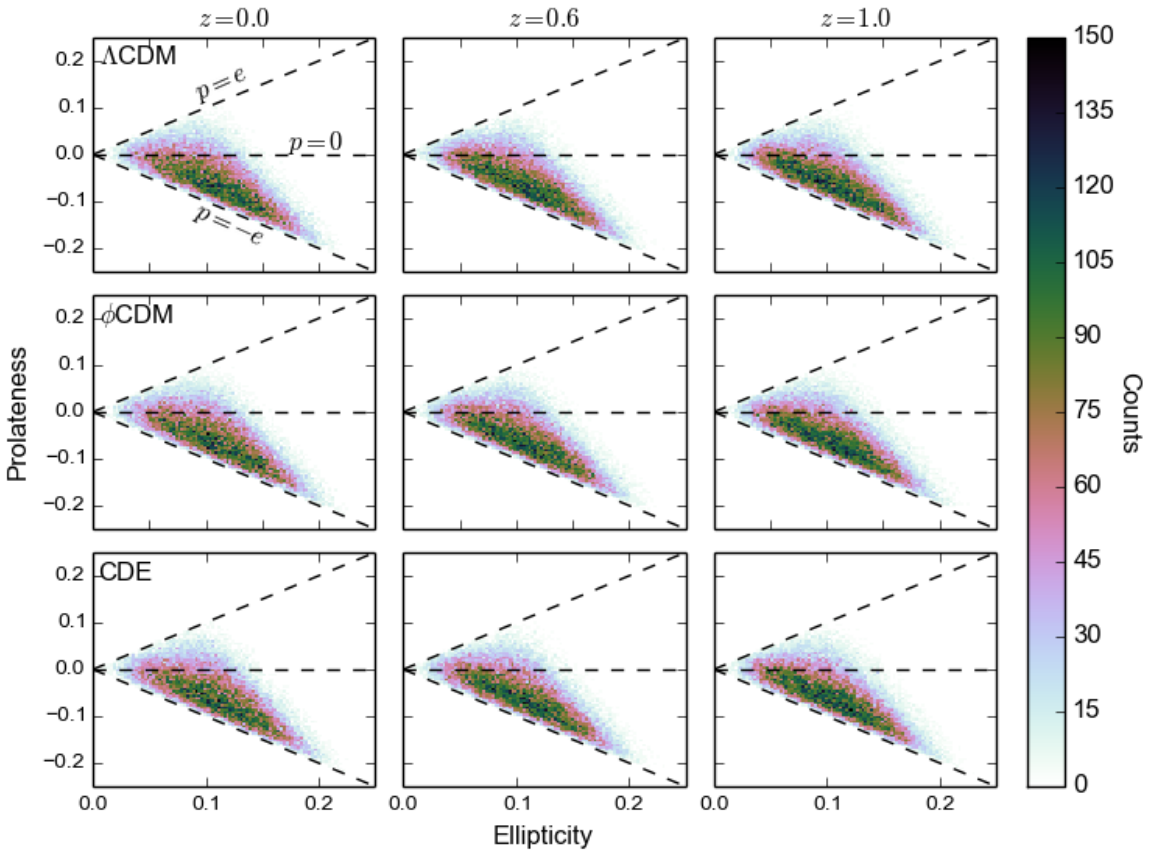

Figure 6. Distribution of void ellipticity versus prolateness in ΛCDM (top row), ϕCDM (middle row) and CDE (bottom row), for z = 0.0, 0.6 and 1.0. The horizontal black dashed line represents a prolateness of zero. The $p = e$ line represents the limiting case where the two shortest sides are equal in length (i.e. $a = b$), while the $p = -e$ line denotes the limiting case where the two longest sides are equal in length (i.e. $b = c$).

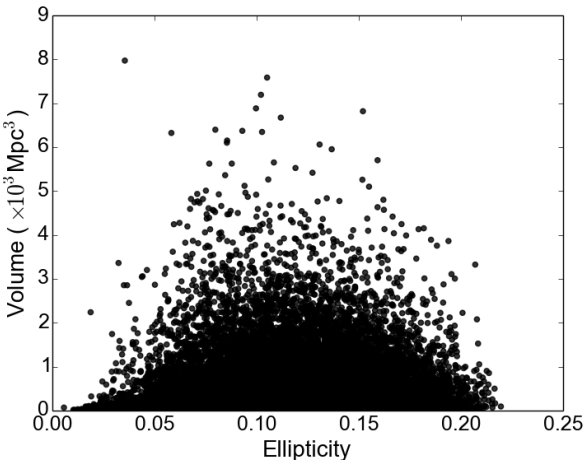

Figure 7. Relationship between void size and ellipticity for ΛCDM at z = 0. The distribution shows that the smallest voids tend to have a larger spread of ellipticities than the larger voids.

all distinct from one another for all three redshifts. At z = 0.6 and 1.0, the ΛCDM PDF has the highest density peak, while the ϕCDM PDF has the lowest. This indicates that on average, the voids in both ϕCDM and CDE cosmologies are slightly emptier than the voids in a ΛCDM cosmology. This is also seen at z = 0.0, where the ϕCDM and CDE PDFs appear to have converged, while ΛCDM remains distinct. The PDF peaks (characterised by μ) also shift towards lower densities as the simulations evolve from z = 1.0 to 0.0, while their spread (given by σ) and skewness towards the lower density region (given by α) generally increases. This suggests that voids, on average, become emptier with time, as expected, since matter continuously evacuates out of voids as it accumulates on to higher density structures. The deviations from a ratio of 1 at low densities is due to the ratios of small numbers, since the corresponding PDF values drop off to zero at slightly different rates. The exact shape of drop-off is unlikely to be well-characterised though, due to small number statistics in this region. For this reason, the deviations at the lowest densities are unlikely to be useful in distinguishing among cosmological models.

Table 3. The best-fitting values (including 1σ errors) for the skewed Gaussian parameters, μ, σ and α. The values for three redshifts are shown for each cosmology.

Cosmology	Parameters	$z = 0.0$	$z = 0.6$	$z = 1.0$
ΛCDM	μ	-2.208 ± 0.001	-2.071 ± 0.001	-1.991 ± 0.001
	σ	0.260 ± 0.001	0.226 ± 0.001	0.205 ± 0.001
	α	$2.600^{+0.044}_{-0.001}$	$2.415^{+0.039}_{-0.001}$	$2.256^{+0.036}_{-0.001}$
ϕCDM	μ	-2.251 ± 0.001	-2.113 ± 0.001	-2.033 ± 0.001
	σ	0.272 ± 0.001	0.237 ± 0.001	0.217 ± 0.001
	α	$2.715^{+0.046}_{-0.001}$	$2.493^{+0.041}_{-0.001}$	$2.368^{+0.037}_{-0.001}$
CDE	μ	-2.246 ± 0.001	-2.092 ± 0.001	-2.010 ± 0.001
	σ	0.270 ± 0.001	0.232 ± 0.001	0.210 ± 0.001
	α	$2.700^{+0.047}_{-0.001}$	$2.474^{+0.041}_{-0.001}$	$2.295^{+0.036}_{-0.001}$

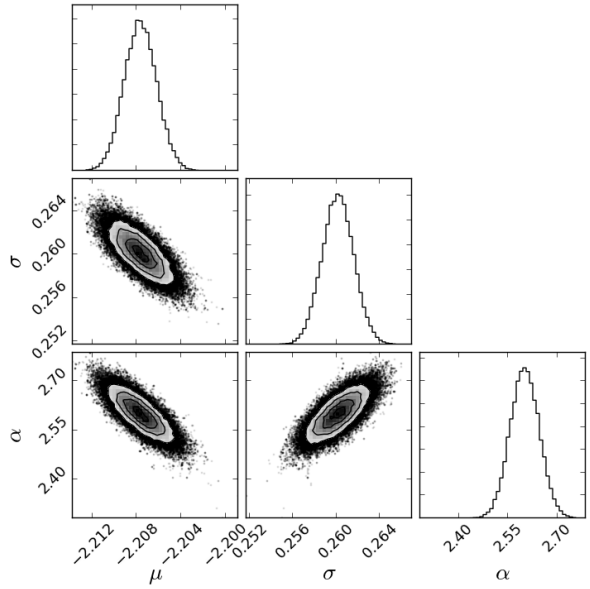

Figure 8. Triangle plot showing the sampled parameter distribution for the ΛCDM density PDF at $z = 0.0$.

6 DISCUSSION

Our simulations show that changes in expansion history and the presence of coupling in the dark sector alter the void size distribution at $z = 0.0$, as well as the average density of voids across $z = 0.0 - -1.0$. However, these differences in dark sector physics do not alter the void ellipticity or prolateness distribution at any redshift, nor do they affect the void size distribution at $z = 0.6 - -1.0$. Given that our simulations differ from each other primarily in the effects of the underlying cosmology, the differences we see among void properties are significant and can be confidently attributed to differences in the underlying model (and hence dark sector physics). We may view these differences as imprints or signatures of dark sector physics on the cosmic web, and use them to observationally constrain the properties of the dark sector. The most promising signature we have found is the potential for the average void density distributions to distinguish between the standard cosmological model and the evolving dark sector models.

6.1 Volume Distribution

The median ratio between ϕCDM and ΛCDM is much more consistent with unity at $z = 0.0$ than at the higher redshifts, potentially signalling greater discrepancies with increasing redshift. At $z = 0.6 - 1.0$, the ratio reaches ≈ 1.05 at volumes of around $\approx 5 \times 10^3\ h^{-3}$ Mpc^3, and continues to rise with volume. Though these ratios only show a small deviation from unity at low redshifts, they hint at the existence of greater discrepancies between ϕCDM and ΛCDM at redshifts greater than $z = 1.0$. However, to determine whether this is the case, the same analysis must be conducted on simulation snapshots at a range of redshifts greater than $z = 1.0$, which will be covered in a follow-up study (Adermann et al., in preparation).

The lack of significant differences between the void volume distributions of ϕCDM and ΛCDM suggests that for our particular form of ϕCDM, the scalar field does not leave a strong imprint on the abundance of voids in the universe at late times. The specific form of ϕCDM we chose exhibits only small changes in the expansion history compared to ΛCDM, with the greatest deviation corresponding to a Hubble parameter approximately 1.02 times greater than in the ΛCDM model, occurring at late times (see Fig. 1). This deviation may have been too small to affect the volume distribution significantly, or the change may have occurred too late in the formation of each void for their sizes to be significantly influenced. This is especially important to consider if final void sizes are most heavily influenced by conditions early in the process of void formation. For our ϕCDM model, the final void sizes appear to be dominated by the initial density perturbations and gravity, and only minimally influenced by

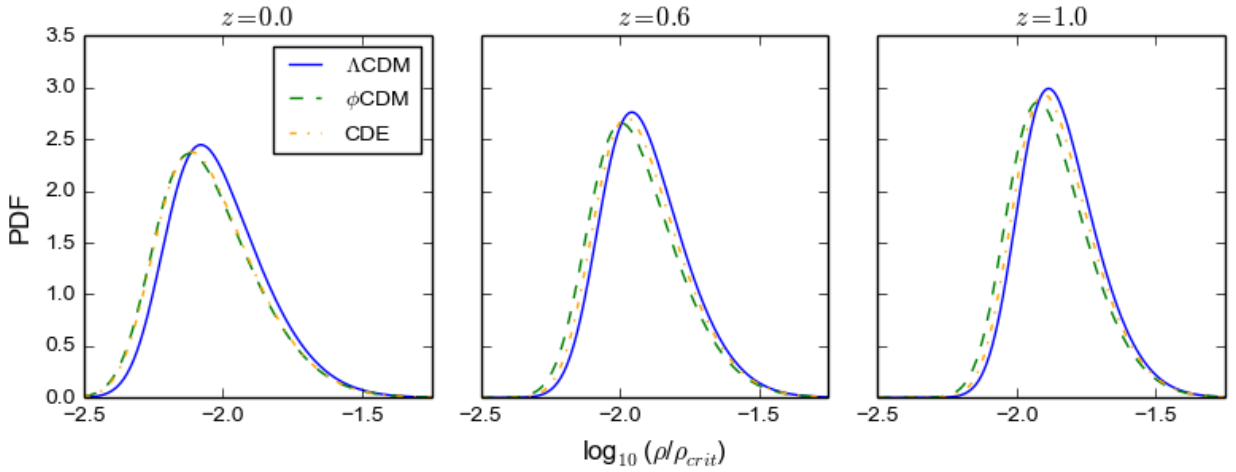

Figure 9. Probability distribution functions for the base 10 logarithm of the average void density in the ΛCDM (solid blue), ϕCDM (dashed green) and CDE (orange dot–dashed) cosmological simulations at $z = 0.0$, 0.6 and 1.0, in units of the critical density. The ΛCDM spherical threshold corresponds to a vertical line at $\log_{10}(\rho/\rho_{\rm crit}) = -1.27$.

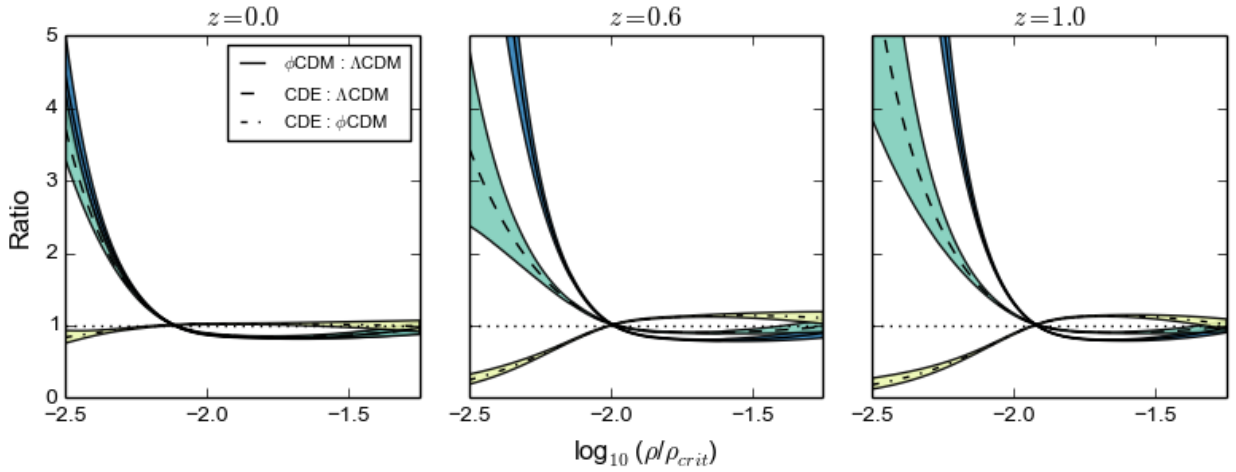

Figure 10. The median ratios of the density PDFs: ϕCDM/ΛCDM (solid line), CDE/ΛCDM (dashed line) and CDE/ϕCDM (dot–dashed line). The shaded regions show the range covered by the $16^{\rm th}$–$84^{\rm th}$ percentiles of the ratio distributions, with ϕCDM/ΛCDM in dark blue (or dark grey in black-and-white print), CDE/ΛCDM in green (or medium grey) and CDE/ϕCDM in yellow (or light grey). A ratio of unity is shown by the black dotted horizontal line.

expansion history, or, equivalently, the scalar field. As there are multiple realisations of a ϕCDM universe, these results do not rule out more visible signatures on void abundance under ϕCDM models with different forms of the potential $V(\phi)$.

Our results also show that the CDE model leaves an imprint on the void size distribution at $z = 0.0$, while ϕCDM is indistinguishable from ΛCDM at the same redshift. Therefore, it is the coupling between the scalar field and dark matter that affects most the abundance of voids in the universe today, rather than the presence of the scalar field in place of a cosmological constant. For our specific models, the coupling results in an increase in the abundance of voids with $V \sim 10^3\ h^{-3}$ Mpc^3. Interestingly, the effect of the coupling is apparent only at $z = 0.0$. At higher redshifts, its effect is much less noticeable.

These results are partially consistent with the results obtained by Sutter et al. (2015), who found an increased number of large voids in their coupled dark sector model compared to ΛCDM, at $z = 0$. However, the excess they show in void abundance occurs at larger volumes than indicated by our results. While our results show a greater void abundance for voids of the order of $\sim 10^3\ h^{-3}$ Mpc^3, their results show a consistency in the abundance of voids of this size between ΛCDM and CDE, with the excess starting at effective radii of $> 25 - -30\ h^{-1}$ Mpc, corresponding to volumes of $\sim 10^4\ h^{-3}$ Mpc^3. It is worth noting that the coupled model used in this study is governed by the same Lagrangian

as ours, apart from the use of a greater coupling constant (cDE with $\beta = 0.099$; for model specifics, see Sutter et al. 2015).

Sutter et al. (2015) suggest that the reason for the excess is the thinning of void walls when moving from the standard to the coupled dark sector models. Smaller voids in the ΛCDM cosmology may then be identified as a single larger, merged void in the coupled dark sector cosmology. In our early analyses of the differences in voids between our ΛCDM and ϕCDM models (at $z = 0.0$) in 50 h^{-1} Mpc and 2×128^3 particle simulations, we discovered that some of the largest voids in the ϕCDM model correspond to two or three smaller voids in the ΛCDM model that had been merged in the ϕCDM model, consistent with Sutter et al.'s (2015) suggestion. This suggests that thinning of void walls may be linked to the scalar field, which is present in both the ϕCDM and CDE models, in addition to its coupling to dark matter.

However, this effect is not significant in our current results, when we applied the same analyses to the larger 500 h^{-1} Mpc and 2×1024^3 particle simulations. Despite the evidence for wall thinning and merging in the smaller simulations, the larger ϕCDM simulation does not predict a significant excess in large voids compared to ΛCDM at $z = 0.0$, which suggests that though it may occur, wall thinning may not be drastic enough to cause most neighbouring voids to merge. On the other hand, the relative excess in larger voids between CDE and ΛCDM is consistent with more significant wall thinning occurring between voids, as found by Sutter et al. (2015). This suggests that the coupling to dark matter by the scalar field has a much more noticeable effect on wall thinning than the scalar field on its own. This might be expected as the additional effective drag acting between baryonic matter and dark matter due to the coupling would potentially slow down the evacuating matter, leaving less material to accumulate on to the void walls.

Despite the similarities in cosmological models used by Sutter et al. (2015), there is an interesting difference between their results and ours, namely the volume range at which CDE produces an excess of voids relative to ΛCDM. We find the excess to be statistically significant but not especially large (up to ≈ 1.3 times as many as ΛCDM), whereas Sutter et al. (2015) find several times as many voids in their CDE model than in their ΛCDM model. There are a number of reasons for this. First, Sutter et al. (2015) use a stronger coupling strength ($\beta = 0.099$ compared to our value of $\beta = 0.05$). It seems likely that the excess (both amplitude and range) depends on the coupling, though we cannot say for certain without a larger parameter space studied. Increasing coupling leads to an increased drag force, which, in turn, results in thinner void walls. Thinner walls increase void merger rates and artificial merging of voids by void finders, thereby creating a greater discrepancy between CDE and ΛCDM. Without detailed tracking of void evolution, as was done in Sutter et al. (2014b), this explanation remains untested. In future studies, we will follow the methodology of Sutter et al. (2014b) and produce void merger trees akin to halo merger trees.

There are also a few potential reasons for the differences between their results and ours that do not imply a physical origin: the simulation volumes differ (theirs was eighth the volume of ours, with higher mass resolution), and they used a watershed-based algorithm (VIDE) to identify voids in their simulations (biases in void-finding techniques remain to be thoroughly catalogued). Although differences in mass resolution result in differences in the density field, at large scales, the low-density regions that correspond to voids are generally well converged and independent of resolution. Small scales, and hence small voids, are more affected by resolution, but they are unlikely to be a major cause of the differences because we are neglecting the smallest, unresolved voids from our analyses. Differences could also arise due to the use of other criteria in their void finding that we did not impose, such as a density and size criterion, as well as the use of different smoothing scales to calculate densities. However, these should not alter the void-finding results significantly because imposing other criteria should only affect a small population of the densest and smallest voids, while using different smoothing scales will affect only voids that are in the process of merging. Thus, we believe that the physical origin, namely the coupling strengths, remains the most reasonable explanation and primary reason for the difference.

Our results are generally consistent with the results obtained by Pollina et al. (2016), who also found an excess of large cosmic voids in their coupled dark sector model compared to ΛCDM, over the redshift range $z = 0.00 - -1.00$ (for more details on their coupled model, see Pollina et al. 2016). As with our results, this excess increases with void size. However, the excess was found to steadily increase with decreasing redshift, whereas our results show a more sudden increase at $z = 0.0$. Furthermore, the distributions they derive do not decrease with increasing size, but rather peak at effective radii of roughly $20--30\ h^{-1}$ Mpc. The range of void sizes they find includes voids with effective radii up to $\approx 40\ h^{-1}$ Mpc in size, while the largest voids in our simulations were only $\approx 10^4\ h^{-3}$ Mpc^3.

The use of different CDE models may account for the discrepancies we observe; Pollina et al. (2016) apply an exponential form for the potential governing the scalar field ($V(\phi) = A\exp(-\alpha\phi)$), as well as a much greater coupling strength ($\beta = 0.15$). Greater coupling, in addition to a different expansion history, may lead to a stronger signature at higher redshifts than $z = 0.0$, accounting for the differences in when the signature starts showing up. The inconsistency in void sizes is likely to be the result of using different void-finding methods. Pollina et al. (2016) use the same void finder as Sutter et al. (2015), who also find voids with much larger sizes than we find. The watershed-based algorithm appears to identify much larger voids than our density-based method. In addition, Pollina et al. (2016) apply additional cuts based on density contrast, which we do not apply. It is possible that many of their smallest voids were eliminated in this way, which was not the case in either Sutter et al.'s (2015) void catalogue or ours.

The normalisation of the amplitudes of the density perturbations used in their simulations also differs from ours (and that of Sutter et al. 2015). While the density perturbations in the models we use are normalised to have the same σ_8 at $z = 0.0$, those used in Pollina et al. (2016) are normalised to have the same amplitude of perturbations at $z = z_{\rm CMB}$, and, consequently, the amplitudes in their models differ most at $z = 0$ (for an in-depth discussion on normalisation method, see Elahi et al. 2015). As we expect the amplitudes of density perturbations to affect the growth of

voids, it is reasonable to expect that some of the deviations between CDE and ΛCDM seen in Pollina et al. (2016), including the fact that the deviation increases with decreasing redshift, could be due to the way the simulations were normalised. The best way to test this would be to derive the void volume distribution from models that have been normalised differently.

6.2 Shapes

The remarkable similarity in the e versus p distributions across simulations indicates that changes in expansion history and dark matter physics do not drastically alter the shape of the initial underdensities, which are the same across all simulations. This result suggests that the overall shape of voids is barely affected by small changes to expansion history due to a scalar field or additional drag terms due to coupling within the dark sector but rather dominated by the effect of gravity and the initial phases of the density perturbations. However, we note that higher order shape statistics may carry more noticeable imprints, which are not captured in our shape statistics.

Our results also indicate that the common assumption of sphericity for voids is problematic. In each of the shape distributions, there is a spread of ≈ 0.2 in the range of ellipticity and prolateness values, with a peak in the distributions at $e \approx 0.10$ and $p \approx -0.05$. This demonstrates that voids, when approximated by a regular ellipsoid, match an ellipsoid shape more commonly than a spheroid shape ($e = 0$, $p = 0$). Though the general deviation from a spheroid is not huge, the commonly used spheroid assumption for stacked voids still results in a loss of information, which may have implications for experiments involving the Sachs–Wolfe effect or the Alcock–Paczynski test. In particular, the spheroid assumption would be problematic if the overall ellipsoid shapes are not randomly oriented along different lines of sight, such that the deviations average out. We suggest that a more accurate method of stacking should assume that voids are ellipsoidal rather than spheroidal, drawn from a distribution in e and p.

The ellipsoid average has implications for defining and analysing void profiles. Void profiles are conventionally determined using an effective void radius, which implicitly assumes that the void can be approximated by a sphere. If most voids are ellipsoidal, then it may be more informative to define effective ellipsoid axes in which to calculate void density profiles, rather than use an effective radius where density variation information is invariably lost. However, it should be noted that a void density profile will still be a somewhat crude measure of how density varies within highly irregular voids (which many of our voids are), even if the profiles are calculated with respect to effective ellipsoid axes. Profiles for such voids would ideally take the shape of the void into account.

6.3 Densities

Out of the three void properties we have explored thus far, the average void density distribution shows the most potential for use as a probe of cosmology. Except for the similarity between ϕCDM and CDE at $z = 0.0$, these distributions are all distinct from one another across redshifts $z = 0.0 - 1.0$. In particular, at all three redshifts, ΛCDM produces denser voids than the other cosmologies.

A possible cause of the distinct difference in average void densities is the way dark energy is characterised in both ϕCDM and CDE compared to ΛCDM. In both the alternative models, the accelerated expansion of the universe arises due to the presence of a scalar field, whereas in the standard model, the cause is attributed to the presence of dark energy that produces an outwards pressure on the universe. The inclusion of an additional scalar field affects the expansion history of the universe, which, in turn, may affect the speed at which matter evacuates out of voids. Under the Ratra–Peebles potential used in our quintessence and coupled models, matter appears to evacuate out of voids more quickly.

The differences present in the average void densities can also be understood in terms of the non-linear power spectra in Fig. 1. Both ϕCDM and CDE have more power at scales where the vast majority of our voids are found ($0.1 \lesssim k \lesssim 1$) than ΛCDM. This is consistent with denser void walls and thus emptier voids, found in both the alternative models compared to the standard model.

The ϕCDM and CDE PDFs are distinct from each other at $z = 0.6$ and 1.0, indicating that the presence of coupling does affect the speed of evacuation at some time during void evolution. Specifically, as the peak of the CDE PDF occurs at a higher density than the peak of the ϕCDM PDF at $z = 0.6$ and 1.0, the presence of coupling between the scalar field and dark matter appears to cause voids to evacuate more slowly and contain more matter. This is consistent with the additional drag force between particles, which may be expected to slow down the evacuation of matter from voids. However, despite the additional drag force, the CDE PDF still peaks at a lower density than the ΛCDM PDF, indicating that voids in a CDE cosmology are still on average emptier than the voids in a ΛCDM cosmology. One possible explanation for this is that the effect of the scalar field (which is also present in our CDE model) in emptying out voids is greater than the effect of coupling in slowing down void evacuation. The lower density peak is offset by the effect of coupling, but not enough to produce voids as dense as those in ΛCDM, on average.

Interestingly, the difference in the distributions reduces to insignificance at $z = 0.0$, as the two PDFs converge. There are two possible explanations for this. The first is that the effect of coupling naturally reduces with time, perhaps as the evacuation speed in the CDE cosmology speeds up as fewer particles are left in voids, causing the average void densities in these two models to converge, and ultimately leaving no evidence of coupling on the average emptiness of voids in the present-day universe. If true, this would be a remarkable coincidence. The second explanation is that the evolution of the void densities is influenced by the normalisation of the density field perturbation amplitudes (our simulations are all normalised so that the mass variance, σ_8, at $z = 0.0$, is the same for all of them). Indeed, this would not be surprising, given that the normalisation affects the evolution of the initial density field perturbations (i.e. if we chose a different redshift for the normalisation, then the evolution of those amplitudes would look different). If this effect is as significant as the effect of coupling between dark matter

and the scalar field, then it is possible that the differences we see between the ϕCDM and CDE PDFs (and between the ΛCDM and CDE PDFs) across all three of these redshifts are affected by this normalisation. Determining the significance of the time of normalisation would require extracting the average void density PDFs from simulations normalised at different epochs, and checking for differences in the evolution of the PDFs.

Fortunately, the differences between the ΛCDM PDF and the ϕCDM PDF are unlikely to be affected by our normalisation, since the presence of the scalar field alters only the expansion history, and not the evolution of the initial density perturbations. We can therefore conclude that the scalar field, or the nature of dark energy, imprints itself on to the average density of voids. In our specific models, it produces emptier voids in the universe.

It is worth noting that the specific differences we see in the density PDFs may be very model-dependent. For example, using a different potential for the Lagrangians underpinning the ϕCDM and the CDE models may result in different PDF profiles, compared to ΛCDM. Furthermore, the choice of parameter values such as coupling strength may affect the size of the differences between the PDFs. For this reason, it is possible for certain realisations of alternative models to produce density PDFs that are very similar to that of the standard ΛCDM. Conversely, any difference found between the predicted ΛCDM PDF and the PDF derived from actual observations will not necessarily inform us of the specific cosmology of the universe. In order for strong constraints on the cosmology to be made, more studies into the particular dependence of the void densities on the specific model and its parameter values must be done.

Once we have predictions from a wide range of models, the advantage of using the average void density PDF as a probe of cosmology is clear. Unlike the volume distributions, the differences between models in the average void density distributions occur across the redshift range $z = 0 - 1$, which corresponds to a significantly larger observational volume in which to search for signatures of cosmology.

7 CONCLUSIONS

We studied the properties of voids in three different cosmological models: the standard ΛCDM model, a quintessence model with a time-varying scalar field and a CDE model featuring coupling between a time-varying scalar field and dark matter. We have made comparisons of void properties between these models in the redshift range $z = 0.0 - 1.0$, with the goal of identifying the signatures left on voids by the underlying dark sector physics within these models.

We ran numerical N-body simulations of each of the three cosmological models in boxes of length 500 h^{-1} Mpc, consisting of 512^3 dark matter and baryonic particles each. Each simulation was initialised to have the same density perturbation phases, enabling voids between simulations/models to be matched and compared. The primary difference between the simulations lay in the governing cosmological model, which allowed direct comparisons of various void properties to be made among the models and any differences found to be attributed to differences in underlying cosmology. Using a Hessian-based void-finding algorithm without applying shape or density requirements, we were able to find a variety of voids in the CDM distributions of these simulations, many of which are highly irregular and would not have been found via other methods. We conducted analyses on the sizes, shapes and average densities of these voids. For each of the three cosmological models, we derived a PDF describing the void size distribution, a void ellipticity and prolateness distribution, and a probability density function describing the average void density distribution.

We found that the CDE model is distinct from both ΛCDM and ϕCDM in the distribution of void sizes at $z = 0.0$. The void volume PDF predicted by the CDE model deviates from the standard model (and the ϕCDM) prediction by $\sim 10\%$ for large voids, a deviation that increases with void size. This deviation is not nearly as significant at the higher redshifts, nor is it seen between the ϕCDM and ΛCDM distributions across the three redshifts. This suggests that it is the coupling between the scalar field and dark matter that leaves a potentially observable imprint in the void abundance, particularly of large voids and at very late times, while the presence of the scalar field leaves only a minimal imprint. We propose that this signature may be attributed to the coupling, which introduces an additional drag force between baryons and dark matter, and causes thinning of void walls as matter evacuates more slowly from voids, enabling a greater number of larger voids to form through the merger of smaller voids (building on the original suggestion by Sutter et al. 2015).

Additionally, we found that the distributions of void ellipticity and prolateness were extremely similar across all three models in the redshift range $z = 0.0 - 1.0$. Our cosmological models leave no imprint on general void shape statistics, though it is possible that higher order shape statistics carry significant imprints. This indicates that the general void shape is dominated by gravity and the initial phases of the density perturbations, and is insensitive to small changes in dark sector physics. General void shape statistics are therefore unlikely to be useful probes of cosmology, and more complex shape statistics that quantify irregularity may be necessary. Furthermore, we found that the distributions of ellipticity and prolateness, calculated through the fitting of ellipsoids to the true void shape, suggest that the most common ellipsoid that best fits the shape of each void has an ellipticity of ≈ 0.10 and a prolateness of ≈ -0.05. Our results show that most voids are not, in fact, best represented by spheroids, but rather, they are best represented by slightly prolate ellipsoids. Furthermore, we find that the voids identified by our Hessian-based method can be very irregular in shape. Irregularity is most common amongst large voids, as they are likely to have become so through the merger of smaller voids. These results have important implications for common practices where the spherical void assumption is made (e.g. experiments involving void stacking, defining density profiles for voids). The inherent flaw in the assumption may significantly affect the results obtained through such practices.

The differences in the distribution of average void densities among the cosmologies may be the most promising signature of the underlying cosmology found in this study. With the exception of a great similarity between the average density PDFs in the ϕCDM and CDE models at $z = 0.0$, all of the models predict distinctly different distributions for

average void density, across all three redshifts. These results may be attributed to both the presence of the scalar field and its coupling to dark matter. CDE is seen to produce denser voids than ϕCDM, which suggests that the coupling alone affects the rate of matter evacuation from the void. This may be attributed to the additional drag term experienced by baryons and dark matter, which would slow the movement of material out of the void. The fact that ΛCDM still produces the densest voids, on average, despite the effect of coupling in CDE suggests that the effect of the scalar field in emptying voids is great enough to offset the effect of coupling. It is possible that the normalisation used in our simulations affected the position of the peaks derived from the ϕCDM and CDE simulations, and contributed to the strong similarity between those PDFs at $z = 0.0$. Further studies involving the use of different normalisations need to be conducted to shed light on to this result.

It is worth noting that the results presented in this study are true for specific realisations of quintessence and CDE cosmologies. It is not enough to simply determine that alternative cosmological models give rise to different void properties. As we have seen, different void properties may arise depending on the specific parameter values. Properly probing the nature of the dark sector requires quantifying how the strength of the coupling, or the specific changes in expansion history, affects the properties of voids. How strong must the coupling be to produce a deviation from the prediction of the standard model? Is there a dependence of the size of the deviation on the coupling strength? How different from ΛCDM predictions must the Hubble parameter be for any imprint to be observable? What form must the potential, $V(\phi)$, take in order to leave an imprint? These questions are especially important for constraining the vast range of possible models that are consistent with our universe.

ACKNOWLEDGEMENTS

EA acknowledges financial support by the Australian Government and The University of Sydney, through an Australian Postgraduate Award and a University of Sydney Merit Scholarship, respectively. PJE acknowledges funding from the SSimPL programme and the Sydney Institute for Astronomy (SIfA), DP130100117 and DP140100198. The authors acknowledge the use of code written by Cullan Howlett to calculate non-linear power spectra, and the use of code written by Simeon Bird to read DARK-GADGET simulation snapshots. The authors also acknowledge the University of Sydney HPC service at The University of Sydney for providing HPC resources, in particular, the Artemis supercomputer, which have contributed to the research results reported within this paper. URL: `http://sydney.edu.au/research_support/`. This research made use of the NCI National Facility in Canberra, Australia, which is supported by the Australian Commonwealth Government, with resources provided by Intersect Australia Ltd and the Partnership Allocation Scheme of the Pawsey Supercomputing Centre.

REFERENCES

Abazajian K. N., et al., 2009, ApJS, 182, 543
Achitouv I., 2016, Phys. Rev. D, 94, 103524
Achitouv I., Neyrinck M., Paranjape A., 2015, MNRAS, 451, 3964
Alam S., et al., 2015, ApJS, 219, 12
Amendola L., 2000, Phys. Rev. D, 62, 043511
Anderson L., et al., 2014, MNRAS, 441, 24
Aragón-Calvo M. A., van de Weygaert R., Jones B. J. T., van der Hulst J. M., 2007, ApJ, 655, L5
Armendariz-Picon C., Mukhanov V., Steinhardt P. J., 2001, Phys. Rev. D, 63, 103510
Baldi M., Pettorino V., Robbers G., Springel V., 2010, MNRAS, 403, 1684
Barreira A., Cautun M., Li B., Baugh C. M., Pascoli S., 2015, J. Cosmology Astropart. Phys., 8, 028
Bennett C. L., et al., 2013, ApJS, 208, 20
Benson A. J., Frenk C. S., Lacey C. G., Baugh C. M., Cole S., 2002, MNRAS, 333, 177
Bertone G., Hooper D., Silk J., 2005, Phys. Rep., 405, 279
Beutler F., et al., 2011, MNRAS, 416, 3017
Beutler F., et al., 2012, MNRAS, 423, 3430
Blake C., et al., 2011, MNRAS, 418, 1707
Bos E. G. P., van de Weygaert R., Dolag K., Pettorino V., 2012, MNRAS, 426, 440
Bullock J. S., Kravtsov A. V., Weinberg D. H., 2000, ApJ, 539, 517
Cai Y.-C., Neyrinck M. C., Szapudi I., Cole S., Frenk C. S., 2014, ApJ, 786, 110
Cai Y.-C., Padilla N., Li B., 2015, MNRAS, 451, 1036
Carlesi E., Knebe A., Lewis G. F., Wales S., Yepes G., 2014a, MNRAS, 439, 2943
Carlesi E., Knebe A., Lewis G. F., Yepes G., 2014b, MNRAS, 439, 2958
Cautun M., Bose S., Frenk C. S., Guo Q., Han J., Hellwing W. A., Sawala T., Wang W., 2015, MNRAS, 452, 3838
Chuang C.-H., et al., 2016, MNRAS, 461, 3781
Clampitt J., Jain B., 2015, MNRAS, 454, 3357
Clampitt J., Cai Y.-C., Li B., 2013, MNRAS, 431, 749
Conley A., et al., 2011, ApJS, 192, 1
Conn A. R., et al., 2013, ApJ, 766, 120
Demchenko V., Cai Y.-C., Heymans C., Peacock J. A., 2016, MNRAS, 463, 512
Doran M., 2005, J. Cosmology Astropart. Phys., 10, 011
Elahi P. J., Mahdi H. S., Power C., Lewis G. F., 2014, MNRAS, 444, 2333
Elahi P. J., Lewis G. F., Power C., Carlesi E., Knebe A., 2015, MNRAS, 452, 1341
Foreman-Mackey D., Hogg D. W., Lang D., Goodman J., 2013, PASP, 125, 306
Gillet N., Ocvirk P., Aubert D., Knebe A., Libeskind N., Yepes G., Gottlöber S., Hoffman Y., 2015, ApJ, 800, 34
Giocoli C., Metcalf R. B., Baldi M., Meneghetti M., Moscardini L., Petkova M., 2015, MNRAS, 452, 2757
Granett B. R., Neyrinck M. C., Szapudi I., 2008, ApJ, 683, L99
Granett B. R., Kovács A., Hawken A. J., 2015, MNRAS, 454, 2804
Hahn O., Porciani C., Carollo C. M., Dekel A., 2007, MNRAS, 375, 489
Hamaus N., Sutter P. M., Wandelt B. D., 2014, Physical Review Letters, 112, 251302
Heymans C., et al., 2013, MNRAS, 432, 2433
Hoffman Y., Metuki O., Yepes G., Gottlöber S., Forero-Romero J. E., Libeskind N. I., Knebe A., 2012, MNRAS, 425, 2049
Hopkins P. F., Kereš D., Oñorbe J., Faucher-Giguère C.-A., Quataert E., Murray N., Bullock J. S., 2014, MNRAS, 445, 581
Hu W., Sawicki I., 2007, Phys. Rev. D, 76, 064004
Ibata R. A., et al., 2013, Nature, 493, 62
Ibata N. G., Ibata R. A., Famaey B., Lewis G. F., 2014, Nature, 511, 563

Jennings E., Li Y., Hu W., 2013, MNRAS, 434, 2167
Kilbinger M., et al., 2013, MNRAS, 430, 2200
Klypin A., Kravtsov A. V., Valenzuela O., Prada F., 1999, ApJ, 522, 82
Kowalski M., et al., 2008, ApJ, 686, 749
Lam T. Y., Clampitt J., Cai Y.-C., Li B., 2015, MNRAS, 450, 3319
Li B., Barrow J. D., 2011, Phys. Rev. D, 83, 024007
Li Z., Wang Y., Yang X., Chen X., Xie L., Wang X., 2013, ApJ, 768, 20
Ma C.-P., Bertschinger E., 1994, ApJ, 434, L5
Massara E., Villaescusa-Navarro F., Viel M., Sutter P. M., 2015, J. Cosmology Astropart. Phys., 11, 018
Moore B., Ghigna S., Governato F., Lake G., Quinn T., Stadel J., Tozzi P., 1999, ApJ, 524, L19
Nadathur S., 2016, MNRAS, 461, 358
Neyrinck M. C., 2008, MNRAS, 386, 2101
Nickerson S., Stinson G., Couchman H. M. P., Bailin J., Wadsley J., 2011, MNRAS, 415, 257
Nickerson S., Stinson G., Couchman H. M. P., Baili J., Wadsley J., 2012, in Capuzzo-Dolcetta R., Limongi M., Tornambè A., eds, Astronomical Society of the Pacific Conference Series Vol. 453, Advances in Computational Astrophysics: Methods, Tools, and Outcome. p. 305
Pace F., Baldi M., Moscardini L., Bacon D., Crittenden R., 2015, MNRAS, 447, 858
Padilla N. D., Ceccarelli L., Lambas D. G., 2005, MNRAS, 363, 977
Paillas E., Lagos C. D. P., Padilla N., Tissera P., Helly J., Schaller M., 2017, MNRAS, 470, 4434
Pawlowski M. S., Pflamm-Altenburg J., Kroupa P., 2012, MNRAS, 423, 1109
Perlmutter S., et al., 1999, ApJ, 517, 565
Petraki K., Volkas R. R., 2013, International Journal of Modern Physics A, 28, 1330028
Pettorino V., Amendola L., Baccigalupi C., Quercellini C., 2012, Phys. Rev. D, 86, 103507
Pisani A., Sutter P. M., Hamaus N., Alizadeh E., Biswas R., Wandelt B. D., Hirata C. M., 2015, Phys. Rev. D, 92, 083531
Planck Collaboration et al., 2014a, A&A, 571, A16
Planck Collaboration et al., 2014b, A&A, 571, A23
Planck Collaboration et al., 2016a, A&A, 594, A13
Planck Collaboration et al., 2016b, A&A, 594, A16
Pogosyan D. Y., Starobinsky A. A., 1993, MNRAS, 265, 507
Pollina G., Baldi M., Marulli F., Moscardini L., 2016, MNRAS, 455, 3075
Power C., 2013, Publ. Astron. Soc. Australia, 30, e053
Ratra B., Peebles P. J. E., 1988, Phys. Rev. D, 37, 3406
Reid B. A., et al., 2010, MNRAS, 404, 60
Riess A. G., et al., 1998, AJ, 116, 1009
Rozo E., et al., 2010, ApJ, 708, 645
Sawala T., et al., 2016, MNRAS, 457, 1931
Sheth R. K., van de Weygaert R., 2004, MNRAS, 350, 517
Starobinsky A. A., 1980, Physics Letters B, 91, 99
Sutter P. M., Ricker P. M., 2008, ApJ, 687, 7
Sutter P. M., et al., 2014a, VIDE: The Void IDentification and Examination toolkit, Astrophysics Source Code Library (ascl:1407.014)
Sutter P. M., Elahi P., Falck B., Onions J., Hamaus N., Knebe A., Srisawat C., Schneider A., 2014b, MNRAS, 445, 1235
Sutter P. M., Carlesi E., Wandelt B. D., Knebe A., 2015, MNRAS, 446, L1
Suzuki N., et al., 2012, ApJ, 746, 85
Tegmark M., et al., 2004, Phys. Rev. D, 69, 103501
Trowland H. E., Lewis G. F., Bland-Hawthorn J., 2013, ApJ, 762, 72
Tsujikawa S., 2013, Classical and Quantum Gravity, 30, 214003
Vikhlinin A., et al., 2009, ApJ, 692, 1060
Wetterich C., 1988, Nuclear Physics B, 302, 668
Wetterich C., 1995, A&A, 301, 321
Xia J.-Q., 2013, J. Cosmology Astropart. Phys., 11, 022
Yang X., van den Bosch F. C., Mo H. J., Mao S., Kang X., Weinmann S. M., Guo Y., Jing Y. P., 2006, MNRAS, 369, 1293
Yang L. F., Neyrinck M. C., Aragón-Calvo M. A., Falck B., Silk J., 2015, MNRAS, 451, 3606
Zhang Y., Yang X., Faltenbacher A., Springel V., Lin W., Wang H., 2009, ApJ, 706, 747
Zivick P., Sutter P. M., Wandelt B. D., Li B., Lam T. Y., 2015, MNRAS, 451, 4215
de Felice A., Tsujikawa S., 2010, Living Reviews in Relativity, 13

This paper has been typeset from a TEX/LATEX file prepared by the author.

CHAPTER 5

The Properties of Cosmic Voids in Evolving Dark Sector Cosmologies in the High-Redshift Universe

This chapter presents the following published article:

Cosmic voids in evolving dark sector cosmologies: the high-redshift universe by **Adermann E.**, Elahi, P. J., Lewis G. F., Power, C., 2018, Monthly Notices of the Royal Astronomical Society, Volume 479, 4861–4877.

The study presented in the paper extends the work detailed in Chapter 4 to the high-redshift universe, and is the first published study of void properties in quintessence and coupled dark energy models at high redshift. The paper covers the properties of cosmic voids over the redshift range $z = 1.5 - 12$, in the same three cosmological models that were analysed in the last chapter: the pure quintessence model (ϕCDM), the coupled dark energy model (CDE) and the standard model (ΛCDM). Using hydrodynamical simulations of these cosmological models, we compared the population sizes, void volumes, shapes and densities of voids in each of the three models.

We found that voids continue to be the emptiest in the pure quintessence model, and densest in the standard model, in agreement with our previous work on low-redshift voids reported in Adermann et al., 2017, Chapter 4. We also found that at late times, despite having a smaller population of voids than ΛCDM, both ϕCDM and CDE contain a greater total void volume than ΛCDM. From these results, we concluded that the scalar field within both ϕCDM and CDE causes not only emptier voids in these cosmologies, but also a greater rate of void mergers, potentially due to an increased evacuation rate from within voids. These results further demonstrate the potential of void density as an observational probe of dark energy in our Universe, as the differences in the density of voids between the quintessence

cosmologies and ΛCDM extend to a very large redshift range.

The key figures that show these results are Figures 5.9 and 5.10, and Figures 5.1 and 5.5. Figure 5.9 reveals the differences between the models in the average void density distribution from $z = 12$ to $z = 0$, specifically that ϕCDM consistently produces the emptiest voids and ΛCDM the densest, while Figure 5.10 demonstrates the multiple-σ significance of these differences. The combination of Figure 5.1, which displays the lower abundance of voids at late times in the two alternative models compared to ΛCDM, and Figure 5.5, which reveals that both the alternative models contain a greater total void volume than the standard model, indicate that ϕCDM and CDE exhibit greater void merger rates than ΛCDM.

We end this chapter with further discussion of our results not presented in the published article, starting from Section 5.8.

Important Notes on the Published Paper:

In Section 5.4, we offered an explanation for why other non-Hessian methods of void finding tend to identify much larger underdense regions than Hessian-based methods. To clarify our statement, we are suggesting that void-finding methods that rely on density changes in space are better able to detect the ridges between subvoids within large underdensities than other methods. The consequence is that subvoids (rather than the larger underdensities in which they reside) are more likely to be identified as individual voids by these methods.

We note a minor error in the published paper in Section 5.4, where we reported that 0.3% of voids in the ΛCDM simulation at $z = 0$ have a density greater than the average simulation density, when in fact there are no voids whose density exceeds the average simulation density, as reported in Chapter 3. The correction does not significantly alter the statement made in the paper. The conclusion that our void-finding method does not present problems with possible 'voids-in-clouds' is still valid.

In Section 5.5.4, we wrote, 'Although the relative differences reach $> 25\sigma_0$ in significance at most redshifts, the PDF shapes do not wildly differ from each other, as seen in Fig. 9.' We mean to convey that the PDF shapes associated with each model are fairly similar, as shown by Fig. 9. However, they are still distinctly different from each other, as relative differences between the PDFs reach $> 25\sigma_0$ in significance at most redshifts. Only at $z = 0$ are the CDE and ϕCDM PDF shapes not distinct from each other.

In Section 5.6.1, we proposed that a higher void evacuation rate leads to higher merger rates in the alternative models compared to the standard model, as a result of void walls evacuating more quickly, causing neighbouring voids to merge into a single void. We

acknowledge that void mergers can also involve two void walls joining together to become more dense and contracted (as discussed in Sutter et al., 2014). If the wall is thin enough and not too overdense, our Hessian void finder would identify the two voids as a single void, which we consider merged. However, a study into void mergers is necessary to confirm the physical details of the process.

We have moved a small body of text in Section 5.6.4, 'Although we have not calculated density profiles...in which greatest discrepancy from the standard model was found in the centre.', to a new position two paragraphs below its original position in the published paper. The correction does not alter the discussion, except to minimise confusion in its interpretation.

In Section 5.6.4, we wrote, 'Although we have not calculated density profiles (as the majority of our voids are not spherical)...', by which we mean that the combination of ellipticity and irregularity in many of our voids complicates the process of calculating density profiles, and that because of this, a density average was better suited for identifying density differences.

In Section 5.7, we mention 'cosmological effects', which refers to deviations from General Relativity due to the presence of the scalar field and coupling.

Contributions and Acknowledgements:

The analyses in this paper are all my own work, apart from the contributions detailed below:

The simulations were provided by Dr. Pascal Elahi and Prof. Chris Power.

The fitting code I wrote to find the best-fitting parameter values for the volume and density distributions was based on code originally written by Dr. Joseph Callingham.

The text in this paper was checked and edited by Dr. Pascal Elahi and Prof. Geraint Lewis.

MNRAS **000**, 1–19 (2018) Preprint 20 August 2018 Compiled using MNRAS LATEX style file v3.0

Cosmic voids in evolving dark sector cosmologies: the high-redshift universe

Eromanga Adermann,[1]★ Pascal J. Elahi,[2] Geraint F. Lewis[1] and Chris Power[2]
[1]*Sydney Institute for Astronomy, School of Physics, A28, The University of Sydney, NSW, 2006, Australia*
[2]*International Centre for Radio Astronomy Research (ICRAR), The University of Western Australia, 35 Stirling Hwy, Crawley, Western Australia 6009, Australia*

Accepted 2018 July 5. Received 2018 June 12; in original form 2018 February 22

ABSTRACT
We compare the evolution of voids formed under the standard cosmological model and two alternative cosmological models. The two models are a quintessence model (ϕCDM) and a Coupled Dark Matter-Dark Energy (CDE) model, both of which have evolving and interacting dark sectors. From N-body adiabatic hydrodynamical simulations of these models, we measure the statistics and quantify the properties of voids over the redshift range $z = 1.5 - 12$: these include their population size, volumes, shapes, and average densities. We find that the latter property has potential as a probe of cosmology, particularly dark energy, as significant differences in average void densities exist between the alternative models and the standard model. We postulate that this signature arises from an increased evacuation rate of particles out of voids, or an earlier start to void evacuation, in the alternative models as a direct consequence of the dynamical scalar field, which also leads to greater void merger rates. Additionally, differences between the two alternative models are likely due to the drag force arising from dark sector coupling, acting on dark matter particles in our coupled model.

Key words: dark energy – dark matter – large-scale structure of the Universe – cosmology: observations – cosmology: theory

1 INTRODUCTION

The Standard Model of Cosmology, Λ Cold Dark Matter (ΛCDM), is the simplest and most successful cosmological model of the Universe. It asserts that the universe is spatially flat and dominated by a dark sector, comprised of non-baryonic dark matter and a dominant component of dark energy.

The presence of dark matter is seen through observations of galaxy rotation dynamics and cluster dynamics (Clowe et al. 2006). It is commonly assumed to be a non-relativistic (or 'cold'), non-baryonic form of matter that interacts primarily via the gravitational force, and very likely played an important role in the formation of structure by driving the small-scale clustering of baryonic matter (see Frenk & White 2012). The exact properties, such as mass, of the dark matter particle(s) are unknown, although there are a number of theoretically motivated candidates from high-energy physics whose properties are consistent with observations, for example, the lightest supersymmetric particle (LSP), the Weakly Interacting Massive Particle (WIMP), and the Strongly Interacting Massive Particle (SIMP, Hochberg et al. 2015). Dark energy was discovered through measurements of the redshift-luminosity distance relationship in Type Ia supernovae (Riess et al. 1998; Perlmutter et al. 1999), which revealed the late-time acceleration of cosmic expansion. It is considered a form of negative pressure vacuum energy driving the acceleration, and is characterised by the cosmological constant Λ and the equation of state $w = -1$.

The ΛCDM model has had enormous success in explaining large-scale observations, such as the Cosmic Microwave Background (CMB) anisotropies (Bahcall et al. 1999; Bennett et al. 2013; Planck Collaboration et al. 2014, 2016b), Baryonic Acoustic Oscillations (Blake et al. 2011; Beutler et al. 2012; Anderson et al. 2014), features in the large-scale structure (Beutler et al. 2012), weak gravitational lensing by the large-scale structure (Kilbinger et al. 2013) and galaxy clustering (Alam et al. 2017). As such, it has become the standard model for comprehending the Universe on large scales.

Although ΛCDM is well supported by observations, tensions still exist between some observations and its predictions. For example, ΛCDM overestimates the number of satellite galaxies around galaxies similar to the Milky Way (Klypin et al. 1999; Moore et al. 1999). While this tension

★ E-mail: eromanga.adermann@sydney.edu.au (EA)

could be due to insufficient modelling of feedback processes and their effects (e.g. small subhaloes may not be able to host satellite galaxies due to removal of gas from feedback processes, as suggested by Bullock et al. 2000; Benson et al. 2002; Nickerson et al. 2011, 2012; Sawala et al. 2016), it could also indicate the need for modifications to ΛCDM, perhaps in the form of warm dark matter (for details, see Schneider et al. 2012; Power 2013; Elahi et al. 2014; Lovell et al. 2014), although some studies have shown that warm dark matter does not eliminate small-scale inconsistencies (Schneider et al. 2014). ΛCDM also cannot explain or predict the strong alignment of satellite galaxies observed in the Local Group (e.g. the Vast Polar Structure; Pawlowski et al. 2012; Pawlowski 2018 and the Plane of Satellites; Conn et al. 2013; Ibata et al. 2013 or beyond (e.g. alignments in SDSS data; Yang et al. 2006; Li et al. 2013; Ibata et al. 2014), indicating a further need for extensions or alterations to the model.

The ΛCDM model also has some theoretical shortcomings. One such example is the so-called cosmological constant problem, where the prediction for the value of Λ from quantum field theory (assuming that dark energy arises from the zero-point energy of a fundamental quantum field) is stunningly inconsistent with the value of Λ derived from observations and general relativity, which could be a sign of a fundamental misrepresentation of dark energy by the standard model (for a review, see Weinberg 1989; Martin 2012). Another issue is that the density of dark energy is similar in value to the density of matter today, despite their independent evolution through cosmic time and the very small period in which they should be comparable (for a review, see Sahni 2002). This unlikely coincidence may point to some interdependence within the dark sector that is not accounted for in ΛCDM. Perhaps most frustrating is the lack of theoretical underpinning for dark energy and dark matter – though we can characterise the dark sector with cosmological parameters, its nature remains a mystery.

To address the shortcomings of the standard model, a number of alternative cosmological models have been proposed. For example, the coincidence problem has led to the proposal of models with a time-dependent dark energy density and equation of state. These include quintessence models that feature a dynamical scalar field that drives the accelerated universal expansion instead of a cosmological constant (see Ford 1987; Wetterich 1988; Ratra & Peebles 1988; Tsujikawa 2013). For specific types of potentials, the scalar field density remains close to the matter density throughout most of its evolution, which alleviates the cosmic coincidence problem. Another example of a class of dynamical dark energy models are the $f(R)$ gravity models (for a review, see Tsujikawa 2010), which were proposed to explain dark energy through modifications to gravity on large scales (Capozziello & Fang 2002; Carroll et al. 2004). It is worth mentioning that these models have not been ruled out by the recent confirmation that gravitational waves travel at light speed, while others, such as Galileons, quartic, and quintic Horndeski theories, and some beyond-Horndeski models have (see, for example, Baker et al. 2017; Creminelli & Vernizzi 2017; Ezquiaga & Zumalacárregui 2017).

To constrain the possible models that could explain observations of our Universe, cosmologists have utilised the properties and statistics of the large-scale structure, in particular the overdense substructures (e.g. the halo mass function, Sutter & Ricker 2008) and galaxy cluster gas properties (Baldi et al. 2010; Carlesi et al. 2014b). However, in recent times, cosmic voids (underdense regions occurring within the large-scale structure) have gained momentum as a probe of cosmology, as they are only mildly non-linear structures (due to their low density), which makes them potentially more sensitive probes than overdense structures like haloes and filaments. The properties and growth of overdense structures are heavily influenced by complex baryonic physics and gravitational interactions, meaning that cosmological signatures may be difficult to distinguish from, or even be masked by, non-cosmological effects. In contrast, cosmic voids are relatively simple environments that are much less affected by baryonic physics, meaning that any cosmological signatures in their properties are easier to identify. As such, they have been established as useful probes of dark energy (Bos et al. 2012; Pisani et al. 2015), modified gravity (Voivodic et al. 2017) and alternative cosmological models (Massara et al. 2015; Sutter et al. 2015; Pollina et al. 2016; Achitouv 2017; Adermann et al. 2017; Watts et al. 2017). Voids have also been used in studies and measurements of the integrated Sachs–Wolfe effect signal (Cai et al. 2014; Granett et al. 2015; Kovács 2017), baryonic acoustic oscillations (in void clustering; Kitaura et al. 2016; Liang et al. 2016), and weak lensing studies (Gruen et al. 2016; Sánchez et al. 2017).

This paper will use voids as probes of cosmology, extending the results presented in Adermann et al. (2017) to the high-redshift universe, in order to identify discrepancies between cosmologies at all times, including in the dark matter dominated era. Expanding to high redshift allows us to potentially differentiate between the effects of normalisation (those which are always present and continuously evolving, and those which only appear in the dark energy dominated era) and cosmology. We focus on the properties of voids and their evolution from $z = 1.5 - 12$, a redshift range seldom explored in studies of voids. In Sections 2, 3, and 4, we present a summary of the models examined in this paper, details of the simulations of these models, and our approach to finding voids in the simulations. In Section 5, we present our results, followed by our interpretation and discussion in Section 6. In Section 7, we summarise the findings and implications of the results in this paper.

2 EVOLVING DARK SECTOR MODELS

We compare predictions from the standard model to predictions from two non-standard, evolving dark sector models: an uncoupled quintessence model (ϕCDM) and a coupled dark energy-dark matter model, which we shall refer to as Coupled Dark Energy (CDE) throughout this paper. The key difference between the non-standard models and ΛCDM is the nature of dark energy. Within the non-standard models, a time-dependent scalar field, ϕ, is responsible for dark energy, rather than the cosmological constant, Λ. The CDE model is further distinguished from both ϕCDM and ΛCDM, in that its scalar field is coupled to the dark matter field.

We choose a Ratra–Peebles potential (Ratra & Peebles 1988) for both our non-standard models, given by:

$$V(\phi) = V_0 \phi^{-\alpha} \quad (1)$$

where V_0 and α are constants.

The consequence of including the scalar field in ϕCDM and CDE is that the dark energy density evolves with time, which affects the expansion history of the universe. However, the Lagrangian for the scalar field of the CDE model contains a coupling term, which allows dark matter particles to decay into the scalar field. An additional consequence of the coupling is the presence of a 'frictional' force acting on dark matter particles, which affects the evolution of density perturbation amplitudes. For a more detailed discussion of these models, see Elahi et al. (2015) and Adermann et al. (2017).

3 SIMULATIONS

We produced N-body simulations of the two models of interest, ϕCDM and CDE, and a reference ΛCDM simulation to compare to the alternative models. We choose the coupling parameter, β_0, in the CDE simulation to be 0.05. The choice allows us to maximise any differences between the model and the reference ΛCDM model, while still remaining within the range of allowed coupling (see Pettorino et al. 2012; Xia 2013).

Our simulations were run using DARK-GADGET, a modified version of P-GADGET-2, which is itself a modified version of GADGET-2 (for more details, see Springel 2005; Carlesi et al. 2014a). Our implementation follows that of Carlesi et al. (2014a). We include a separate gravity tree to account for the long range forces arising from the scalar field, and an evolving dark matter N-body particle mass for CDE, arising from the decay of the dark matter density. Each of the simulations had a mass resolution of $m_{dm}(m_{gas}) = 6.9(13)\times10^{10}h^{-1}M_{\odot}$ at $z = 0$, high enough for void identification. Each simulation was contained in a box of size 500 h^{-1} Mpc in length and consisted of 2×512^3 particles (dark matter and gas). The linear power spectrum and the growth factor were calculated using the publicly available Boltzmann code CMBEASY (Doran 2005) and first-order Newtonian perturbation equations. For plots of the growth factor evolution, the Hubble constant evolution and the non-linear power spectrum in each of the simulations, please refer to Section 3 of Adermann et al. (2017).

The initial conditions for the simulations were produced using a modified version of the publicly available N-GENIC, by perturbing particles in a Cartesian grid with the first-order Zel'dovich approximation. The modified N-GENIC code uses the growth factors $f = \mathrm{d}\ln D(a)/\mathrm{d}\ln a$ (which were calculated by CMBEASY) to determine the particle displacements in the alternative cosmologies. We chose to match the cosmological parameters h, Ω_m, Ω_b and σ_8 among the simulations at $z = 0$, rather than $z = z_{CMB}$ (redshift of the CMB). The values were chosen to be consistent with the $z = 0$ ΛCDM Planck data (Planck Collaboration et al. 2014, 2016a), with (h, Ω_m, Ω_b, σ_8) = (0.67, 0.3175, 0.049, 0.83) for all three simulations. Matching the parameters at $z = 0$ results in the alternative models having a different expansion history in the early universe compared to ΛCDM. Each simulation begins at $z = 100$, with the same initial density perturbation phases, resulting in underdense regions forming in the same approximate locations in each simulation. This leaves any differences among the models to manifest in the density profiles of the underdense regions (according to their individual power spectra), and minimises differences arising from cosmic variance.

Although the simulations do not take into account star formation or feedback physics, recent studies have shown that this should not significantly affect the void population. Paillas et al. (2017) demonstrated that large underdensities remain underdense, regardless of whether full baryonic/hydrodynamic physics is accounted for.

4 VOID FINDING

Following Adermann et al. (2017), we identified voids in the cold dark matter particle distribution in the simulations by calculating the Hessian matrix across the density field, which is given by:

$$H_{\alpha\beta}(\mathbf{x}) = \frac{\partial^2\rho(\mathbf{x})}{\partial x_\alpha \partial x_\beta}. \quad (2)$$

The Hessian matrix can be used to characterise the curvature of the density field, $\rho(\mathbf{x})$ at position $\mathbf{x}$. If all three eigenvalues are negative, the local density field exhibits a minimum along all directions, and is thus void-like. Various combinations of positive and negative eigenvalues characterise sheet-like, filament-like and knot-like regions within the density field.

To calculate the Hessian matrix and its eigenvalues across an entire simulation box, we first divided it up into a grid of $500\times500\times500$ cubic cells, each 1 h^{-1} Mpc in length. Particle densities were calculated using a smooth particle hydrodynamics kernel, and then were assigned to the nearest grid cell, and used to determine an average density for each cell. The densities were then convolved with a Gaussian kernel, with $\sigma = 3$ h^{-1} Mpc, in order to remove small-scale noise in the density field. We then calculated the Hessian matrix for each cell, and used its eigenvalues to identify the cells that were void-like. We grouped the neighbouring void-like cells together with a friends-of-friends algorithm, with the requirement that neighbouring cells could only be linked if both are void-like cells, or the second is a sheet-like cell. Each void group thus included a boundary layer of sheet-like cells of thickness 1 h^{-1} Mpc. Void groups were only classified as voids if their total volume consisted of at least two void-like cells linked together (with a corresponding volume of 2 h^{-3} Mpc^3), as smaller groups consisting of one void-like cell may be spurious voids, and the resolution of our grid does not allow us to distinguish between these voids and genuine voids with volume 1 h^{-3} Mpc^3.

Recent structure finder comparison projects (Libeskind et al. 2018) have revealed that there is a good agreement between most void-finding methods, especially in the shape of the void density profiles. We note that the Hessian-based methods were associated with smaller volume-filling fractions than other methods, which is consistent with our results. However, the void-filling fraction within our simulations is still smaller than what was calculated using other Hessian-based methods, potentially because of the difference in the eigenvalue thresholds used. While other methods set their threshold based on visual comparisons, we set ours based on a physical definition of voids as density minima.

We also suggest that other, non-Hessian methods tend

to identify much larger underdense regions than Hessian-based methods, because Hessian methods rely on density changes in space, allowing the identification of individual density minima within these larger underdensities. Although a small fraction of density minima identified in this way could be 'voids-in-clouds' (approximately 0.3 per cent of voids we identified have an average density greater than the average simulation density at $z = 0$), we argue that this should not be problematic, as long as there is consistency in the methods used to define and identify voids when comparing predictions to observations. More information on how our void-finding method compares to other methods can be found in Adermann et al. (2017) and Libeskind et al. (2018).

5 RESULTS

We present the population size, volume distribution, shape distribution, and average density distribution of voids occurring across the high-redshift universe. Our analysis spans the redshift range from $z = 1.5$ to $z = 12$.

5.1 Population Size

The evolution of the void population size for ΛCDM is shown in Fig. 1, along with the ratios of the ϕCDM and CDE population size to the ΛCDM population size. The number of voids decline with time for all models, and is generally very similar between the models at all redshifts, with all ratios staying close to unity. However, there are small differences between the models worth noting.

Specifically, the ϕCDM and the CDE models have greater void populations than the ΛCDM model at high redshift ($z \approx 4-12$), with ϕCDM having the largest population. At $z \approx 4$, the ΛCDM void population begins to overtake both ϕCDM and CDE, and continues to be most populated until $z = 0$. In the range $z \approx 0.3 - 0.6$, the population size ratios between the alternative models and ΛCDM increase slightly, before decreasing again towards $z = 0$. At $z \approx 0.3$, the population of CDE suddenly declines and the model becomes less populated than ϕCDM.

5.2 Volumes

Following Adermann et al. (2017), we use a probability density function (PDF) to quantify the shape of the void volume distribution across the high-redshift universe. The PDF is defined so that the probability of finding a void with a specific volume V is given by the integral from V to $V + dV$ of the PDF. The number of voids of a given volume that can be expected to exist in a given region can be determined from the PDF by multiplying the probability of finding a void with that volume by the number of voids inside the region. The PDF is given by:

$$f(V) = \frac{1}{V_0 \Gamma(1-\alpha)} (V/V_0)^{-\alpha} \exp(-V/V_0), \quad (3)$$

where V is the void volume in h^{-1} Mpc, defined as the number of 1 h^{-1} Mpc void-like cells comprising the void (excluding sheet-like cells). The parameter α is the slope of the power law, V_0 is the characteristic volume that determines the position of the turnover, and $\Gamma(1-\alpha)$ is the gamma function evaluated at $1-\alpha$. The best-fitting values for the parameters α and V_0 were determined by fitting Equation 3 to the set of void volumes at each redshift in all simulations, and are shown in Table 1. The fitting was performed using a Markov chain Monte Carlo (MCMC) algorithm with the Python EMCEE library (Foreman-Mackey et al. 2013).

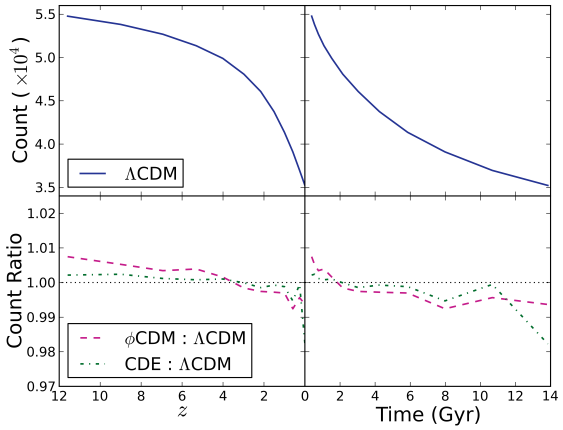

Figure 1. Left-hand panels: The evolution of the total number of voids found in the ΛCDM model across the redshift range $z = 0-12$ (top panel), and the ratio of the population size in the ϕCDM (dashed magenta) and CDE (dot–dashed green) models to the ΛCDM model (bottom panel). A ratio of one is indicated by the black dotted line. Right-hand panels: The evolution of the total number of voids in each model as a function of the age of the universe, calculated using the same cosmological parameters used in our simulations.

The PDF distributions in the ΛCDM simulation at a select number of redshifts is presented in Fig. 2. It is clear from the figure that the lower the redshift, the greater the probability of finding large voids ($V \gtrsim 10^3$ h^{-3} Mpc^3). This trend is exhibited across the entire set of snapshots we analysed. However, in the volume range $V \approx 4-300$ h^{-3} Mpc^3, a different trend emerges; the lower the redshift, the lower the probability of finding these voids. The PDF distributions for different z intersect with each other at $V \approx 300 - 310$ h^{-3} Mpc^3, because the higher redshift curves experience a faster drop off than the lower redshift curves (due to a combination of the slightly shallower power-law slope and the exponential drop off at lower volumes for higher redshift curves). At the lowest volumes (2 h^{-3} Mpc^3 $\leq V \lesssim 4$ h^{-3} Mpc^3) the PDFs show the same trend as at high volumes; the smallest voids occur more frequently at low redshift than at high redshift. Although the rate of growth and coalescence of these smallest voids may not be numerically converged, the trends observed are likely physical, and supported by the large number of small voids. The power-laws at lower redshifts are shallower than at higher redshifts, resulting in another intersection between the PDF distributions at approximately $4-5$ h^{-3} Mpc^3. However, it must be noted that the exact locations of these intersection points are not well constrained, as it occurs at low volumes very close to the noise limit.

The PDF distributions across multiple redshifts for ϕCDM and CDE show similar trends. The intersection points between the PDF distributions for different z also

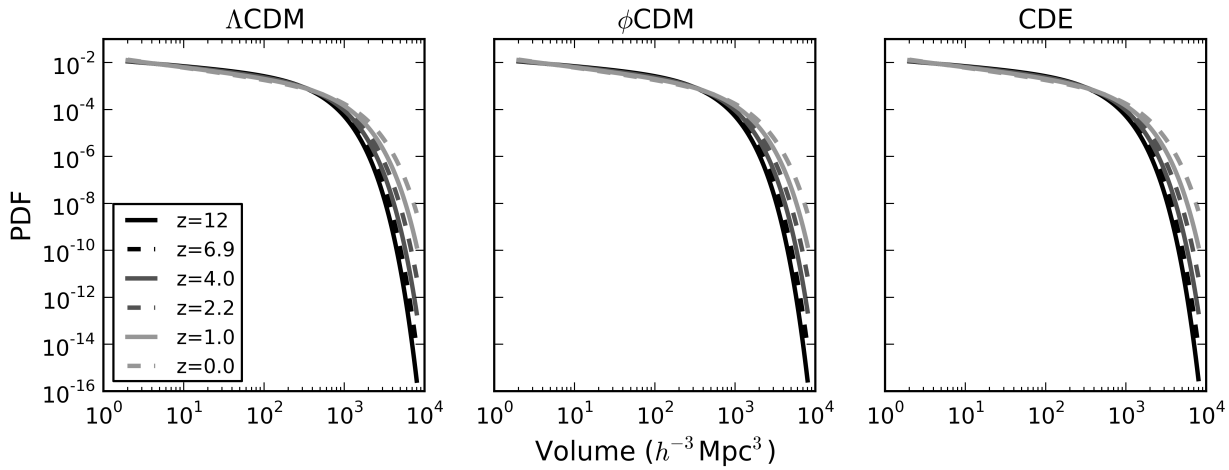

Figure 2. The volume PDF distributions for ΛCDM, ϕCDM and CDE at multiple redshifts.

occurs at $V \approx 300-310\ h^{-3}$ Mpc^3 and $V \approx 4h^{-3}$ Mpc^3 for ϕCDM and CDE. However, the range included between these crossover points is slightly smaller for ΛCDM than for the alternative models. Interestingly, the intersection between the $z = 9$ and $z = 12$ distributions in CDE appears to occur at less than 2 h^{-3} Mpc^3, outside the range probed by our void-finding method. Thus, in the CDE simulation, there are a slightly greater number of the smallest voids at $z = 9$ than at $z = 12$, which is not the case for the other two models.

Comparisons of the volume PDF between the models for $z = 1.5-12$ are presented in Fig. 3 (along with the $z = 0-1$ comparisons for reference), where we show the ratio between each pair of cosmologies. To obtain these ratios, we performed a bootstrapping analysis on the distribution of parameter values that were sampled during the MCMC fitting process. We took a subsample of 5000 values for each of the two parameters, α and V_0, and calculated the ratios between the corresponding volume PDFs they defined. We were thus able to produce a distribution of ratios for each pair of models. We show the median ratios between each pair of cosmologies in Fig. 3[1], along with the 16$^{\text{th}}$ and 84$^{\text{th}}$ percentile ratios, which represent the 1σ uncertainty on the ratios obtained, as the distributions are not necessarily Gaussian. These ratio plots show that across all redshifts studied, the ratios between the PDFs for each pair of cosmologies are consistent with a ratio of unity to within 1σ uncertainty (1σ uncertainty range overlaps with a ratio of one). We observe the same increasing spread in the ratio distributions with volume for the high-redshift universe, as we saw in the low-redshift universe, because the shape of the PDFs at high volume are not as well constrained as at low volume due to lower numbers of large voids. The median ratios also tend to increase with volume, indicating that the disparity between cosmologies is greater in the large void population than the small void population.

[1] We show the ratios of the bin-independent fits, rather than ratios of the raw volume data which would be bin dependent.

At very early times, the ΛCDM PDF is closer to ϕCDM than CDE. Specifically, CDE predicts more large voids $V > 1000\ h^{-3}$ Mpc^3 than the other two models. In the range $z = 9.0-5.3$, CDE converges towards ΛCDM. At the same time, ϕCDM shows greater discrepancy from the standard model, suggesting faster production of large voids within ϕCDM. By $z = 4.0$, ϕCDM contains the largest number of voids with $V > 1000\ h^{-3}$ Mpc^3, and ΛCDM the least. The disparity between ϕCDM and ΛCDM decreases in the range $z = 3.0-2.2$, before increasing again by $z = 1.5$. Despite these changes, it continues to have the largest number of voids in the range $z = 3.0-1.5$. The CDE PDF gradually approaches the ΛCDM PDF in the range $z = 12-1.5$, until their median ratio is nearly unity at $z = 1.5$. However, we note that these systematic differences are affected by the absence of large-scale power. Hence, the evolution described here may not accurately represent the large void populations, although each simulation should be affected in the same way.

Although not shown, the results for smaller voids ($V < 1000\ h^{-3}$ Mpc^3) also show no significant deviation from each other by more than 1σ, but there are small discrepancies among the cosmologies. There is no clear trend for the smallest voids, with each model containing the greatest number of these voids at different redshifts. However, small voids are close to our noise limit, which may hide differences among the models. Across the redshift range $z = 1.5-12$, ΛCDM contains the greatest number of mid-range voids ($V \approx 100\ h^{-3}$ Mpc^3; specific volume range varies with redshift).

In Fig. 4, we present the evolution of the volume PDF parameters α and V_0. The ratios of the parameters in the ϕCDM and CDE models to the ΛCDM parameters are also presented. The uncertainties displayed were calculated by adding the parameter uncertainties in quadrature, while accounting for variation in the upper and lower uncertainties. It is clear from Fig. 4 that α and V_0 increase with decreasing redshift across all models, indicating that the power-law steepness and the exponential cut-off point increases with decreasing redshift. Additionally, the rate of increase for V_0 increases as the models evolve (i.e. $d^2V_0/dt^2 > 0$). Although

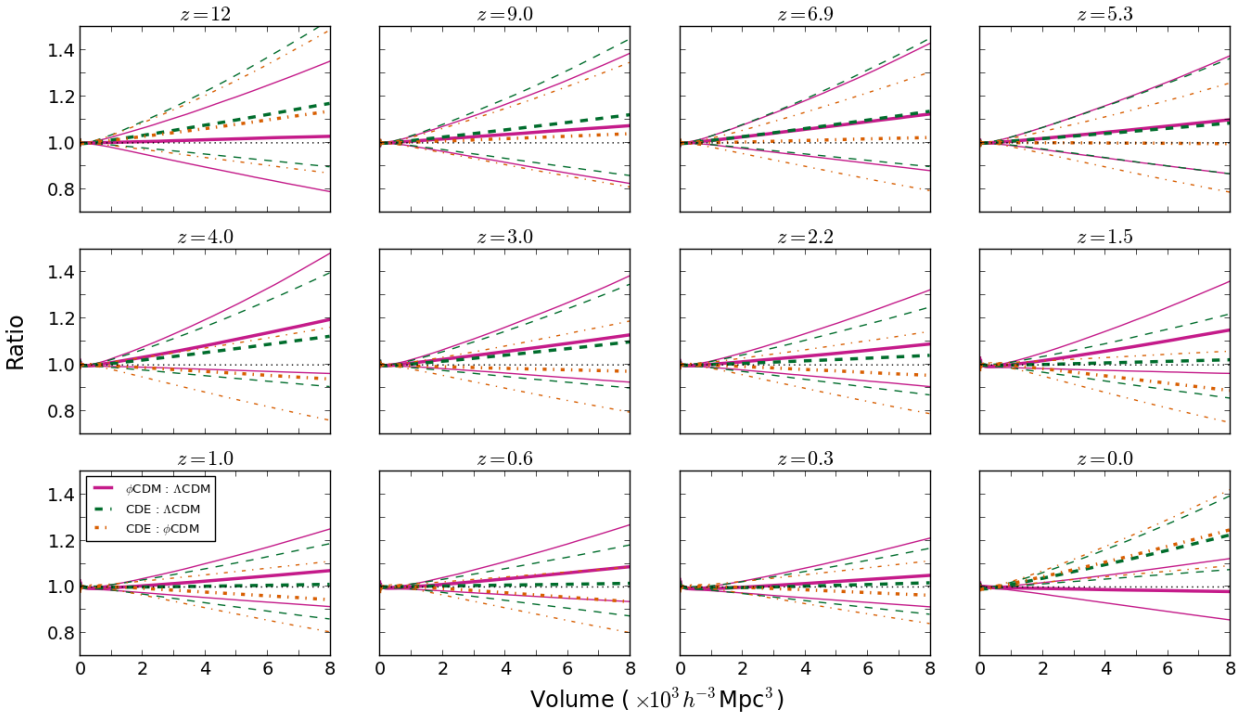

Figure 3. Bootstrapped ratios for the volume PDFs between each pair of the three models, in the range $z = 12 - 0$. We show the median ratio, along with the 16th and 84th percentile ratios, at each redshift. The median ratios are represented by the thickest lines, while the 16th and 84th percentile ratios are indicated by the thinner lines. The ratios between the ϕCDM PDF and the ΛCDM PDF are indicated by the solid magenta lines, while the dashed green lines and the dot–dashed orange lines represent the ratios between the CDE and ΛCDM PDFs and between the CDE and ϕCDM PDFs, respectively.

this rate of increase is generally quite similar across the models, there is one difference; in the range $z = 0 - 0.3$, the parameter V_0 in the CDE model increases much more quickly than in either of the other models. The parameter values are otherwise consistent among the models to within a 1σ uncertainty across all redshifts (uncertainty regions overlap a ratio of one). These trends are also clear from Table 1, which lists the best-fitting values of α and V_0 along with their 1σ uncertainties. [2]

Fig. 5 shows the evolution of the total volume occupied in voids in each cosmological model. We do not show uncertainties arising from cosmic variance, as this would require multiple simulations. Although the discrepancies may not be statistically significant for our sample size, they are still noteworthy due to our effort to minimise the effects of cosmic variance, so that discrepancies may be attributed to differences in cosmology. We find that the ϕCDM model contains the greatest total volume within voids at early times, while ΛCDM contains the least. At $z \approx 3$, the curves intersect and ΛCDM experiences faster growth in total void volume than the other two cosmologies. At late times, ϕCDM contains the lowest total volume within voids.

[2] For reference, the best-fitting values in the range $z = 0 - 1$ are also presented, which covers a total of ~ 8 Gyr in time.

5.3 Shapes

Following Adermann et al. (2017), we fit the voids with ellipsoids and calculated their ellipticity and prolateness. To determine the axis lengths of the best-fitting ellipsoids, we calculated the moment tensor for each void using the sheet-like cells in the boundary layer:

$$M_{ab} = \sum_i (x_i^a - X^a)(x_i^b - X^b), \tag{4}$$

where i represents the sheet-like cells defining the boundary layer of each void, x_i^a and x_i^b are the a-coordinate and the b-coordinate of the i^{th} cell, respectively (where a and b denote x, y, or z), and X^a and X^b are the a-coordinate and b-coordinate of the void barycentre, respectively. The void barycentres were calculated by taking the unweighted average of the boundary cell positions. The eigenvalues e_1, e_2, and e_3 of the moment tensor relate simply to the axis lengths a, b, and c of the best-fitting ellipsoid:

$$e_1 = \frac{a^2}{3}, \; e_2 = \frac{b^2}{3}, \; e_3 = \frac{c^2}{3}, \tag{5}$$

where c is the longest axis and a is the shortest axis.

We define ellipticity of the best-fitting ellipsoid to be

$$e = \frac{1}{4}\frac{c^2 - a^2}{a^2 + b^2 + c^2}. \tag{6}$$

The consequence of our definition is that spheres have an ellipticity of zero, and the value of e increases as the deviation

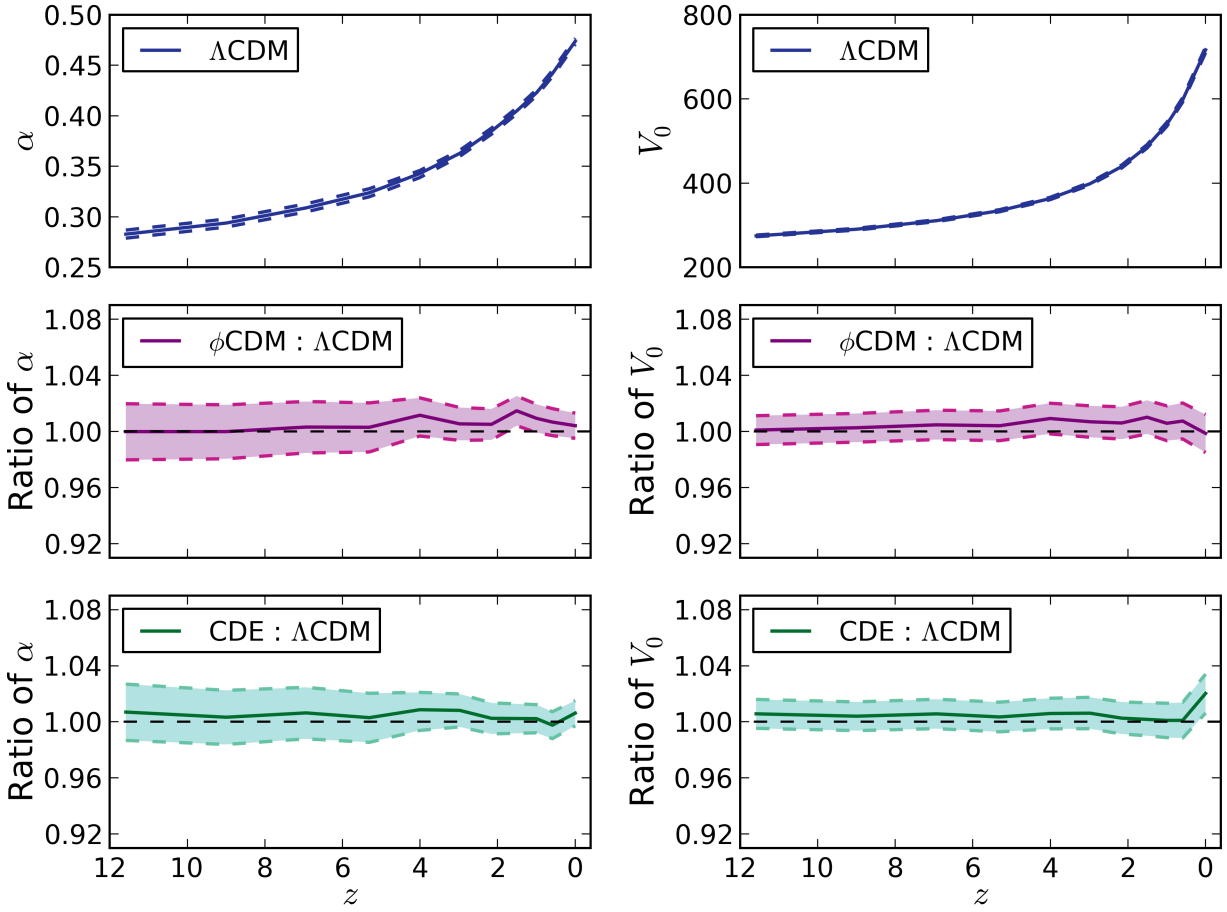

Figure 4. The evolution of the parameters α and V_0 with redshift for the three models. The parameters characterising the void volume PDF in the ΛCDM model are displayed in the first row, with 1σ uncertainties indicated by the dashed lines. The ratio of α and V_0 in the ϕCDM and CDE models to the corresponding α and V_0 in the ΛCDM model are shown in the second and third rows, respectively. The 1σ spread on the ratios are indicated by the coloured regions. A ratio of unity is indicated by the black dashed lines.

Table 1. The best-fitting values (with 1σ uncertainties) for the parameters α and V_0. The values for the $z = 0.0 - 1.0$ are also included for the sake of comparison.

	ΛCDM		ϕCDM		CDE	
z	α	V_0	α	V_0	α	V_0
12	0.283 ± 0.004	275.0 ± 2.0	0.283 ± 0.004	275.3 ± 2.0	0.285 ± 0.004	276.6 ± 2.0
9.0	0.294 ± 0.004	290.9 ± 2.1	0.294 ± 0.004	291.7 ± 2.1	0.295 ± 0.004	292.1 ± 2.1
6.9	0.309 ± 0.004	311.2 ± 2.3	0.310 ± 0.004	312.7 ± 2.3	0.311 ± 0.004	313.0 ± 2.3
5.3	0.324 ± 0.004	334.9 ± 2.5	0.325 ± 0.004	336.3 ± 2.5	0.325 ± 0.004	336.1 ± 2.5
4.0	$0.343^{+0.003}_{-0.004}$	363.8 ± 2.8	0.347 ± 0.003	367.2 ± 2.8	0.346 ± 0.003	366.0 ± 2.8
3.0	0.363 ± 0.003	$399.0^{+3.2}_{-3.1}$	0.365 ± 0.003	$401.8^{+3.2}_{-3.1}$	0.366 ± 0.003	$401.5^{+3.2}_{-3.1}$
2.2	0.385 ± 0.003	$440.0^{+3.6}_{-3.5}$	0.387 ± 0.003	442.7 ± 3.6	0.386 ± 0.003	$441.2^{+3.6}_{-3.5}$
1.5	0.405 ± 0.003	$487.6^{+4.1}_{-4.0}$	0.411 ± 0.003	$492.6^{+4.2}_{-4.1}$	0.406 ± 0.003	$488.5^{+4.1}_{-4.0}$
1.0	0.423 ± 0.003	540.0 ± 4.7	0.427 ± 0.003	$543.2^{+4.8}_{-4.7}$	0.424 ± 0.003	$540.6^{+4.7}_{-4.6}$
0.6	0.442 ± 0.003	$598.3^{+5.4}_{-5.3}$	0.445 ± 0.003	$602.8^{+5.5}_{-5.4}$	0.441 ± 0.003	$599.0^{+5.5}_{-5.3}$
0.3	0.459 ± 0.003	$660.1^{+6.2}_{-6.1}$	0.465 ± 0.003	$664.5^{+6.3}_{-6.2}$	0.462 ± 0.003	$661.7^{+6.2}_{-6.1}$
0.0	0.474 ± 0.003	$717.1^{+6.8}_{-6.9}$	0.476 ± 0.003	716.2 ± 6.9	0.477 ± 0.003	731.7 ± 7.1

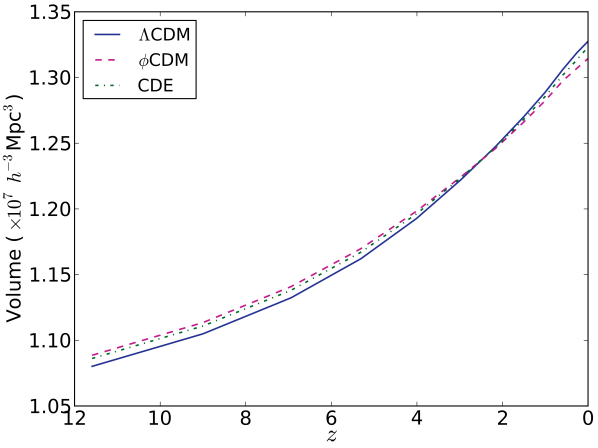

Figure 5. The evolution of the total void volume in each model.

from a sphere increases. Prolateness is defined as

$$p = \frac{1}{4}\frac{(b^2 - a^2) + (b^2 - c^2)}{a^2 + b^2 + c^2}, \quad (7)$$

and characterises the elongation of the axes relative to each other. A negative value of p indicates that one axis is elongated relative to the other two (prolate), while a positive value of p indicates that two axes are elongated relative to the third (oblate).

Fig. 6 shows the distribution of ellipticities and prolateness for voids in each model for selected redshifts. As the smallest voids do not have sufficiently resolved shapes, we included in our subsequent analyses only voids consisting of more than 10 cells. The majority of voids have $p < 0$, and $e \approx 0.1$, for $z = 12 - 1.5$ and for all models. However, each model starts out at $z = 12$ with more voids of (relatively) high prolateness or oblateness (i.e. magnitude of $p \approx 0.1 - 0.2$). As the models evolve, the void populations tend towards more average values of p and e ($p \approx -0.1 - 0$ and $e \approx 0.05 - 0.15$).

This trend can also be seen in how the median e and p values change with redshift. At $z = 12$ the medians in ΛCDM occur at $(e,\ p) = (0.09 \pm 0.03, -0.04^{+0.03}_{-0.04})$[3]. The median e increases slowly with redshift, while the median p decreases slowly with redshift. At $z = 1.5$, the median e and p occur at $(e,\ p) = (0.10 \pm 0.03, -0.05^{+0.03}_{-0.04})$, before settling at $(e,\ p) = (0.11 \pm 0.03,\ -0.05 \pm 0.04)$ when $z = 0$.

The alternative models show very similar trends overall; differences in the median values and scatter are only slight. The only differences are that the median prolateness of voids in ϕCDM is slightly lower than in ΛCDM, and at $z = 1.5$, the scatter in the ellipticity values in CDE is slightly narrower than in the other models. The rate of change in the distributions are also extremely similar among the models.

Plots of the variation in prolateness and ellipticity with volume in Fig. 7 show that the oblate voids, and the voids with the highest ellipticity and lowest ellipticity in ΛCDM decline in number with decreasing redshift. Although this could be affected by small number statistics, the figure also shows that larger voids have a noticeably smaller spread in both prolateness and ellipticity than smaller voids. There is a general trend of decreasing scatter in these shape parameters with increasing volume. This is also reflected in the other two cosmological models. Additionally, there are occasional large voids tending away from the average, with positive p instead of negative. However, the large void population is too small to draw any conclusion about the existence of a significant subset of large, oblate voids.

[3] The upper and lower limits reported here are the 25$^{\text{th}}$ and 75$^{\text{th}}$ percentiles

5.4 Average Densities

For each model, we fit a PDF to the distribution of average void density at different redshifts. The average density for each void was calculated by taking the mean of the cell densities comprising the void, excluding the densities of the sheet-like boundary cells. For each snapshot, the average void density formed a distribution which was best fit with a skewed Gaussian,

$$p(t) = \frac{1}{\sqrt{2\pi}} e^{-t^2/2}\left[1 + \mathrm{erf}\left(\frac{\alpha t}{\sqrt{2}}\right)\right], \quad (8)$$

where $t = (\log_{10}\rho - \mu)/\sigma$, α is the skewness parameter, μ is the mean, and σ is the standard deviation of the associated Gaussian. The best-fitting values for μ, σ and α for all available snapshots are listed in Table 2.

The PDFs showing the average void density distribution in the range $z = 12 - 0$ for each cosmological model are displayed in Fig 8. The peak of the PDFs decrease with time, showing that voids become more underdense with time. The spread of the PDFs also increases with decreasing redshift, suggesting that the range of densities starts off quite narrow at early times and increases as voids evolve (expand, evacuate, and merge). The evolution of the density PDFs in all three models is very similar.

Fig. 9 shows the comparison between the density PDFs at specific redshifts. The density PDFs in the range $z = 0-1$, which were presented in Adermann et al. (2017), are also displayed in this figure for completeness. At $z = 12$, the three models show the most similarity in their density distributions, but remain distinct. The ΛCDM density PDF peaks at a slightly higher average void density than the other two models. As the models evolve, the ΛCDM PDF becomes more distinct from, and continues to peak at a higher average density than, the other two PDFs. At $z = 5.3$, the ϕCDM PDF starts to become more distinct from the CDE PDF, shifting further to the left and showing a wider spread in densities. This indicates that the ϕCDM density PDF starts spreading out to include lower average void densities a sooner than the PDFs of CDE and ΛCDM. From $z = 4.0$ to $z = 1.0$, the three models are quite distinct from each other, with ϕCDM peaked at the lowest void density and with the widest spread, and ΛCDM peaked at the highest and with the narrowest spread. The ΛCDM and CDE PDFs finally attain a similar spread to the ϕCDM PDF by $z = 0.6$, and as observed in Adermann et al. (2017), the CDE PDF approaches the ϕCDM PDF until they converge at $z = 0.0$.

To compare the density PDFs among the models, we performed a bootstrapping analysis on the distribution of parameter values that were sampled during the MCMC fitting process. As with the volume PDF comparisons, we took

z	ΛCDM			ϕCDM			CDE		
	μ	σ	α	μ	σ	α	μ	σ	α
12	-1.4705 ± 0.0003	0.0635 ± 0.0003	$-1.9580^{+0.0242}_{-0.0093}$	-1.4814 ± 0.0004	0.0653 ± 0.0003	$-1.7328^{+0.0231}_{-0.0093}$	-1.4770 ± 0.0003	0.0647 ± 0.0003	$-1.8112^{+0.0233}_{-0.0093}$
9.0	-1.4910 ± 0.0005	0.0680 ± 0.0004	$-1.4970^{+0.0229}_{-0.0004}$	-1.5053 ± 0.0005	0.0698 ± 0.0004	$-1.3010^{+0.0229}_{-0.0004}$	-1.4992 ± 0.0005	0.0691 ± 0.0004	$-1.3750^{+0.0223}_{-0.0004}$
6.9	-1.5179 ± 0.0007	0.0732 ± 0.0005	$-1.1162^{+0.0245}_{-0.0005}$	-1.5373 ± 0.0010	0.0746 ± 0.0006	$-0.9155^{+0.0272}_{-0.0006}$	-1.5282 ± 0.0008	0.0743 ± 0.0005	$-1.0110^{+0.0255}_{-0.0005}$
5.3	$-1.5568^{+0.0015}_{-0.0016}$	$0.0775^{+0.0007}_{-0.0008}$	$-0.7072^{+0.0305}_{-0.0008}$	$-1.6571^{+0.0015}_{-0.0014}$	$0.0866^{+0.0008}_{-0.0009}$	$0.8858^{+0.0305}_{-0.0009}$	$-1.5751^{+0.0027}_{-0.0035}$	$0.0765^{+0.0011}_{-0.0012}$	$-0.5032^{+0.0285}_{-0.0012}$
4.0	-1.6879 ± 0.0012	$0.0993^{+0.0007}_{-0.0008}$	$1.0883^{+0.0291}_{-0.0008}$	-1.7214 ± 0.0010	0.1107 ± 0.0007	$1.2963^{+0.0275}_{-0.0007}$	-1.7054 ± 0.0011	0.1054 ± 0.0007	$1.2073^{+0.0281}_{-0.0007}$
3.0	-1.7554 ± 0.0010	0.1248 ± 0.0008	$1.4656^{+0.0281}_{-0.0008}$	-1.7905 ± 0.0010	0.1359 ± 0.0008	$1.6167^{+0.0284}_{-0.0008}$	-1.7731 ± 0.0010	0.1308 ± 0.0008	$1.5545^{+0.0280}_{-0.0008}$
2.2	-1.8296 ± 0.0010	$0.1522^{+0.0008}_{-0.0009}$	$1.8143^{+0.0306}_{-0.0009}$	-1.8674 ± 0.0010	0.1639 ± 0.0009	$1.9251^{+0.0311}_{-0.0009}$	-1.8472 ± 0.0010	0.1574 ± 0.0009	$1.8596^{+0.0306}_{-0.0009}$
1.5	-1.9093 ± 0.0011	0.1800 ± 0.0010	$2.0624^{+0.0328}_{-0.0010}$	-1.9490 ± 0.0011	0.1917 ± 0.0010	$2.1827^{+0.0337}_{-0.0010}$	-1.9275 ± 0.0011	0.1852 ± 0.0010	$2.1147^{+0.0335}_{-0.0010}$
1.0	-1.991 ± 0.001	0.205 ± 0.001	$2.256^{+0.036}_{-0.001}$	-2.033 ± 0.001	0.217 ± 0.001	$2.368^{+0.037}_{-0.001}$	-2.010 ± 0.001	0.210 ± 0.001	$2.295^{+0.036}_{-0.001}$
0.6	-2.071 ± 0.001	0.226 ± 0.001	$2.415^{+0.039}_{-0.001}$	-2.113 ± 0.001	0.237 ± 0.001	$2.493^{+0.041}_{-0.001}$	-2.092 ± 0.001	0.232 ± 0.001	$2.474^{+0.041}_{-0.001}$
0.3	-2.147 ± 0.001	0.248 ± 0.001	$2.580^{+0.043}_{-0.001}$	-2.177 ± 0.001	0.255 ± 0.001	$2.644^{+0.043}_{-0.001}$	-2.168 ± 0.001	0.252 ± 0.001	$2.601^{+0.043}_{-0.001}$
0.0	-2.208 ± 0.001	0.260 ± 0.001	$2.600^{+0.044}_{-0.001}$	-2.251 ± 0.001	0.272 ± 0.001	$2.715^{+0.046}_{-0.001}$	-2.246 ± 0.001	0.270 ± 0.001	$2.700^{+0.047}_{-0.001}$

Table 2. The best-fitting values (with 1σ uncertainties) for the parameters μ, σ, and α. The values for $z = 0.0 - 1.0$ are also included for the sake of comparison.

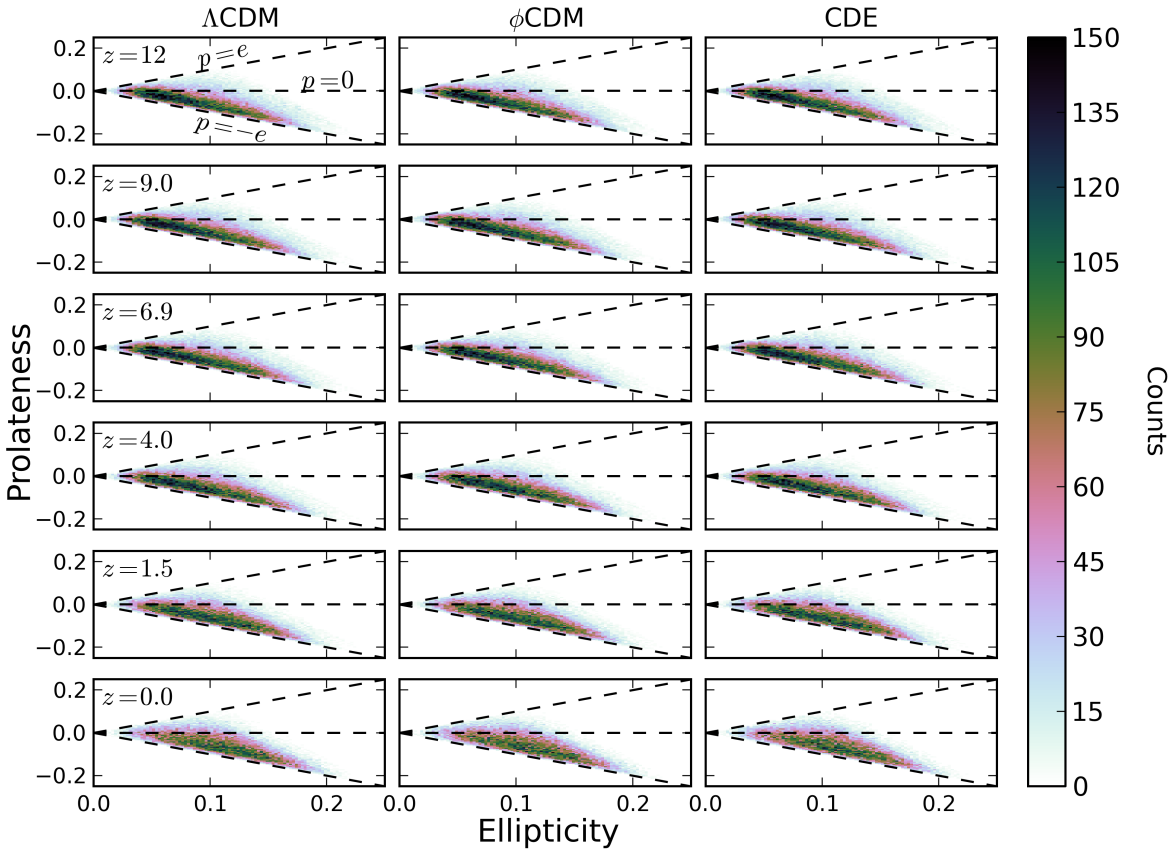

Figure 6. The distribution of ellipticities versus prolateness for the voids in a number of simulation snapshots. We show the distributions for each cosmology for the redshifts z = 0.0, 1.5, 3.0, 5.3, 6.9, 9.0, and 12 (we display the z = 0.0 distributions from Adermann et al. 2017 for reference). The horizontal black dashed line denotes a prolateness of zero. The $p = \pm e$ lines represent the limiting cases where the two shortest axes are equal in length ($p = +e$), and the two longest axes are equal in length ($p = -e$).

a subsample of 5000 values for each of the three parameters, μ, σ, and α, and calculated the ratios between the corresponding volume PDFs they defined, thus producing a distribution of ratios between each pair of models. From these ratios, we calculated the relative difference between each pair of cosmologies, which we define as $(\text{Model1}/\text{Model2} - 1)/\sigma_0$, where Model1/Model2 is the median ratio and σ_0 is equivalent to half the range between the 16$^{\text{th}}$ and 84$^{\text{th}}$ percentile ratios. The relative differences are presented in Fig. 10, highlighting the statistically significant differences between the PDF fit parameters and shapes.

We note that representing the relative differences in terms of a σ_0 defined in this way does not account for the asymmetry in the upper and lower uncertainties associated with the relative difference (or ratio) values. However, since the differences between the density PDFs are very significant, these asymmetries do not have much effect on the accuracy of our representation, while clearly showing the extent of the deviations between the models. [4]

It is clear from the figure that across all redshifts (except at z = 0) the alternative models' average void density distributions are inconsistent with that of the standard model, with much more than a $1\sigma_0$ difference between their distributions. The only crossings with a relative difference of zero occur where the PDFs intersect each other. We note that at z = 0, the relative differences between the CDE and ϕCDM PDF appear to be greater than $1\sigma_0$ for some densities in Fig. 10, but this is only an artefact of our choice to define σ_0 as half the range between the 16$^{\text{th}}$ and 84$^{\text{th}}$ percentiles, not accounting for asymmetry in the ratio distribution and thus slightly underestimating the size of the upper or lower

[4] We did not use relative difference to represent deviations between volume PDFs in Fig. 3. This is because the asymmetries about the median in the 16$^{\text{th}}$ to 84$^{\text{th}}$ percentile range were critical for the accurate representation of the differences and their statistical significance.

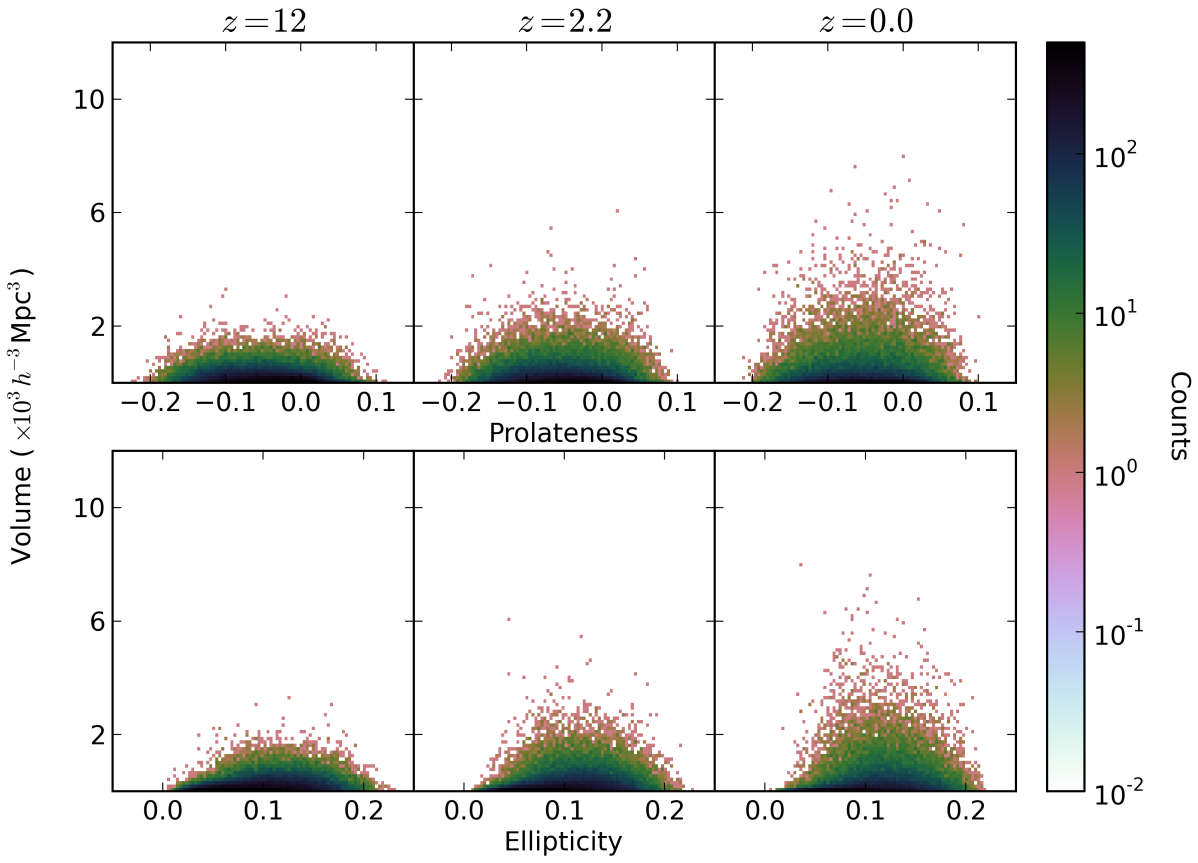

Figure 7. Plots showing how ellipticity and prolateness relate to void volume in the ΛCDM model at z = 12, 2.2, and 0.0. The top row shows prolateness against void volume while the bottom row shows ellipticity against void volume.

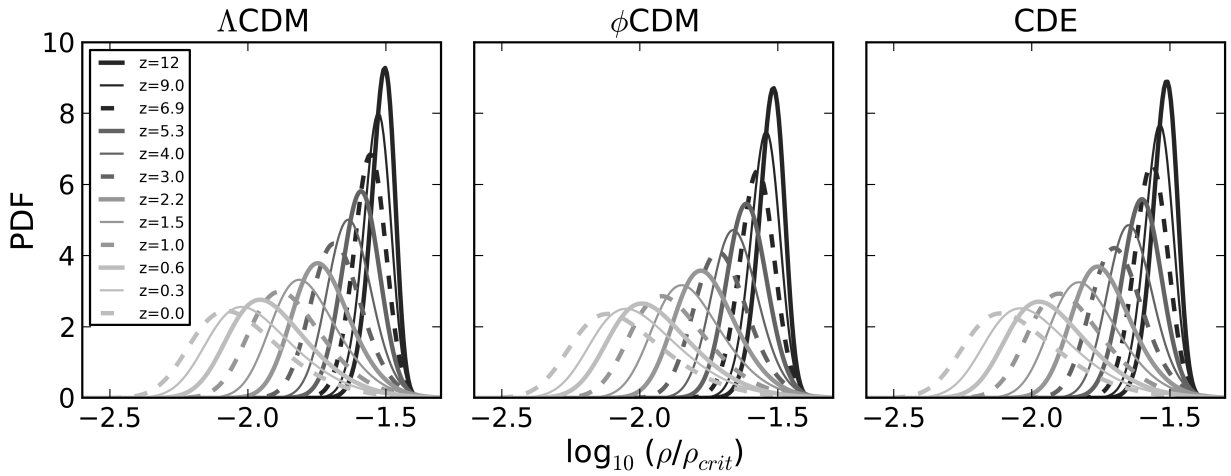

Figure 8. Evolution of the average density PDFs from z = 12 to z = 0.0.

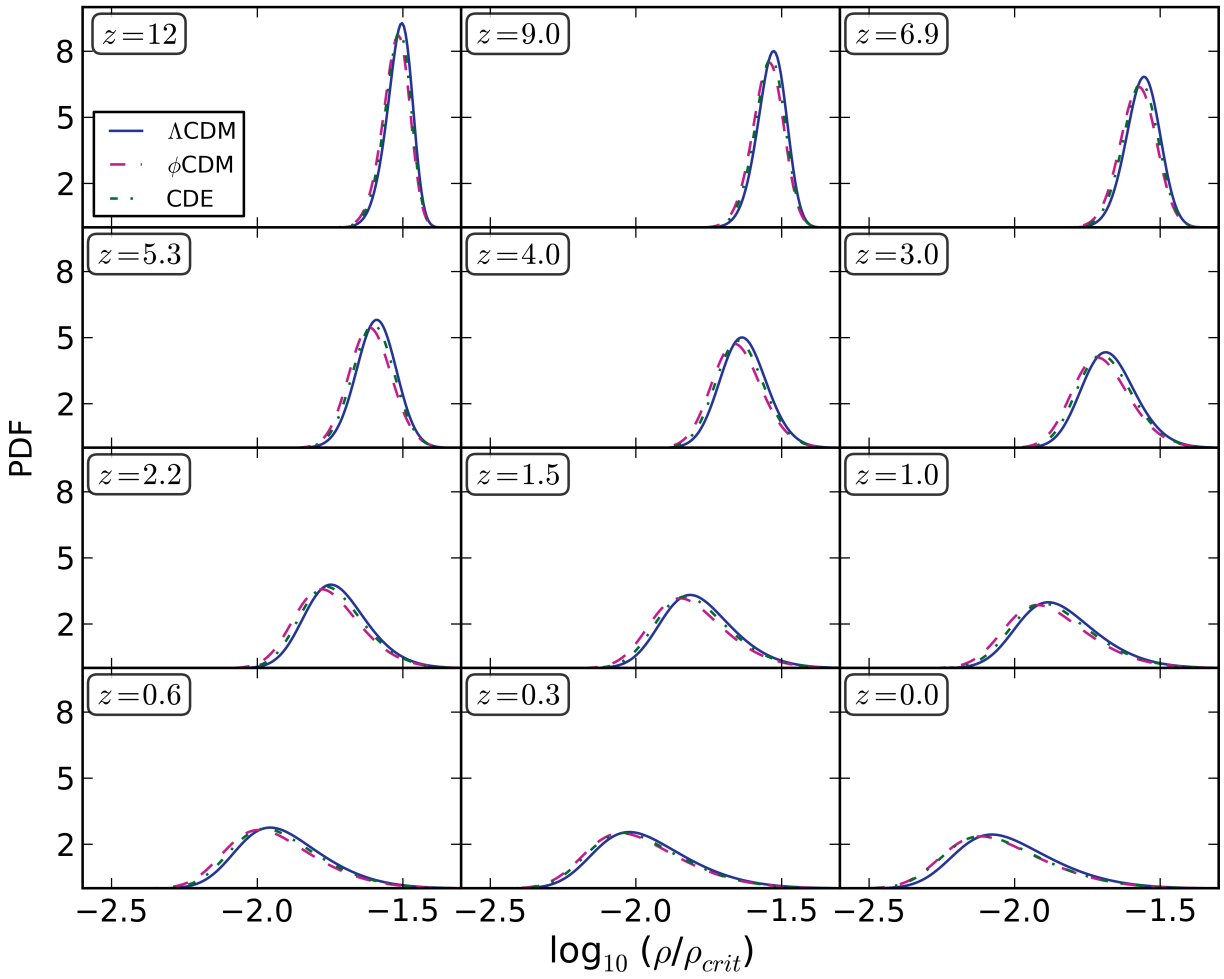

Figure 9. Comparison of the density PDFs among the three models at multiple redshifts.

uncertainty in the median ratio at certain densities. The differences between the CDE and ϕCDM PDFs are not statistically significant, as reported in Adermann et al. (2017). Although the relative differences reach $> 25\sigma_0$ in significance at most redshifts, the PDF shapes do not wildly differ from each other, as seen in Fig. 9. We also note that the relative differences between models at $z = 5.3$ exhibit a different shape than those at other redshifts, because each density PDF undergoes a transition from negative to positive skewness at approximately this redshift, but not at exactly the same time.

In Fig. 11, we show the evolution of the best-fitting density PDF parameters, μ, σ, and α, across all models and all available redshifts (for completeness, we also display the best-fitting values in the range $z = 1 - 0$). As with the volume parameter ratios, the uncertainties were calculated by adding the parameter uncertainties in quadrature, accounting for asymmetry in the upper and lower uncertainties. All three models show a decrease in μ, and increases in σ and α, with time, indicating greater underdensities and larger spreads in densities with time. The CDE and ΛCDM best-fitting values show the greatest similarity, while ϕCDM shows the greatest deviation from the other two models, particularly in μ and α and from $z = 7$ to $z = 4$.

The ϕCDM PDF changes shape earlier than the other two PDFs. Specifically, the skewness changes from negative to positive (α changes sign) earlier, and the PDF experiences an earlier and faster decline in the peak density in the range $z \approx 7 - 5$ before slowing down again. The ΛCDM and CDE PDFs experience the faster decline in the range $z \approx 5 - 4$. As can be seen in the second and third rows of Fig. 11, the ϕCDM and CDE parameters are largely distinct from those of ΛCDM.

6 DISCUSSION

A key element in the interpretations of our results is the fact that our simulations begin with matching density perturbation phases, allowing for initial over- and underdensities to seed in the same location independent of cosmology. This

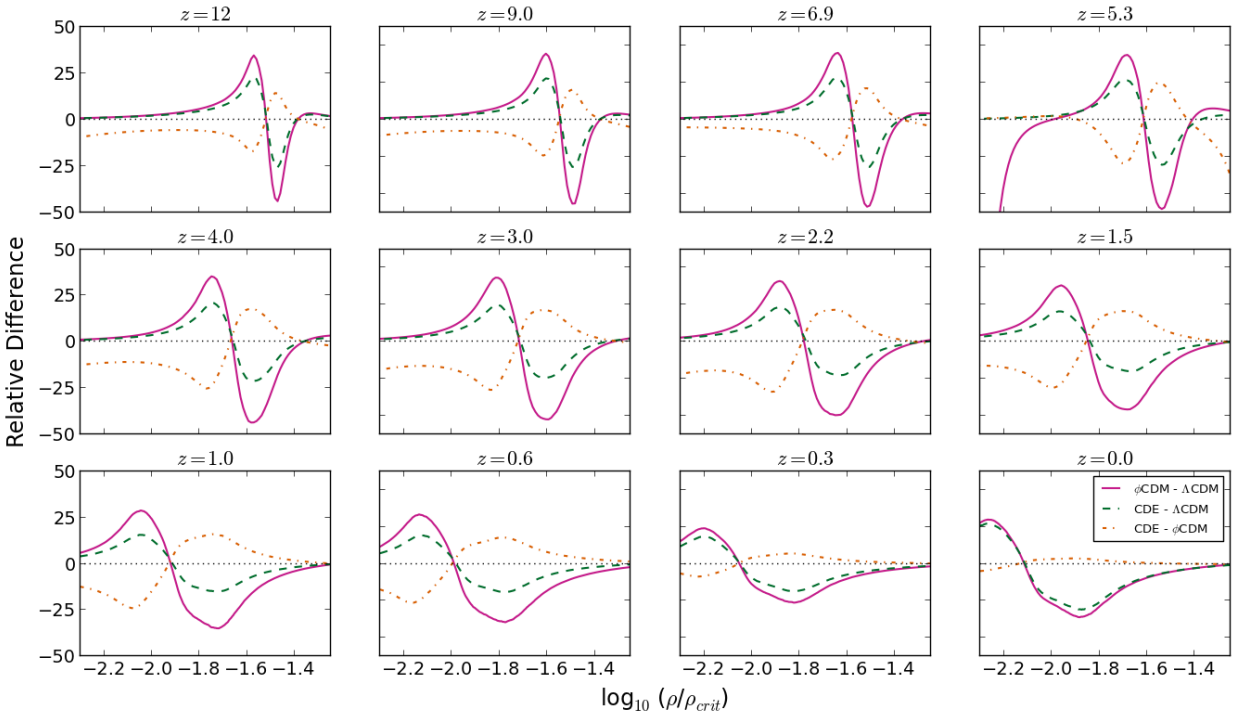

Figure 10. The relative differences in the density PDFs between each pair of the three models, ϕCDM and ΛCDM (solid magenta line), CDE and ΛCDM (dashed green line), and CDE and ϕCDM (dot–dashed orange line), in the range $z = 12 - 0$ (later redshifts included for reference). The relative differences were calculated using the median ratios and are expressed in units of half the range between the 16$^{\text{th}}$ and 84$^{\text{th}}$ percentiles. A relative difference of zero is indicated by the dotted black line.

means that differences among the simulations are due to the differences in expansion history and the growth of the density perturbation amplitudes, hence underlying cosmology, rather than cosmic variance. The differences we focus on in this section are at least 1σ deviations. However, due to the phase matching and enforcing the same σ_8 at $z = 0$, any systematic differences that are within a 1σ consistency are still informative, especially if they do not decrease with redshift.

6.1 Population Size

The fact that the void population size is similar across the models for all redshifts shows that the primary determinant of void formation and growth is gravitational interactions (present in all models). However, given that these simulations start with the same initial density perturbation phases (which allow the same voids to appear in each simulation at the beginning), the small discrepancies we observe in the population sizes are notable, and likely to be directly linked to differences in dark sector physics.

The decline in population size with time for all three models is due to the merger of smaller voids (initially mildly non-linear) into larger voids. The general decline in the ϕCDM and CDE void population sizes compared to the standard model could be due to differences in void merger rates between the models. In particular, the alternative models appear to have a greater void merger rate than the standard model, resulting in these models containing fewer voids than the standard model at late times. This increased void merger rate may be due to a higher particle evacuation rate from voids in the alternative models associated with the dynamical scalar field (proposed in Adermann et al. 2017). The wall of particles between two nearby voids would evacuate more quickly, enabling the two voids to merge earlier than they would under the standard model. A greater void evacuation rate could also reasonably lead to faster void formation and thus more voids at higher redshifts compared to ΛCDM, as seen in Fig. 1.

At $z \approx 0.3 - 0.6$, we observe a sudden increase in the population ratios. This could be the result of a change in the relative merger rates between the alternative models and the standard model somewhere in this redshift range, either due to changes in the ΛCDM merger rate or changes associated with the scalar field. More in-depth investigation into merger rates is needed to pinpoint the exact cause of the increase.

The drag force on baryons due to dark sector coupling is the likely reason for the less pronounced deviation between the CDE and ΛCDM void populations, as the additional drag force would slow down void evacuation rates and thus merger rates compared to ϕCDM. However, the sudden decline in the CDE void population compared to ϕCDM at very late times, suggests an additional effect is at play. This decline occurs when the average density distribution of CDE voids approaches that of ϕCDM voids, and when its large void population ($V > 1000\ h^{-3}$ Mpc^3) becomes significantly greater than the other two models (see Adermann

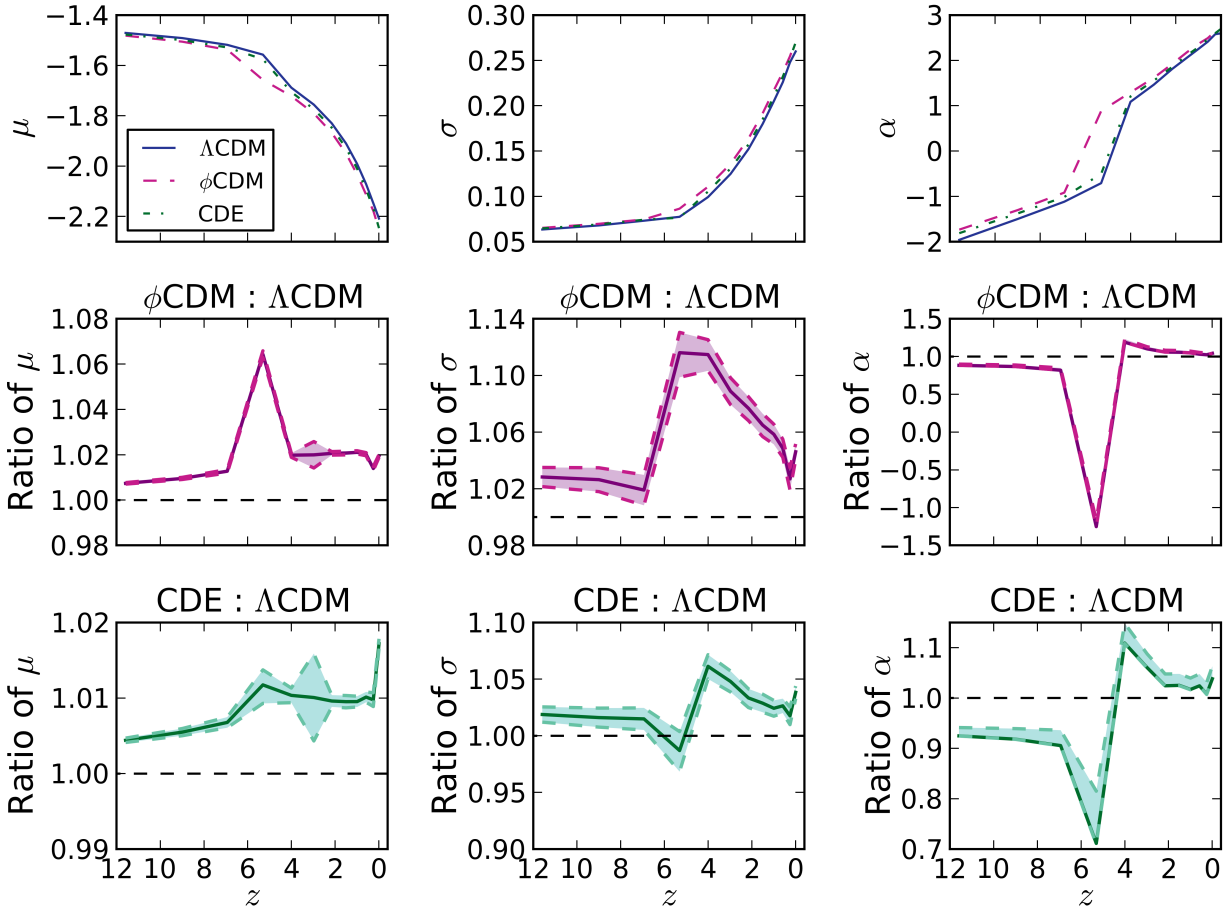

Figure 11. Evolution of density fit parameters and their ratios with 1σ uncertainties, in the range $z = 12 - 0$. The evolution of the best-fitting values in each of the models is displayed in the first row. The ratio between the ΛCDM best-fitting values and those of the ϕCDM and the CDE models are displayed in the second and third row, respectively. A ratio of unity is represented by the black dashed line.

et al. 2017). One likely explanation is a sudden increase at very late times in the evacuation rate of the CDE voids compared to ϕCDM, which would reduce the average void densities and increase the merger rate in the CDE model, explaining both the greater number of large voids and the drop in void population. However, it is unclear how coupling might increase the evacuation rate at very late times. Further study into void merger rates and how they vary with redshift and model is required to explain these changes in the CDE model (Adermann et al., in preparation).

6.2 Volume Distributions

The volume distributions seen in Fig. 3 are very similar in shape to each other and to the PDFs presented in Adermann et al. (2017). We observe that the PDFs turn over at larger volumes as redshift decreases, consistent with a progressive increase in steepness of the power law α and the characteristic volume V_0. The curves show that at higher redshifts for all three models, the probability of smaller voids in any given volume is higher than at lower redshifts, while the probability of larger voids is lower than at lower redshifts. These trends are consistent with what we expect of voids as they merge and expand, which would increase the number of large voids with time while decreasing the number of small voids. However, the trends also show that the rate at which the mid-range voids are replenished is not as great as the rate at which large voids are created. The smallest of voids ($2\ h^{-3}\ \mathrm{Mpc}^3 \leq V \leq 4\ h^{-3}\ \mathrm{Mpc}^3$) tend to become more numerous with decreasing redshift, suggesting that the rate at which they are growing/merging into mid-range voids is less than the rate at which they are forming. Their existence at low redshift shows that small voids appear throughout the evolution of the universe, regardless of model.

The comparisons between the volume PDF parameter values in Fig. 4 and Table 1 show that α and V_0 are almost all consistent with one another between models, and follow the same trend with time. It is clear from the rate of increase in V_0 that the birth rate of larger voids increases with time, meaning that the total void expansion and merger

rate increases with time for all three models. The question of which of the two methods for growing voids largely determines the rate of large void formation will be investigated in later publications, although since mergers are a faster method of growing voids than void wall expansion, we believe that it is dominated by the merger rate. However, the discrepancy ($> 1\sigma$) at $z = 0$ between the CDE value of V_0 and the ΛCDM value reveals that large voids have a faster growth rate at very late times under a CDE cosmology. This is consistent with the population size results, from which we concluded that CDE must have a greater merger rate at very late times in order to have the smallest population size by $z = 0$. Thus, we propose that the increased growth rate of large voids in CDE at late times is the result of an increased merger rate, which in turn is due to an increased particle evacuation rate from voids at late times. This could in fact be the primary cause of the deviation we observed in the CDE volume PDF at $z = 0$ in Adermann et al. (2017), where the CDE model predicted a greater number of voids at high volumes compared to the other two models.

From the lack of statistically significant deviation between the alternative and standard model volume PDFs for large voids ($V > 1000\ h^{-3}$ Mpc^3), across $z = 1.5 - 12$, we can conclude that the growth of voids and their eventual sizes are primarily governed by gravitational effects. However, although not statistically significant, the differences in the median void volumes between the alternative and standard models suggests some small dependence of void volume/growth on cosmology. For example, CDE contains the most large voids at the highest redshifts, until $z \approx 5.3$, when ϕCDM then contains the most (see Fig. 3). This can also be explained by a greater void merger rate in the alternative models compared to the standard model, as void merger rate is positively correlated with the formation rate of large voids. However, this does not explain why CDE starts at $z = 12$ with more large voids than ϕCDM. It is possible that the coupled dark sector leads to greater numbers of large voids at early times, perhaps due to a higher merger rate and/or a higher void wall expansion rate at early times, but the drag force associated with coupling slows down their growth rate so that at later times, ϕCDM contains more large voids.

The fact that the ΛCDM model contains the largest number of mid-sized voids (those with $100 \lesssim V \lesssim 1000\ h^{-3}$ Mpc^3) in the range $z = 1.5 - 12$ can also be explained by the lower merger rate in ΛCDM. A lower merger rate would slow down the creation of large voids more than the creation of mid-sized voids, which can also be formed through void wall expansion. Interestingly, there is no clear trend for the smallest voids ($V \lesssim 100\ h^{-3}$ Mpc^3), with different models containing the greatest number of these voids at different redshifts. This suggests that the growth and depletion of the smallest voids occurs at different rates in each model at different times.

Although the differences we see in the volume distributions suggest differences in void growth rates, stemming from differences in underlying cosmology, we require confirmation of this explanation with further studies of how void merger and void expansion rates differ among the three models, which will be presented in future publications (Adermann et al., in preparation).

In Adermann et al. (2017), we suggested that there could be greater discrepancies in the volume PDF between ϕCDM and ΛCDM at higher redshifts (because the trend in the range $z = 1 - 0$ showed a decline in the discrepancy towards $z = 0$), however we observe that there is no such continuing trend into the higher redshifts. Instead, the ratio between the ϕCDM and ΛCDM volume PDFs rises and falls with time. Without further data, we cannot determine the cause of this. Furthermore, these fluctuations are well within the 1σ uncertainty range, and may well be statistical (for example, from the lack of large-scale power in the simulations) rather than meaningful fluctuations.

Finally, we note that ϕCDM starts out with the greatest total volume and ΛCDM the least total volume at early times, and then this crosses over at $z \approx 2 - 3$ and the opposite order appears (see Fig. 5). At early times, the ϕCDM model has the highest void population (see Section 5.1), and unsurprisingly, the greatest total volume contained in voids. Despite having fewer large voids than the other two models, ΛCDM has the highest void population and the greatest total void volume at late times, which is likely due to having more mid-sized voids than the alternative models. At $z = 0$, CDE has the smallest void population and yet it has a greater total void volume than ϕCDM. This is consistent with the result from Adermann et al. (2017), showing that CDE has more large voids than the other two models, which very likely were the result of increased merger rates, and potentially even an increased void wall expansion rate. These large voids would contribute to the total void volume without adding to the population.

6.3 Shape Distributions

In the range $z = 12$–1.5, void growth/merger dynamics result in only small and slow changes to the void ellipticity and prolateness distributions. Nevertheless, some of these changes may offer insight into the evolution of voids. Firstly, we observed that for all three models, there is a general decrease in the numbers of high-ellipticity and low-ellipticity voids with time[5] (Fig. 6). Secondly, larger voids tend to stay approximately centred around the median values while the scatter in their prolatenesses and ellipticities reduces. Despite the small number statistics and lack of large-scale modes, the existence of these trends in all three models suggests that it is not merely a statistical fluke. However, we acknowledge that since our data does not confirm these trends in simulations with different initial density perturbations, it is possible that these results are not robust under cosmic variance.

While many small voids start out with high ellipticities, when they merge they are much more likely to produce a shape with less extreme values of e and p. This trend is a consequence of the greater number of ways to combine voids into less elliptical shapes, as high-ellipticity voids require more specific and less likely alignments of voids before merging. The tendency towards shapes with $(e, p) \approx (0.1, -0.05)$, even at the highest redshifts, is not as straightforward. Our results suggest that voids tend to evacuate

[5] We define high-ellipticity voids as those with $e \approx 0.2$, which is high compared to the vast majority of the population (but not compared to the full range of ellipticities). Low ellipticity refers to $e \approx 0$.

faster along one direction (producing prolate voids) rather than two or three directions (which would produce oblate or non-elliptical voids), which is consistent with 'Zel'dovich pancake' collapse (see Cautun et al. 2014). Voids do not tend to evacuate at the same rate in all three orthogonal directions in our simulations, which is perhaps not surprising because the cosmic web is not anisotropic along all directions for an observer within a void. However, this does not fully explain why the preferred prolateness is around −0.05, although it could be due to mergers pushing voids towards lower magnitudes of p. It is beyond the scope of our paper to elicit how mergers and void growth affect void shapes. To answer this question, we require the shape distributions for multiple simulation volumes with differing initial density perturbations, as well as void tracking to identify the interplay between mergers and evacuation in void growth and evolution.

The trends discussed so far do not vary with model. Thus, we conclude that the average shape distributions and the processes that produce them are generally insensitive to underlying cosmology, and are largely determined by gravity. This may not be surprising considering that void shape is defined by the boundary of the void, which is classified as sheet material, and is thus somewhat non-linear in its growth. Despite this, there do exist distinct differences in the shapes of the largest voids between the cosmological models. These are differences in the growth and evolution of individual voids, which are noteworthy because the simulations start out with the same initial density perturbation phases. Any alterations in their growth and evolution is due to differences in cosmology, and so it would be useful to isolate these differences for further investigation in void-by-void comparison studies. There may be further individual differences amongst the smaller voids that are not visible in the shape distributions due to the sheer number of similarly sized and shaped voids, but would be observable individually, which could offer further insight into the effect of dark sector physics on the growth and evolution of voids.

6.4 Average Density Distributions

The density evolution observed in Fig. 8 and Fig. 11 is consistent with our understanding of how voids evolve under gravity. At high redshift, voids have a much narrower range of average densities. They generally become less dense due to their increasing size (from expansion and mergers) and continual evacuation of matter as they accumulate on to denser structures. Since the rate of emptying depends on the specific local structure around each void, and thus varies across the population, the spread of average densities increases over time. This gravity-dominated evolution is evident in all three models.

However, dark sector physics does leave a potentially observable imprint on the evolution of void densities, which is clear from Figures 9 and 10. The three models predict distinct density PDFs at all redshifts except for $z = 0$ (the $z = 0$ case was discussed in Adermann et al. 2017). In particular, the ϕCDM density distributions consistently peak at lower densities than the other models, while ΛCDM consistently peaks at higher densities. It is clear that on average, the ϕCDM cosmology produces the emptiest voids and ΛCDM produces the densest, while CDE is somewhere in between. This phenomenon occurs throughout the entire evolution, from at least $z = 12$ to $z = 0$.

Since the observed deviation does not shrink with time, we conclude that it is not the result of normalisation, and that the scalar field is leaving this imprint on the average density of voids. Average density is affected by both the size and evacuation rate of voids. However, the lack of significant differences in the void volume distribution among the models suggests that this is not the primary cause of lower density voids in ϕCDM. Instead, we propose that the scalar field affects their evacuation rate. Additionally, as dark energy in CDE and ϕCDM arise from the same mechanism (dynamical scalar field) and differ in the degree to which dark matter and the scalar field are coupled, we can conclude that the coupling and its associated effects cause the voids in the CDE model to be more dense than those in the ϕCDM model, while the scalar field forces voids to be less dense than those in the ΛCDM model. The coupling leads to a drag effect on the dark matter particles, which slows down their evacuation from voids.

The differences between ϕCDM and the other two models is also apparent in Fig. 11. In particular, the shape of the ϕCDM PDF evolves more quickly than in the other two models, with the change of skewness sign and the drop in peak density occuring at earlier times, due to faster evolution and evacuation of voids. Interestingly, the shape of the parameter evolution curves for CDE and ΛCDM are remarkably similar, despite the parameter values being different. The decline in peak density happens at very similar rates, as well as the rise in the overall spread of the PDFs, and the change in skewness. The effect of coupling seems to override the effect of the scalar field when it comes to the overall parameter evolution, and thus shape evolution, bringing it much closer to a ΛCDM cosmology than a ϕCDM cosmology, despite the shifted density PDFs.

Although we have not calculated density profiles (as the majority of our voids are not spherical) and determined the exact effect of the scalar field on their shapes, we expect the increased evacuation rate in our quintessence models to result in statistically significant lowered densities across most of the void, with greatest discrepancy from ΛCDM occurring at the void centre. This is consistent with the density profile results presented in Pollina et al. (2016) for their coupled dark energy model at low redshift, in which greatest discrepancy from the standard model was found in the centre.

Although the dynamical scalar field characterised by the Ratra–Peebles potential leaves a statistically significant and potentially observable imprint on the average void densities, the differences we see may be fairly model dependent. Another potential could produce a different imprint (including no imprint), on void density. However, most simple scalar field models are required to reproduce the approximate expansion history of ΛCDM. Hence the scalar field density, Ω_ϕ, must exhibit late-time growth. This typically results in a faster rate of growth for Ω_ϕ than Ω_Λ, so if this is a major component of the scalar field's influence over the density of voids, then the imprint we observe could be considered a generic feature of any scalar field cosmology consistent with observations. If this is the case, the observed imprint in the average void density PDFs across a large range of redshifts would be a very promising probe of a dynamical scalar field.

7 CONCLUSIONS

We calculated and compared the void properties over the redshift range $z = 1.5 - 12$ between the ΛCDM model of cosmology and two alternative models, ϕCDM and CDE. Specifically, we compared the size of the void population, the total population volume, the volume distribution, the shape distributions, and the average density distributions.

These properties were derived from three adiabatic hydrodynamical simulations (one for each cosmological model), each of which contained 512^3 dark matter and baryonic particles, in a box of length 500 h^{-1} Mpc. The simulations initially had the same density perturbation phases, so population differences from cosmic variance are not present. Any differences seen thus arise from differences in underlying cosmology.

We used a Hessian-based void finder to identify voids in the cold dark matter distribution of these simulations. We examined the size of the void population and the total volume occupied by voids, their volumes, shapes, and densities across cosmic time, in several cosmologies to identify how cosmology, specifically dark sector physics, affects void evolution and growth.

Firstly, we found that the void population size and its evolution were fairly similar among the three models, which serves as evidence that gravitational effects have the greatest influence on void formation and growth. However, although not statistically significant, there exist a number of small discrepancies between the standard and alternative models, which likely arise from differences in cosmology. The alternative models contained void populations which were greater than that of ΛCDM at early times, and smaller at late times. From this, we concluded that the void merger rate within ϕCDM and CDE is greater than in ΛCDM. We propose that this is due to the increased evacuation rate from voids due to the scalar field, giving rise to more depleted voids in the alternative models than ΛCDM. Furthermore, we propose that the CDE cosmology experiences a sudden increase in its void evacuation rate at very late times, leading to the sudden decline in its void population, the sudden increase in the number of large voids with $V > 1000\ h^{-3}$ Mpc^3, and the sudden consistency between its average void density distribution and that of ϕCDM we have observed at $z = 0$.

Secondly, we found that the void volume distribution cannot distinguish between the models at the 1σ level. The presence of the scalar field or dark sector coupling does not leave a distinct imprint on the volume distribution of voids. Although not statistically significant, slight variations exist between the models. In particular, CDE and ϕCDM both contain more large voids (in the range $V > 1000\ h^{-3}$ Mpc^3) than ΛCDM. Furthermore, the number of large voids in the CDE model relative to ΛCDM and ϕCDM declines with time, and is surpassed by ϕCDM so that by $z = 1.5$, ϕCDM contains the highest population of large voids. We suggested that the coupling present in the CDE model has the effect of increasing the number of large voids at very early times. The very late time increase in the number of large voids in the CDE model could be the result of a sudden increase in the evacuation rate of particles from voids and hence merger rates, leading to the sudden lowering of average void density at $z = 0$. We also discovered that the ΛCDM model contains the greatest number of mid-sized voids with volumes of $\sim 100\ h^{-3}$ Mpc^3 in the entire redshift range, which suggests that ΛCDM has a higher growth rate for mid-sized voids than larger voids, consistent with a lower merger rate than the other two models.

Thirdly, we found that the preference for slightly elliptical voids over spherical ones at low redshifts is also present at higher redshifts. Smaller voids which are less likely to have undergone many mergers tend to exhibit more extreme ellipticities, pointing to the anisotropic, asymmetric nature of void growth (expansion of void walls). Larger voids tend to be closer to the average shape, though not entirely spherical. We proposed that this was due to the averaging out of more extreme shapes by merging. We also suggested that the commonality of slightly elliptical and prolate voids, no matter their volume, is due to anisotropic matter evacuation. These observations are the same across all three models. The ellipticity and prolateness distributions are indistinguishable between the models, and show no obvious traces of the underlying cosmological model. From this, we concluded that the shape of a void, and its evolution with redshift, is dominated by gravitational effects rather than cosmological effects, and hence shape distributions would not serve as a good probe of a dynamical scalar field or coupling.

Finally, we discovered that the form of dark energy, be it a scalar field or the cosmological constant, and dark sector coupling, leaves an imprint on the average void density distributions. We found that the ϕCDM model produces emptier voids on average than CDE or ΛCDM across $z = 1.5-12$, extending the results found in Adermann et al. (2017) for $z = 0 - 1$. Our results support the proposal made by Adermann et al. (2017), that the dynamical scalar field acts to evacuate voids faster than they otherwise would, and the coupling between dark matter and dark energy delays or slows this down due to the drag force acting on baryonic particles moving out of voids. Since this effect is predicted over a large range of redshifts ($z = 0 - 12$), this signature is very promising as an observational probe of the dark sector, particularly as a probe of dynamical scalar fields. Additionally, as there is a good agreement between other void finders and Hessian-based void finders, especially in the void density profiles, we expect this signature to be detectable through other popular void finders that have already been applied to observational data (e.g. ZOBOV, VIDE).

In summary, we have found a number of differences in void population properties between the three models. Specifically, our results suggest that the primary cause of all the discrepancies discovered is an increased evacuation rate from voids in the models containing a dynamical scalar field, which results in a greater merger rate for these models. While some of the imprints we have isolated in this study are not observable unless the void population studied is very large, and contains a sufficient number of large voids, we have found one very promising probe of the dynamical scalar field form of dark energy in the average density distribution of voids, across a wide range of redshifts. It is worth noting that although our proposed explanations are consistent with all of our results, without deeper analyses it is unclear if there are other effects at play we have not been able to isolate in this study (e.g. void wall expansion rate). In future studies, we will attempt to elucidate this situation by calculating void growth rate, wall expansion rate, merger rate, and particle evacuation rate from voids for each

model. While this signature is easily observable in a well-characterised cold dark matter density field, tracer bias may affect its visibility in an observational context, particularly at high redshift. For this reason, we will also consider the impact of using the galaxy distribution to derive the density field, and observational selection for galaxies in the range $z \approx 0-6$ and for 21 cm maps of the cosmic web at higher redshifts, on these signatures. Additionally, we will be investigating the usage of related and more robust observables to amplify the signal we found, in order to minimise the effect of observational limitations.

With a more in-depth understanding of how alternative dark sector physics affects different processes of void evolution, and how observational biases affect signatures, we can develop promising probes of the cosmology of our Universe, and inform the way future large surveys are conducted so that we can effectively constrain the properties and the nature of the dark sector.

ACKNOWLEDGEMENTS

EA acknowledges financial support by the Australian Government and The University of Sydney, through an Australian Postgraduate Award and a University of Sydney Merit Scholarship, respectively. PJE acknowledges funding from the SSimPL programme and the Sydney Institute for Astronomy (SIfA), DP130100117 and DP140100198. The authors acknowledge the University of Sydney HPC service at The University of Sydney for providing HPC resources, in particular the Artemis supercomputer, which have contributed to the research results reported within this paper. URL: http://sydney.edu.au/research_support/. This research made use of the NCI National Facility in Canberra, Australia, which is supported by the Australian Commonwealth Government, with resources provided by Intersect Australia Ltd and the Partnership Allocation Scheme of the Pawsey Supercomputing Centre. We thank Vasiliy Demchenko for enlightening discussions about our void-finding method, and his suggestion to compare the average densities of individual voids with the mean density of the simulation box, as a means of determining the proportion of voids that could be voids-in-clouds.

REFERENCES

Achitouv I., 2017, Phys. Rev. D, 96, 083506
Adermann E., Elahi P. J., Lewis G. F., Power C., 2017, MNRAS, 468, 3381
Alam S., et al., 2017, MNRAS, 470, 2617
Anderson L., et al., 2014, MNRAS, 441, 24
Bahcall N. A., Ostriker J. P., Perlmutter S., Steinhardt P. J., 1999, Science, 284, 1481
Baker T., Bellini E., Ferreira P. G., Lagos M., Noller J., Sawicki I., 2017, preprint, (arXiv:1710.06394)
Baldi M., Pettorino V., Robbers G., Springel V., 2010, MNRAS, 403, 1684
Bennett C. L., et al., 2013, ApJS, 208, 20
Benson A. J., Frenk C. S., Lacey C. G., Baugh C. M., Cole S., 2002, MNRAS, 333, 177
Beutler F., et al., 2012, MNRAS, 423, 3430
Blake C., et al., 2011, MNRAS, 418, 1707
Bos E. G. P., van de Weygaert R., Dolag K., Pettorino V., 2012, MNRAS, 426, 440
Bullock J. S., Kravtsov A. V., Weinberg D. H., 2000, ApJ, 539, 517
Cai Y.-C., Neyrinck M. C., Szapudi I., Cole S., Frenk C. S., 2014, ApJ, 786, 110
Capozziello S., Fang L. Z., 2002, International Journal of Modern Physics D, 11, 483
Carlesi E., Knebe A., Lewis G. F., Wales S., Yepes G., 2014a, MNRAS, 439, 2943
Carlesi E., Knebe A., Lewis G. F., Yepes G., 2014b, MNRAS, 439, 2958
Carroll S. M., Duvvuri V., Trodden M., Turner M. S., 2004, Phys. Rev. D, 70, 043528
Cautun M., van de Weygaert R., Jones B. J. T., Frenk C. S., 2014, MNRAS, 441, 2923
Clowe D., Bradač M., Gonzalez A. H., Markevitch M., Randall S. W., Jones C., Zaritsky D., 2006, ApJ, 648, L109
Conn A. R., et al., 2013, ApJ, 766, 120
Creminelli P., Vernizzi F., 2017, preprint, (arXiv:1710.05877)
Doran M., 2005, J. Cosmology Astropart. Phys., 10, 011
Elahi P. J., Mahdi H. S., Power C., Lewis G. F., 2014, MNRAS, 444, 2333
Elahi P. J., Lewis G. F., Power C., Carlesi E., Knebe A., 2015, MNRAS, 452, 1341
Ezquiaga J. M., Zumalacárregui M., 2017, Phys. Rev. Lett., 119, 251304
Ford L. H., 1987, Phys. Rev. D, 35, 2339
Foreman-Mackey D., Hogg D. W., Lang D., Goodman J., 2013, PASP, 125, 306
Frenk C. S., White S. D. M., 2012, Annalen der Physik, 524, 507
Granett B. R., Kovács A., Hawken A. J., 2015, MNRAS, 454, 2804
Gruen D., et al., 2016, MNRAS, 455, 3367
Hochberg Y., Kuflik E., Murayama H., Volansky T., Wacker J. G., 2015, Physical Review Letters, 115, 021301
Ibata R. A., et al., 2013, Nature, 493, 62
Ibata N. G., Ibata R. A., Famaey B., Lewis G. F., 2014, Nature, 511, 563
Kilbinger M., et al., 2013, MNRAS, 430, 2200
Kitaura F.-S., et al., 2016, Physical Review Letters, 116, 171301
Klypin A., Kravtsov A. V., Valenzuela O., Prada F., 1999, ApJ, 522, 82
Kovács A., 2017, preprint, (arXiv:1701.08583)
Li Z., Wang Y., Yang X., Chen X., Xie L., Wang X., 2013, ApJ, 768, 20
Liang Y., Zhao C., Chuang C.-H., Kitaura F.-S., Tao C., 2016, MNRAS, 459, 4020
Libeskind N. I., et al., 2018, MNRAS, 473, 1195
Lovell M. R., Frenk C. S., Eke V. R., Jenkins A., Gao L., Theuns T., 2014, MNRAS, 439, 300
Martin J., 2012, Comptes Rendus Physique, 13, 566
Massara E., Villaescusa-Navarro F., Viel M., Sutter P. M., 2015, J. Cosmology Astropart. Phys., 11, 018
Moore B., Ghigna S., Governato F., Lake G., Quinn T., Stadel J., Tozzi P., 1999, ApJ, 524, L19
Nickerson S., Stinson G., Couchman H. M. P., Bailin J., Wadsley J., 2011, MNRAS, 415, 257
Nickerson S., Stinson G., Couchman H. M. P., Baili J., Wadsley J., 2012, in Capuzzo-Dolcetta R., Limongi M., Tornambè A., eds, Astronomical Society of the Pacific Conference Series Vol. 453, Advances in Computational Astrophysics: Methods, Tools, and Outcome. p. 305
Paillas E., Lagos C. D. P., Padilla N., Tissera P., Helly J., Schaller M., 2017, MNRAS, 470, 4434
Pawlowski M. S., 2018, preprint, (arXiv:1802.02579)
Pawlowski M. S., Pflamm-Altenburg J., Kroupa P., 2012, MNRAS, 423, 1109

Perlmutter S., et al., 1999, ApJ, 517, 565
Pettorino V., Amendola L., Baccigalupi C., Quercellini C., 2012, Phys. Rev. D, 86, 103507
Pisani A., Sutter P. M., Hamaus N., Alizadeh E., Biswas R., Wandelt B. D., Hirata C. M., 2015, Phys. Rev. D, 92, 083531
Planck Collaboration et al., 2014, A&A, 571, A16
Planck Collaboration et al., 2016a, A&A, 594, A13
Planck Collaboration et al., 2016b, A&A, 594, A16
Pollina G., Baldi M., Marulli F., Moscardini L., 2016, MNRAS, 455, 3075
Power C., 2013, Publ. Astron. Soc. Australia, 30, e053
Ratra B., Peebles P. J. E., 1988, Phys. Rev. D, 37, 3406
Riess A. G., et al., 1998, AJ, 116, 1009
Sahni V., 2002, Classical and Quantum Gravity, 19, 3435
Sánchez C., et al., 2017, MNRAS, 465, 746
Sawala T., et al., 2016, MNRAS, 457, 1931
Schneider A., Smith R. E., Macciò A. V., Moore B., 2012, MNRAS, 424, 684
Schneider A., Anderhalden D., Macciò A. V., Diemand J., 2014, MNRAS, 441, L6
Springel V., 2005, MNRAS, 364, 1105
Sutter P. M., Ricker P. M., 2008, ApJ, 687, 7
Sutter P. M., Carlesi E., Wandelt B. D., Knebe A., 2015, MNRAS, 446, L1
Tsujikawa S., 2010, in Wolschin G., ed., Lecture Notes in Physics, Berlin Springer Verlag Vol. 800, Lecture Notes in Physics, Berlin Springer Verlag. pp 99–145 (arXiv:1101.0191), doi:10.1007/978-3-642-10598-2_3
Tsujikawa S., 2013, Classical and Quantum Gravity, 30, 214003
Voivodic R., Lima M., Llinares C., Mota D. F., 2017, Phys. Rev. D, 95, 024018
Watts A. L., Elahi P. J., Lewis G. F., Power C., 2017, MNRAS, 468, 59
Weinberg S., 1989, Reviews of Modern Physics, 61, 1
Wetterich C., 1988, Nuclear Physics B, 302, 668
Xia J.-Q., 2013, J. Cosmology Astropart. Phys., 11, 022
Yang X., van den Bosch F. C., Mo H. J., Mao S., Kang X., Weinmann S. M., Guo Y., Jing Y. P., 2006, MNRAS, 369, 1293

This paper has been typeset from a TEX/LATEX file prepared by the author.

5.8 Wider Implications

The papers presented in this and the last chapter explored how the physical properties of voids are related to the physics of the dark sector. We showed that void volumes and shapes are not significantly different between the standard model and two models containing an evolving dark sector, but that void density is. We concluded that the presence of the scalar field that also drives accelerated universal expansion causes voids to form with less matter within them. We postulated that the mechanism for producing emptier voids is through an increased evacuation rate, which also manifests itself in the form of a greater void merger rate, as evidenced by the subtle differences in the evolution of void population size and the void volume distribution for very large voids.

The increased evacuation rate can be explained as the result of the scalar field providing its own separate force that acts on the matter within voids, in addition to the usual gravitational force from other particles in the density field. As the scalar field is an additional source of energy in the stress-energy tensor, it exerts its own force on particles within voids, leading to the higher evacuation rate.

We also found differences in the void densities between the two models containing the scalar field. The coupled dark energy model produces emptier voids than the standard model, but denser voids than the uncoupled quintessence model. We concluded that the coupling between the scalar field and the dark matter field has the opposite effect on void density, which is most likely explained by the gravitational drag force that arises from the coupling, which slows down the evacuation of matter from voids.

Similar effects on void density have been found in other alternative models. In particular, other studies conducted on coupled dark energy models have results consistent with ours. Pollina et al. (2016) investigated a coupled dark energy model very similar to our coupled model, featuring a scalar field with a potential given by $V(\phi) = Ae^{-\alpha\phi}$, which differs from ours but exhibits the same behaviour of rapid decline with increasing ϕ, and a coupling strength of $\beta = 0.15$, which is three times as large as ours.

Interestingly, Pollina et al. (2016) found that the voids within their coupled model also display a lower density than the voids within the ΛCDM model, especially near their centres, as evidenced by the comparison between the stacked spherically-averaged radial density void profiles of both cosmological models at $z = 0$ and $z = 1$ (see Figure 5.12). Their comparison shows a distinct, but not statistically significant, difference between the two models. Although the authors did not explain this difference in this way, the scalar field has likely lowered the density of their voids just as it has ours, especially given the similar behaviour exhibited by our potentials. Additionally, their coupled model would have included the drag force that acts on dark matter particles, which limits the disparity in density between the coupled and standard models. As their coupling strength was three times that of ours, the drag force would have been stronger in their model than ours (as it increases with the square of the coupling strength; see Equation 2.8), which may explain the relatively small and statistically insignificant disparity they find compared to ours. The fact that Pollina et al. (2016) found the same signature as we did in their CDE model offers

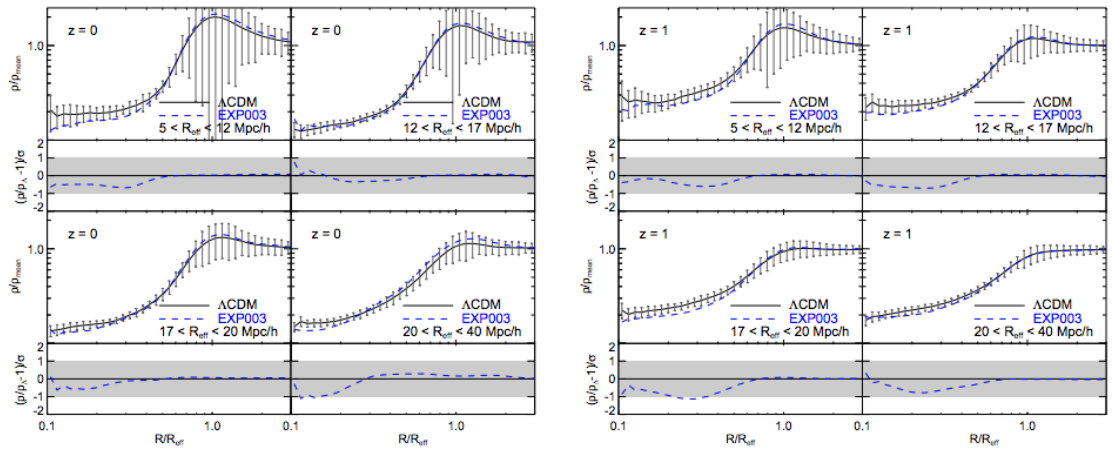

Figure 5.12: The stacked density profiles of cosmic voids within the cold dark matter distribution and the relative differences between them, in four size categories and at $z = 0$ and $z = 1$, showing that the coupled model voids (labelled EXP003; blue dashed lines) have a lower density in their central regions than the ΛCDM voids (black solid lines). The coupled dark energy model has a potential given by $V(\phi) = Ae^{-\alpha\phi}$ and a coupling strength of 0.15. The density value for each radial bin was calculated by averaging values from 100 randomly selected voids, and the error bars represent the sample standard deviation of these voids in each bin. The sub-panels show the relative difference between the profiles in units of the standard deviation of the averaged profile. $\rho_{\rm mean}$ refers to the mean density of the Universe. Credit: Pollina et al. (2016).

additional proof that it is the scalar field giving rise to emptier voids, and shows that it extends more generally to other quintessence models with different potentials.

Even more intriguingly, a number of studies of modified gravity models have yielded similar results to ours. In particular, lowered void density appears in multiple modified gravity models in which a fifth force (from a scalar field) enhances the gravitational force experienced by matter. Cai, Padilla & Li (2015), Barreira et al. (2015) and Falck et al. (2018) found that several $f(R)$ models, a cubic Galileon and a normal Dvali-Gabadadze-Porrati (nDGP) braneworld model, respectively, contain emptier voids than the standard model.

The nDGP model is a stable branch of a modified gravity model where four-dimensional Newtonian gravity is generated from the embedding of a static three-dimensional brane in a five-dimensional Minkowski space (Dvali, Gabadadze & Porrati, 2000). The nDGP braneworld model contains an additional scalar field to produce the acceleration of the expansion of the Universe without introducing a new source of energy. The scalar field makes the gravitational force stronger than in ordinary GR (and Newtonian gravity, in simulations). The consequence of this is an additional 'fifth force' which needs to be screened on small scales to be consistent with GR on these scales, which in the case of

the nDGP model, occurs via the Vainshtein mechanism (Vainshtein, 1972). The $f(R)$ models studied in Cai, Padilla & Li (2015) are similar to the nDGP braneworld model studied in Falck et al. (2018), incorporating an additional scalar field that enhances the gravitational force compared to GR, and requiring a screening mechanism (the chameleon mechanism for the $f(R)$ models). The cubic Galileon presented in Barreira et al. (2015) also contains a gravity-enhancing fifth force, and includes Vainshtein screening.

The $f(R)$ models studied in Cai, Padilla & Li (2015), the nDGP braneworld model studied in Falck et al. (2018) and the full cubic Galileon model studied in Barreira et al. (2015) all exhibit a deeper void density profile, especially in the inner regions, than ΛCDM. They additionally contain a greater abundance of the largest voids than models with standard GR, including ΛCDM. These differences are remarkably similar to those we found between our quintessence models and the standard model.

The one feature that all of these models have in common is an enhanced gravitational force compared to ΛCDM (from the additional fifth force), which is not entirely screened within voids, and indeed the authors of the above studies suggest that the increased emptiness of voids in these models is the result of an increased gravitational force acting on the particles evacuating out of voids. The fifth force within voids can be seen as an additional repulsive force in these models, giving rise to faster wall expansion and particle evacuation. The effect of the quintessence scalar field on void evacuation can be viewed in this way: the scalar field provides an additional force on the particles within voids that drives particles to evacuate out of them at an increased rate. In this regime, the additional force is the result of an additional source of energy in the stress-energy tensor, rather than a modification to the way spacetime responds to energy sources, as it is in modified gravity models. The gravitational force acting on these particles does not differ from ΛCDM (GR); the particles are merely subject to an additional force mediated by the time-varying scalar field.

One could argue that within voids (where screening is irrelevant), this distinction between how the force acting on void matter is enhanced is meaningless, as one could provide a scalar field that has the same effect on void matter as the modification to gravity. Modified gravity models may be seen as equivalent to quintessence models, in that one set of models modifies the left-hand side of Einstein's field equations while the other set of models modifies the right-hand side of Einstein's field equations, but because it does not matter where we write the additional terms, the solution to these equations is the same. Both result in the same alternative physics.

This interchangeability is evident even in the ΛCDM version of Einstein's field equations. Equation 1.1 can be written with the term $\Lambda g_{\mu\nu}$ on the right-hand side, as a constant scalar field giving rise to the acceleration of expansion – an extra form of energy, more compatible with its usual interpretation as dark energy. Writing Λ on the left-hand side can be interpreted as a modification to gravity (of a Universe with steadily decreasing expansion) because it alters the gravitational equations even in the absence of energy sources (when $T_{\mu\nu} = 0$). Similarly, adding a time-dependent scalar field to the stress-energy tensor is equivalent to modifying the equations of gravity on the left-hand side of Einstein's

field equations, and results in the same physics. In fact, even modified gravity models featuring derivatives of the metric $g_{\mu\nu}$ can be rewritten as dynamical dark energy models with multiple scalar fields (Wetterich, 2015). This is ultimately because of field relativity. Observables are dependent on the dynamical degrees of freedom rather than the choice of fields to represent them. Modified gravity models that are consistent with the evolution of the Universe are usually equivalent to some dynamical dark energy model, particularly coupled models, and it is possible to map classes of modified gravity models to dynamical dark energy models through non-linear field transformations[1].

The specific modified gravity models mentioned above are not exactly equivalent to the specific quintessence models studied in this thesis, and yet they produce the same alternative physics as our quintessence models (at least within voids). This is significant because it indicates the existence of multiple other quintessence models (for example, with differing potentials or multiple scalar fields) that would exhibit the same signature, perhaps to varying degrees. The density of voids is therefore a powerful differentiator between the standard model and a wide range of different alternative models. Distinguishing between modified gravity models and dynamical dark energy models is not as straightforward with voids, which can be understood in terms of the equivalence between modified gravity models and quintessence models. However, given that the models discussed are not exactly equivalent models, differences between them may exist elsewhere in these cosmologies, perhaps in higher density structures where the fifth force is screened but the dynamical scalar field is not.

5.9 Observational Probes

The existence of emptier voids occurring in non-standard cosmologies beyond the pure quintessence and coupled dark energy model we investigated has significant implications. The commonality of emptier voids in both quintessence and modified gravity models, as well as the existence of emptier voids in different CDE models than our own (with similarly behaving scalar field potentials), suggests that void emptiness may be used to distinguish between the standard model and multiple quintessence models (including multiple coupled dark energy models) and between the standard model and various equivalent modified gravity models. The void density signature can thus be used to distinguish between the standard model and multiple alternative cosmological models, making it a very powerful probe of a wide range of cosmological models. The challenge before us is to turn this signature into robust observational probes of the Universe.

The two primary problems we face are that galaxy distribution data provide only a very sparse representation of the actual galaxy distribution that gets worse with increasing

[1] Although differences in growth factors have been found between modified gravity models and quintessence models, this only applies to pure quintessence without coupling. Coupling alters the growth factor compared to pure quintessence, so the issue of differentiating between modified gravity models and pure quintessence models reduces to the problem of differentiating between coupled and pure quintessence models.

redshift, and that the galaxy distribution itself is an inherently biased way of representing the true matter distribution, even if it is well sampled. Without a well estimated density field, the signature in the average void density distribution is not likely to be visible. It is unlikely that even the upcoming next generation telescopes (e.g. the Large Synoptic Survey Telescope (LSST) and Euclid) will be capable of measuring the density field with sufficient accuracy for a direct comparison of the true average void density distribution to our theoretical predictions to yield meaningful results.

One way of overcoming this hurdle is to use weak gravitational lensing data from LSST and Euclid surveys to map the underlying dark matter distribution. However, this method requires us to make assumptions about the galaxy biasing, which is not precisely understood. As such, we must find other, less direct approaches of observing our signature. In this section, we suggest a number of possible methods to distinguish between a scalar field model and the standard model, that stems directly from the differences in average void density.

5.9.1 Void Density Profiles

Although we did not directly measure density profiles, it is likely that if we had we would have found greatest deviation around the inner regions of voids, consistent with other studies. As such, we expect our void density signal to be visible in averaged stacked void density profiles as well as in the void density distribution.

One way to measure void density profiles is through weak gravitational lensing, as the lensing signal generated by voids is related to their underlying matter distribution. The density or mass profiles may be deduced from the galaxy distribution in and around the voids, and then the stacked profile (to reduce the effect of noise) can be fit to the predicted profiles for each cosmological model. Next-generation surveys such as the LSST and Euclid are expected to have the capabilities to enable such measurements.

Previous studies (e.g. Falck et al., 2018) have shown that an averaged stacked void density profile can be an effective and alternative method of differentiating between cosmological models using void densities. In particular, the differences in void density profile remain even when using halos to trace the density field, instead of the full dark matter distribution, so the use of density profiles could be effective in probing cosmology from observational data. However, since haloes are traced by galaxies, the halo distribution will likely contain some bias that may hide the signal we are looking for.

5.9.2 Velocity Field

Measuring the velocity field in and around voids may offer another related method of probing for signs of alternative cosmology. Linear theory dictates a link between density profiles and velocity profiles within voids, where the velocity of particles at a particular radius is proportional to the density contrast at that radius (Peebles, 1993). If density profiles show discrepancies, void velocity profiles should as well. The tangential velocity

profiles within voids may magnify the discrepancy better than radial velocity profiles, simply because tangential velocities tend to be a lot larger than the radial component (Falck et al., 2018). However, it is much easier to measure radial velocities than tangential velocities of galaxies around line-of-sight voids, so the discrepancy in the radial component may offer the best chance of detecting the signal, although many more galaxies would need to be sampled in order to detect the small signal.

5.9.3 Differences in Sheet, Filament and Knot Densities and Velocities

If voids have less matter in them in scalar field cosmologies, then this absent matter should be found elsewhere outside of the voids. It is possible that the missing matter gathers in just the boundary of the voids, in the sheets, rather than higher density structures. If this is the case, then sheets should have a significantly higher density in scalar field cosmologies than in the standard model cosmology. It is also a possibility that it is not merely the void evacuation rate that is increased, but the general accumulation rate onto higher density structures. If this is the case, then we should find that the knots are significantly denser in scalar field cosmologies. The sheets and filaments may also show differences, depending on the balance between the rates of evacuation and accumulation of matter for these structures.

As the density of large-scale substructures is correlated with the velocity of matter within and surrounding it, in the scenarios outlined above, we should expect an increased flow of matter on to higher density structures, either sheets or knots. Differences in velocity streams may be more accurately measured than differences in average void density because the average velocity field can still be well estimated with a subset of the true matter distribution, unlike the density field (provided that observational biases are appropriately accounted for, such as the possibility that the subset is not random).

CHAPTER 6

Conclusions and Future Work

The goal of this thesis was to find the observational signatures of alternative cosmological models on the large-scale matter distribution, in order to provide a means of distinguishing between alternative models and the standard model of cosmology with future generations of telescopic surveys. My work is strongly motivated by the lack of scientific understanding of the dark sector in our Universe. By providing a way to rule out or constrain possible alternative cosmological models through observations, I provide a path toward understanding the nature of the dark sector, in particular dark energy, in our Universe.

I focused on identifying the unique signatures of two models from the quintessence (or dynamical dark energy) class of models: an uncoupled quintessence model (ϕCDM) and a coupled dark energy model (CDE). Both these models contain a dynamical scalar field, ϕ, characterised by the Ratra–Peebles potential, in place of a cosmological constant. Unlike ΛCDM, the dark energy density in these models is constantly evolving. The coupled model additionally includes interaction between the scalar field and the dark matter field, in which dark matter decays into dark energy, giving rise to an effective gravitational drag only experienced by dark matter.

In this thesis, I searched for imprints of these cosmological models on the properties and evolution of cosmic voids. I performed a comprehensive study into the properties of cosmic voids and their evolution, conducting the first ever model-comparison study of voids in the high and low redshift universe, spanning a redshift range of $z = 12 - 0$. I used adiabatic hydrodynamical simulations of each of the two alternative models and ΛCDM to study the large-scale matter distribution. Each simulation was 500 h^{-1} Mpc in length, cubic, and contained 2×512^3 dark matter particles and baryonic (gas) particles. The simulations were all normalised so that they had the same σ_8 (mass variance), $\Omega_{\rm m}$, $\Omega_{\rm b}$ and h at $z = 0$, and each simulation began with the same density perturbation *phases* (not amplitudes) to ensure that any differences manifesting in their respective large-scale structures could be attributed to differences in the governing cosmology rather than cosmic variance.

I developed a void-finding pipeline based on the Hessian of the density field to find voids within the dark matter distribution of the simulations. The void finder classifies

regions of the density field into one of four categories – void-like, sheet-like, filament-like and knot-like – based on the sign of the Hessian matrix eigenvalues, and is extremely versatile. It can also be used to find sheets, filaments and knots, and can be applied to any distribution of matter, including observational data.

I investigated a number of key void population properties, and compared them between cosmological models with the goal of finding discrepancies that can be used to observationally distinguish between the models. The properties I studied were the population size and its evolution with redshift, the distribution and evolution of void volumes, void ellipticities and void prolateness, and the distribution and evolution of the average density of voids. Whilst other studies have looked into similar properties in other alternative cosmological models (e.g. Sutter et al., 2015; Pollina et al., 2016; Falck et al., 2018), none have yet performed a wide-ranging study of void properties and their evolution across the redshift range $z = 12 - 0$. The study presented in this thesis is the first wide-ranging redshift study of voids within any alternative cosmological model, where I provide insight into the evolution of voids within these models, as well as reveal the extent that alternative dark sector physics has on the evolution and properties of voids.

My most important result is that the voids in the quintessence models are, on average, less dense than the voids in the standard model. I found that in the range $z = 12 - 0$, the average density distribution in the ϕCDM model peaks at a lower density than that of the CDE or ΛCDM, and the ΛCDM model peaks at the highest density. These discrepancies are statistically significant at all redshifts studied, meaning that the density of voids could be the key to distinguishing between the three models. The imprint on void density left by the scalar field is likely the result of an increased evacuation rate, including perhaps an earlier start to evacuation. The imprint exists in both ϕCDM and CDE, though the coupling within the dark sector mitigates the effect and reduces the imprint, due to the associated gravitational drag experienced by dark matter (which in turn affects the motion of baryonic matter).

The enhanced evacuation rate from voids also increases the likelihood of void mergers, as walls of matter between voids are more quickly evacuated than otherwise. Thus, both quintessence models should have more void mergers than the standard model at most redshifts. Indeed, my population size results suggests that this is the case, with both models showing a greater void abundance than ΛCDM at early times, followed by a lower void abundance at late times. The ϕCDM model contains fewer voids than the CDE model at every late redshift except for $z = 0$, consistent with the model having a greater void evacuation rate.

I also found that small, though not statistically significant, differences exist between the volume distributions predicted by each model, that are also consistent with our finding that voids in quintessence models exhibit higher void evacuation rates than voids in ΛCDM. In particular, I found that both the quintessence models generally contain a greater abundance of large voids (voids with $V > 1000\ h^{-3}$ Mpc^3) than the standard model, due to a higher void merger rate, while the ΛCDM model contains the greatest number of mid-sized voids ($100 \lesssim V \lesssim 1000\ h^{-3}$ Mpc^3). The difference in large voids is noticeable except

at later redshifts when the CDE volume distribution becomes very similar to the ΛCDM distribution (except at $z = 0$), and at $z = 0$ when ϕCDM produces slightly fewer large voids than ΛCDM does. Although the trends for large voids are not certain due to small number statistics, and as such they ought to be treated with caution, they are likely to be more significant than our statistical analyses suggest, since each simulation was initialised with the same density perturbation phases, thus minimising the effect of cosmic variance. It appears that for many of the redshifts, the enhanced void merger rates, arising from greater particle evacuation rates, are producing greater numbers of large voids in the quintessence models.

My results show that at $z = 0$, an interesting phenomenon occurs. Although at all other redshifts, the difference between the average void densities in ϕCDM and CDE are distinct, at $z = 0$ they are not completely distinct from each other. The CDE model appears to undergo a sudden relative increase in its overall evacuation rate compared to ϕCDM, pushing it towards consistency with the uncoupled quintessence prediction. This is likely the result of the decaying dark matter field into the scalar field, steadily increasing its density and influence so that the net evacuation rate surpasses that of ϕCDM. Furthermore, at very late times, the CDE model moves from having more voids than ϕCDM to having fewer voids, and it suddenly exhibits a greater large void abundance than the other two models (a statistically significant discrepancy), suggesting a suddenly increased merger rate consistent with a suddenly enhanced evacuation rate.

Despite these subtle discrepancies, the overall void volume distributions are very similar between the models, indicating that neither the presence of the scalar field nor the coupling within the dark sector leave a significant imprint on void volumes at most redshifts.

I also found that void shapes, in particular ellipticity and prolateness, are extremely similar for all models, and no statistically significant differences between the ellipticity and prolateness distributions of each model exist, across all redshifts studied. The shape distributions for voids of different sizes are also indistinguishable between the models. These results suggest that to first order, the shape of voids do not carry imprints of dynamical dark energy or dark sector coupling, and like void volumes they are most likely determined by gravitational interactions and the specific initial density perturbations, whose influence dominates any imprint left by a scalar field.

My results demonstrate that in all three models, voids are rarely spheroidal. Instead they are slightly elliptical and prolate, consistent with the anisotropic and asymmetric nature of void growth. Additionally, many of the voids I identified with my Hessian-based void-finder are very irregular in shape, especially if large. These are important considerations wherever the spherical void assumption is made, such as in void stacking analyses and in the calculation of radial profiles.

Overall, my results show that the growth of voids, their volumes and their shapes are largely governed by gravitational effects rather than underlying cosmology. Although hints of differences exist in these properties between models, they are generally not statistically significant, and show only a small dependence on cosmology and dark sector physics. As

such, void volumes and shapes are not likely to make effective observational probes of cosmology.

My most promising result is that the density of voids is heavily influenced by whether dark energy arises from a dynamical scalar field governed by the Ratra–Peebles potential or a cosmological constant, and whether there is interaction between the scalar field and the dark matter field. If other simple scalar field models with different potentials display the same feature (which may indeed be the case if they produce a similar expansion history), then this is a signature that has high potential to differentiate between an entire class of simple dynamical scalar field models and the standard model in our Universe, as well as between uncoupled quintessence and coupled dark energy models, across a wide range of redshifts.

My results add to those from other studies into the differences between a CDE model and the standard model (e.g. Sutter et al., 2015; Pollina et al., 2016). These studies show only small discrepancies between CDE and the standard model in void densities, which were not statistically significant. My results are the first to show such a significant discrepancy in void densities between a CDE cosmology and the standard cosmology, most likely due to the smaller degree of coupling within our model compared to the models used in prior studies. Presumably, the increased drag force present in models with a higher degree of coupling reduces the effect of the scalar field on void evacuation rate to the point where only a small deviation from the standard model remains.

Intriguingly, studies into modified gravity models exhibit a very similar signature to the one I discovered in the quintessence models (e.g. Cai, Padilla & Li, 2015; Barreira et al., 2015; Falck et al., 2018). This is because some modified gravity models are equivalent to dynamical dark energy models, and so they have would the same effect on the density of voids as a dynamical scalar field does. Apart from the interesting question of how to interpret these models, the fact that voids are emptier in certain modified gravity models (those that feature enhanced gravitational interactions), as well as in dynamical dark energy models, indicate how promising my signature is. It could be an extremely effective differentiator between the standard model and a wide range of alternative models that are similar in nature. This provides additional motivation to determine how best to make use of the signature to probe the nature of dark energy in our Universe.

The most fruitful path following on from this work is to develop methods of magnifying the signal contained in the emptiness of voids. Stacking voids is a popular method of reducing noise in void properties, and it has been shown that a stacked void density profile may very well be observable even when the density field is not well characterised (for example, if it was traced with halos). However, fully determining the likelihood of finding this signature in real observational data (if it exists), requires us to run mock observations, calculate the density field from such observations, employ the void-finding pipeline on the density field, and calculate the average void density distributions or the stacked void density profiles. Additionally, we must look for other observables that the evacuation rate of voids would leave imprints on, so that they can be used as independent signatures of the scalar field, to support the void density results. One such observable could be the void

velocity profiles, which may be less prone to observational biases and noise effects than quantities derived from the density field. Another possibility would be the densities and the velocity fields of other structures such as sheets and knots, which could exhibit higher densities and in-falling velocities in quintessence models than the standard model.

Another interesting avenue to explore would be the void merger rates and void evacuation rates in each of the simulations, along with their evolution in time. I have found evidence for an enhanced void merger rate in the two quintessence models compared to ΛCDM, in the volume distributions and in the evolution of the void population size, but these differences have not yet been quantified. Tracking the motion of particles out of voids to quantify the rate of void evacuation and how it evolves with time in each model would also serve to confirm the effect the scalar field has on voids. The study could be extended to determine the rate of particle accumulation on to higher density structures as well, to determine if the increased particle velocities also exist in these structures.

My work could also be extended by conducting the same study with a different choice of normalisation redshift for σ_8 and other cosmological parameters, to determine if the choice of $z = 0$ as normalisation redshift significantly impacts our results. Running the simulations in a larger box would also be useful for removing the issue of small number statistics when analysing the population of large voids, allowing better analysis and quantification of the effect of the scalar field and dark sector interactions on the large void population. A box of length $1000 - 2000\ h^{-1}$ Mpc would provide hundreds to thousands of very large voids for study.

A more theoretical question that arises from the work in this thesis is how the scalar field influences void evacuation rate. What type of dynamical scalar field, and what type of potential, gives rise to emptier voids? What aspect of these models cause voids to evacuate more quickly? It is also important to confirm that there are indeed various different scalar field models that produce the same signature, perhaps to varying degrees.

Ultimately, the goal of this work was to find significant differences between the Standard Model of Cosmology and alternative cosmological models. I have successfully found real differences in the average density of voids in the uncoupled quintessence and coupled dark energy models compared to ΛCDM, which I propose are the result of an enhanced particle evacuation rate from voids driven by the scalar field in these models. I have also found that the coupling between the scalar field and dark matter field leaves an imprint on void densities. These are significant results because they provide a means of distinguishing between the standard model and quintessence models, and between uncoupled quintessence and coupled dark energy models. The signature may be versatile enough to differentiate between the standard model and numerous other alternative models. If my results are properly utilised, in the near future it will be possible to observationally probe the dark sector of our Universe, and to finally illuminate its true nature.

Bibliography

Abbott B. P. et al., 2016, Physical Review Letters, 116, 061102

Abbott B. P. et al., 2017a, ApJ, 848, L13

Abbott B. P. et al., 2017b, Physical Review Letters, 119, 161101

Abel T., Hahn O., Kaehler R., 2012, MNRAS, 427, 61

Ackermann M. et al., 2015, ApJ, 807, 169

Adermann E., Elahi P. J., Lewis G. F., Power C., 2017, MNRAS, 468, 3381

Adermann E., Elahi P. J., Lewis G. F., Power C., 2018, MNRAS, 479, 4861

Ahmed S. H., Brooks A. M., Christensen C. R., 2017, MNRAS, 466, 3119

Alcock C. et al., 2000, ApJ, 542, 281

Amendola L., 2000, Phys. Rev. D, 62, 043511

Amendola L., Baldi M., Wetterich C., 2008, Phys. Rev. D, 78, 023015

Anderhalden D., Diemand J., Bertone G., Macciò A. V., Schneider A., 2012, JCAP, 10, 047

Anderhalden D., Schneider A., Macciò A. V., Diemand J., Bertone G., 2013, JCAP, 3, 014

Aragón-Calvo M. A., Jones B. J. T., van de Weygaert R., van der Hulst J. M., 2007, A&A, 474, 315

Baker T., Bellini E., Ferreira P. G., Lagos M., Noller J., Sawicki I., 2017, ArXiv e-prints

Baldi M., 2012, MNRAS, 422, 1028

Baldi M., Pettorino V., Robbers G., Springel V., 2010, MNRAS, 403, 1684

Barausse E., Sotiriou T. P., Miller J. C., 2008, Classical and Quantum Gravity, 25, 062001

Barnes L. A. et al., 2018, MNRAS, 477, 3727

Barreira A., Cautun M., Li B., Baugh C. M., Pascoli S., 2015, JCAP, 8, 028

Bartels R., Krishnamurthy S., Weniger C., 2016, Physical Review Letters, 116, 051102

Bekenstein J. D., 2004, Phys. Rev. D, 70, 083509

Bennett C. L. et al., 2013, ApJS, 208, 20

Benson A. J., Frenk C. S., Lacey C. G., Baugh C. M., Cole S., 2002, MNRAS, 333, 177

Birrell N. D., Davies P. C. W., 1984, Quantum Fields in Curved Space, Cambridge Monographs on Mathematical Physics. Cambridge Univ. Press, Cambridge, UK

Biswas A., Mani K. R. S., 2008, Central European Journal of Physics, 6, 754

Blake C. et al., 2011, MNRAS, 415, 2892

Bolte M., Hogan C. J., 1995, Nature, 376, 399

Bond N. A., Strauss M. A., Cen R., 2010, MNRAS, 409, 156

Boran S., Desai S., Kahya E. O., Woodard R. P., 2018, Phys. Rev. D, 97, 041501

Boylan-Kolchin M., Bullock J. S., Kaplinghat M., 2011, MNRAS, 415, L40

Boylan-Kolchin M., Bullock J. S., Kaplinghat M., 2012, MNRAS, 422, 1203

Brans C., Dicke R. H., 1961, Physical Review, 124, 925

Brooks A. M., Kuhlen M., Zolotov A., Hooper D., 2013, ApJ, 765, 22

Brooks A. M., Papastergis E., Christensen C. R., Governato F., Stilp A., Quinn T. R., Wadsley J., 2017, ApJ, 850, 97

Brooks A. M., Zolotov A., 2014, ApJ, 786, 87

Buchbinder I. L., Odintsov S. D., Shapiro I. L., 1992, Effective action in quantum gravity.

Buchdahl H. A., 1970, MNRAS, 150, 1

Bullock J. S., Kravtsov A. V., Weinberg D. H., 2000, ApJ, 539, 517

Cai Y.-C., Padilla N., Li B., 2015, MNRAS, 451, 1036

Carlesi E., Knebe A., Lewis G. F., Wales S., Yepes G., 2014a, MNRAS, 439, 2943

Carlesi E., Knebe A., Lewis G. F., Yepes G., 2014b, MNRAS, 439, 2958

Carlesi E. et al., 2016, MNRAS, 458, 900

Carroll S. M., 2001, Living Reviews in Relativity, 4, 1

Cautun M., van de Weygaert R., Jones B. J. T., 2013, MNRAS, 429, 1286

Cautun M., van de Weygaert R., Jones B. J. T., Frenk C. S., 2014, MNRAS, 441, 2923

Chaboyer B., Demarque P., Kernan P. J., Krauss L. M., 1996, Science, 271, 957

Chesler P. M., Loeb A., 2017, Physical Review Letters, 119, 031102

Chiba T., 2003, Physics Letters B, 575, 1

Clowe D., Bradač M., Gonzalez A. H., Markevitch M., Randall S. W., Jones C., Zaritsky D., 2006, ApJ, 648, L109

Coc A., Vangioni-Flam E., Descouvemont P., Adahchour A., Angulo C., 2004, ApJ, 600, 544

Colberg J. M. et al., 2008, MNRAS, 387, 933

Colberg J. M., Sheth R. K., Diaferio A., Gao L., Yoshida N., 2005, MNRAS, 360, 216

Colless M., 2004, Measuring and Modeling the Universe, 196

Conn A. R. et al., 2013, ApJ, 766, 120

Copi C. J., Schramm D. N., Turner M. S., 1995, Science, 267, 192

Creminelli P., Vernizzi F., 2017, ArXiv e-prints

Damour T., Vilenkin A., 1996, Phys. Rev. D, 53, 2981

Dar A., 1995, ApJ, 449, 550

Davis M., Efstathiou G., Frenk C. S., White S. D. M., 1985, ApJ, 292, 371

Dawson K. S. et al., 2013, AJ, 145, 10

Daylan T., Finkbeiner D. P., Hooper D., Linden T., Portillo S. K. N., Rodd N. L., Slatyer T. R., 2016, Physics of the Dark Universe, 12, 1

de Bernardis P. et al., 2000, Nature, 404, 955

de Blok W. J. G., 2010, Advances in Astronomy, 2010, 789293

de Rham C., Gabadadze G., Tolley A. J., 2011, Physical Review Letters, 106, 231101

de Vega H. J., Salucci P., Sanchez N. G., 2012, NewA, 17, 653

Di Valentino E., Bœhm C., Hivon E., Bouchet F. R., 2018, Phys. Rev. D, 97, 043513

Dolgov A. D., Kawasaki M., 2003, Physics Letters B, 573, 1

Doran M., 2005, JCAP, 10, 011

Doran M., Robbers G., 2006, JCAP, 6, 026

Doran M., Schwindt J.-M., Wetterich C., 2001, Phys. Rev. D, 64, 123520

Dubinski J., Carlberg R. G., 1991, ApJ, 378, 496

Dvali G., Gabadadze G., Porrati M., 2000, Physics Letters B, 485, 208

Dyson F. W., Eddington A. S., Davidson C., 1920, Philosophical Transactions of the Royal Society of London Series A, 220, 291

Efstathiou G. et al., 2002, MNRAS, 330, L29

Efstathiou G., Sutherland W. J., Maddox S. J., 1990, Nature, 348, 705

Einstein A., 1916a, Annalen der Physik, 354, 769

Einstein A., 1916b, Sitzungsberichte der Königlich Preußischen Akademie der Wissenschaften (Berlin), Seite 688-696.

Einstein A., 1917, Sitzungsber. Preuss. Akad. Wiss. Berlin (Math. Phys.), 1917, 142

Einstein A., 1918, Sitzungsberichte der Königlich Preußischen Akademie der Wissenschaften (Berlin), Seite 154-167.

Einstein A., de Sitter W., 1932, Proceedings of the National Academy of Sciences, 18, 213

Eisenstein D. J. et al., 2011, AJ, 142, 72

Elahi P. J., 2013, STF: Structure Finder. Astrophysics Source Code Library

Elahi P. J., Lewis G. F., Power C., Carlesi E., Knebe A., 2015, MNRAS, 452, 1341

Elahi P. J., Mahdi H. S., Power C., Lewis G. F., 2014, MNRAS, 444, 2333

Elahi P. J., Thacker R. J., Widrow L. M., 2011, MNRAS, 418, 320

Elbert O. D., Bullock J. S., Garrison-Kimmel S., Rocha M., Oñorbe J., Peter A. H. G., 2015, MNRAS, 453, 29

Ezquiaga J. M., Zumalacárregui M., 2017, Phys. Rev. Lett., 119, 251304

Fabbiano G., 1993, Advances in Space Research, 13

Faber S. M., Jackson R. E., 1976, ApJ, 204, 668

Fabian A. C., Thomas P. A., White, III R. E., Fall S. M., 1986, MNRAS, 221, 1049

Fabricant D., Gorenstein P., 1983, ApJ, 267, 535

Fabricant D., Lecar M., Gorenstein P., 1980, Highlights of Astronomy, 5, 689

Falck B., Koyama K., Zhao G.-B., Cautun M., 2018, MNRAS, 475, 3262

Falck B., Neyrinck M. C., 2015, MNRAS, 450, 3239

Falck B. L., Neyrinck M. C., Szalay A. S., 2012, ApJ, 754, 126

Forero-Romero J. E., Hoffman Y., Gottlöber S., Klypin A., Yepes G., 2009, MNRAS, 396, 1815

Freeman K. C., 1970, ApJ, 160, 811

Frieman J. A., Turner M. S., Huterer D., 2008, ARA&A, 46, 385

Frolov A. V., 2008, Physical Review Letters, 101, 061103

Fukugita M., Hogan C. J., Peebles P. J. E., 1998, ApJ, 503, 518

Giannantonio T. et al., 2006, Phys. Rev. D, 74, 063520

Graff D. S., Freese K., 1996, ApJ, 456, L49

Greenstein J. L., Oke J. B., Shipman H. L., 1971, ApJ, 169, 563

Guth A. H., 1981, Phys. Rev. D, 23, 347

Hahn O., Carollo C. M., Porciani C., Dekel A., 2007, MNRAS, 381, 41

Hanany S. et al., 2000, ApJ, 545, L5

He J.-H., Wang B., Zhang P., 2009, Phys. Rev. D, 80, 063530

Heymans C. et al., 2012, MNRAS, 427, 146

Hinshaw G. et al., 2013, ApJS, 208, 19

Hinshaw G. et al., 2009, ApJS, 180, 225

Hochberg Y., Kuflik E., Volansky T., Wacker J. G., 2014, Phys. Rev. Lett., 113, 171301

Hoekstra H., 2007, MNRAS, 379, 317

Hoffman Y., Metuki O., Yepes G., Gottlöber S., Forero-Romero J. E., Libeskind N. I., Knebe A., 2012, MNRAS, 425, 2049

Hoyle F., Vogeley M. S., 2002, ApJ, 566, 641

Hubble E., 1929, Proceedings of the National Academy of Science, 15, 168

Hut P., White S. D. M., 1984, Nature, 310, 637

Ibata N. G., Ibata R. A., Famaey B., Lewis G. F., 2014a, Nature, 511, 563

Ibata R. A., Ibata N. G., Lewis G. F., Martin N. F., Conn A., Elahi P., Arias V., Fernando N., 2014b, ApJ, 784, L6

Ibata R. A. et al., 2013, Nature, 493, 62

Jain B., Khoury J., 2010, Annals of Physics, 325, 1479

Jordan P., 1955, Vieweg (Braunschweig)

Kamada A., Inoue K. T., Takahashi T., 2016, Phys. Rev. D, 94, 023522

Kamada A., Kaplinghat M., Pace A. B., Yu H.-B., 2017, Physical Review Letters, 119, 111102

Kaplinghat M., Tulin S., Yu H.-B., 2016, Physical Review Letters, 116, 041302

Kauffmann G., Melott A. L., 1992, ApJ, 393, 415

Khoury J., Weltman A., 2004, Phys. Rev. D, 69, 044026

Klypin A., Kravtsov A. V., Valenzuela O., Prada F., 1999, ApJ, 522, 82

Le Verrier U. J., 1859, Annales de l'Observatoire de Paris, 5

Lee S., Liu G.-C., Ng K.-W., 2006, Phys. Rev. D, 73, 083516

Lee S. K., Lisanti M., Safdi B. R., Slatyer T. R., Xue W., 2016, Physical Review Letters, 116, 051103

Li Z., Wang Y., Yang X., Chen X., Xie L., Wang X., 2013, ApJ, 768, 20

Libeskind N. I., Di Cintio A., Knebe A., Yepes G., Gottlöber S., Steinmetz M., Hoffman Y., Martinez-Vaquero L. A., 2013a, PASA, 30, e039

Libeskind N. I., Hoffman Y., Forero-Romero J., Gottlöber S., Knebe A., Steinmetz M., Klypin A., 2013b, MNRAS, 428, 2489

Libeskind N. I. et al., 2018, MNRAS, 473, 1195

Limousin M. et al., 2007, ApJ, 668, 643

Linde A. D., 1984, Reports on Progress in Physics, 47, 925

Loeb A., Weiner N., 2011, Physical Review Letters, 106, 171302

Lovell M. R. et al., 2012, MNRAS, 420, 2318

Lovell M. R., Frenk C. S., Eke V. R., Jenkins A., Gao L., Theuns T., 2014, MNRAS, 439, 300

Lovell M. R., Gonzalez-Perez V., Bose S., Boyarsky A., Cole S., Frenk C. S., Ruchayskiy O., 2017, MNRAS, 468, 2836

Macias O., Gordon C., Crocker R. M., Coleman B., Paterson D., Horiuchi S., Pohl M., 2016, ArXiv e-prints

Marsh D. J. E., Silk J., 2014, MNRAS, 437, 2652

Milgrom M., 1983, ApJ, 270, 365

Milne E. A., 1933, ZAp, 6, 1

Moore B., Ghigna S., Governato F., Lake G., Quinn T., Stadel J., Tozzi P., 1999, ApJ, 524, L19

Mota D. F., Pettorino V., Robbers G., Wetterich C., 2008, Physics Letters B, 663, 160

Müller V., Arbabi-Bidgoli S., Einasto J., Tucker D., 2000, MNRAS, 318, 280

Murgia R., Gariazzo S., Fornengo N., 2016, JCAP, 4, 014

Navarro J. F., Frenk C. S., White S. D. M., 1996, ApJ, 462, 563

Navarro J. F., Frenk C. S., White S. D. M., 1997, ApJ, 490, 493

Neyrinck M. C., 2008, MNRAS, 386, 2101

Nickerson S., Stinson G., Couchman H. M. P., Baili J., Wadsley J., 2012, in Astronomical Society of the Pacific Conference Series, Vol. 453, Advances in Computational Astrophysics: Methods, Tools, and Outcome, Capuzzo-Dolcetta R., Limongi M., Tornambè A., eds., p. 305

Nickerson S., Stinson G., Couchman H. M. P., Bailin J., Wadsley J., 2011, MNRAS, 415, 257

Nicolis A., Rattazzi R., Trincherini E., 2009, Phys. Rev. D, 79, 064036

Ntelis P. et al., 2017, JCAP, 6, 019

Ostriker J. P., Peebles P. J. E., 1973, ApJ, 186, 467

Ostriker J. P., Peebles P. J. E., Yahil A., 1974, ApJ, 193, L1

Pahwa I. et al., 2016, MNRAS, 457, 695

Pawlowski M. S., 2018, Modern Physics Letters A, 33, 1830004

Pawlowski M. S. et al., 2014, MNRAS, 442, 2362

Pawlowski M. S., Kroupa P., 2014, ApJ, 790, 74

Pawlowski M. S., Pflamm-Altenburg J., Kroupa P., 2012, MNRAS, 423, 1109

Peccei R. D., Quinn H. R., 1977a, Phys. Rev. D, 16, 1791

Peccei R. D., Quinn H. R., 1977b, Phys. Rev. Lett., 38, 1440

Peebles P. J., Ratra B., 2003, Reviews of Modern Physics, 75, 559

Peebles P. J. E., 1993, Principles of Physical Cosmology

Percival W. J. et al., 2002, MNRAS, 337, 1068

Perlmutter S. et al., 1999, ApJ, 517, 565

Perlmutter S., Schmidt B. P., 2003, in Lecture Notes in Physics, Berlin Springer Verlag, Vol. 598, Supernovae and Gamma-Ray Bursters, Weiler K., ed., pp. 195–217

Peter A. H. G., Rocha M., Bullock J. S., Kaplinghat M., 2013, MNRAS, 430, 105

Pettorino V., 2013, Phys. Rev. D, 88, 063519

Pettorino V., Amendola L., Baccigalupi C., Quercellini C., 2012, Phys. Rev. D, 86, 103507

Phillips J., Weinberg D. H., Croft R. A. C., Hernquist L., Katz N., Pettini M., 2001, ApJ, 560, 15

Phillips M. M., 1993, ApJ, 413, L105

Planck Collaboration et al., 2014a, A&A, 571, A16

Planck Collaboration et al., 2014b, A&A, 571, A20

Planck Collaboration et al., 2016a, A&A, 594, A13

Planck Collaboration et al., 2016b, A&A, 594, A24

Planck Collaboration et al., 2016c, A&A, 594, A14

Planck Collaboration et al., 2016d, A&A, 594, A22

Platen E., van de Weygaert R., Jones B. J. T., 2007, MNRAS, 380, 551

Pollina G., Baldi M., Marulli F., Moscardini L., 2016, MNRAS, 455, 3075

Pontzen A., Governato F., 2012, MNRAS, 421, 3464

Pourtsidou A., Skordis C., Copeland E. J., 2013, Phys. Rev. D, 88, 083505

Power C., 2013, PASA, 30, e053

Randall S. W., Markevitch M., Clowe D., Gonzalez A. H., Bradač M., 2008, ApJ, 679, 1173

Ratra B., Peebles P. J. E., 1988, Phys. Rev. D, 37, 3406

Reyes R., Mandelbaum R., Seljak U., Baldauf T., Gunn J. E., Lombriser L., Smith R. E., 2010, Nature, 464, 256

Riess A. G., 2000, PASP, 112, 1284

Riess A. G. et al., 1998, AJ, 116, 1009

Riess A. G. et al., 2016, ApJ, 826, 56

Rocha M., Peter A. H. G., Bullock J. S., Kaplinghat M., Garrison-Kimmel S., Oñorbe J., Moustakas L. A., 2013, MNRAS, 430, 81

Rogstad D. H., Shostak G. S., 1972, ApJ, 176, 315

Rubin V. C., Ford, Jr. W. K., 1970, ApJ, 159, 379

Salcido J. et al., 2018, MNRAS, 477, 3744

Sawala T. et al., 2016, MNRAS, 457, 1931

Schneider A., Anderhalden D., Macciò A. V., Diemand J., 2014, MNRAS, 441, L6

Schneider A., Smith R. E., Macciò A. V., Moore B., 2012, MNRAS, 424, 684

Scranton R. et al., 2003, ArXiv Astrophysics e-prints

Seljak U., Slosar A., McDonald P., 2006, JCAP, 10, 014

Shandarin S. F., 2011, JCAP, 5, 015

Smoot G. F. et al., 1992, ApJ, 396, L1

Spergel D. N., Steinhardt P. J., 2000, Physical Review Letters, 84, 3760

Springel V. et al., 2008, MNRAS, 391, 1685

Starobinsky A. A., 1980, Physics Letters B, 91, 99

Steinhardt P. J., 2003, Philosophical Transactions of the Royal Society of London Series A, 361, 2497

Steinhardt P. J., Caldwell R. R., 1998, in Astronomical Society of the Pacific Conference Series, Vol. 151, Cosmic Microwave Background and Large Scale Structure of the Universe, Byun Y. I., Ng K. W., eds., p. 13

Steinhardt P. J., Turner M. S., 1984, Phys. Rev. D, 29, 2162

Steinhardt P. J., Wang L., Zlatev I., 1999, Phys. Rev. D, 59, 123504

Sutter P. M., Carlesi E., Wandelt B. D., Knebe A., 2015, MNRAS, 446, L1

Sutter P. M., Elahi P., Falck B., Onions J., Hamaus N., Knebe A., Srisawat C., Schneider A., 2014, MNRAS, 445, 1235

Sutter P. M., Ricker P. M., 2008, ApJ, 687, 7

Suzuki N. et al., 2012, ApJ, 746, 85

Takahashi R., Tanimoto M., 2006, Physics Letters B, 633, 675

Tisserand P. et al., 2007, A&A, 469, 387

Trowland H. E., 2013, PhD thesis, The University of Sydney

Trowland H. E., Lewis G. F., Bland-Hawthorn J., 2013, ApJ, 762, 72

Tulin S., Yu H.-B., 2018, Phys. Rep., 730, 1

Vainshtein A. I., 1972, Physics Letters B, 39, 393

van de Bruck C., Mifsud J., Morrice J., 2017, Phys. Rev. D, 95, 043513

Viel M., Becker G. D., Bolton J. S., Haehnelt M. G., 2013, Phys. Rev. D, 88, 043502

Vilkovisky G. A., 1992, Class. Quant. Grav., 9, 895

Vogelsberger M., Zavala J., Loeb A., 2012, MNRAS, 423, 3740

Watts A. L., Elahi P. J., Lewis G. F., Power C., 2017, MNRAS, 468, 59

Weinberg S., 1978, Phys. Rev. Lett., 40, 223

Wetterich C., 2015, in Lecture Notes in Physics, Berlin Springer Verlag, Vol. 892, Lecture Notes in Physics, Berlin Springer Verlag, Papantonopoulos E., ed., p. 57

White S. D. M., Davis M., Efstathiou G., Frenk C. S., 1987, Nature, 330, 451

White S. D. M., Frenk C. S., Davis M., 1983, ApJ, 274, L1

White S. D. M., Rees M. J., 1978, MNRAS, 183, 341

Wilczek F., 1978, Phys. Rev. Lett., 40, 279

Williams J. G., Turyshev S. G., Boggs D. H., 2009, International Journal of Modern Physics D, 18, 1129

Williams J. G., Turyshev S. G., Boggs D. H., 2012, Classical and Quantum Gravity, 29, 184004

Winter M., Zaharijas G., Bechtol K., Vandenbroucke J., 2016, ApJ, 832, L6

Xia J.-Q., 2009, Phys. Rev. D, 80, 103514

Xia J.-Q., 2013, JCAP, 11, 022

Yang X., van den Bosch F. C., Mo H. J., Mao S., Kang X., Weinmann S. M., Guo Y., Jing Y. P., 2006, MNRAS, 369, 1293

Zlatev I., Wang L., Steinhardt P. J., 1999, Physical Review Letters, 82, 896

Zwicky F., 1937, ApJ, 86, 217